



National Library  
of Canada

Bibliothèque nationale  
du Canada

Canadian Theses Service    Service des thèses canadiennes

Ottawa, Canada  
K1A 0N4

## NOTICE

The quality of this microform is heavily dependent upon the quality of the original thesis submitted for microfilming. Every effort has been made to ensure the highest quality of reproduction possible.

If pages are missing, contact the university which granted the degree.

Some pages may have indistinct print especially if the original pages were typed with a poor typewriter ribbon or if the university sent us an inferior photocopy.

Reproduction in full or in part of this microform is governed by the Canadian Copyright Act, R.S.C. 1970, c. C-30, and subsequent amendments.

## AVIS

La qualité de cette microforme dépend grandement de la qualité de la thèse soumise au microfilmage. Nous avons tout fait pour assurer une qualité supérieure de reproduction.

S'il manque des pages, veuillez communiquer avec l'université qui a conféré le grade.

La qualité d'impression de certaines pages peut laisser à désirer, surtout si les pages originales ont été dactylographiées à l'aide d'un ruban usé ou si l'université nous a fait parvenir une photocopie de qualité inférieure.

La reproduction, même partielle, de cette microforme est soumise à la Loi canadienne sur le droit d'auteur, SRC 1970, c. C-30, et ses amendements subséquents.

**TOPICS IN THE APPLICATION OF THE ZEEMAN EFFECT**

**by**

**Edgar A. Arriaga**

**Submitted in partial fulfillment of the requirements for  
the degree of Doctor of Philosophy**

**at  
Dalhousie University  
Halifax, Nova Scotia  
June, 1990**

**© Copyright by Edgar A. Arriaga, 1990**



National Library  
of Canada

Bibliothèque nationale  
du Canada

Canadian Theses Service    Service des thèses canadiennes

Ottawa, Canada  
K1A 0N4

The author has granted an irrevocable non-exclusive licence allowing the National Library of Canada to reproduce, loan, distribute or sell copies of his/her thesis by any means and in any form or format, making this thesis available to interested persons.

The author retains ownership of the copyright in his/her thesis. Neither the thesis nor substantial extracts from it may be printed or otherwise reproduced without his/her permission.

L'auteur a accordé une licence irrévocable et non exclusive permettant à la Bibliothèque nationale du Canada de reproduire, prêter, distribuer ou vendre des copies de sa thèse de quelque manière et sous quelque forme que ce soit pour mettre des exemplaires de cette thèse à la disposition des personnes intéressées.

L'auteur conserve la propriété du droit d'auteur qui protège sa thèse. Ni la thèse ni des extraits substantiels de celle-ci ne doivent être imprimés ou autrement reproduits sans son autorisation.

ISBN 0-315-64386-2

Canada

## TABLE OF CONTENTS.

TABLE OF CONTENTS.....	iv
LIST OF FIGURES. ....	vii
LIST OF TABLES.....	x
SUMMARY.....	xi
ACKNOWLEDGEMENTS.....	xii
1. INTRODUCTION.....	1
1.1 ATOMIC ABSORPTION SPECTROSCOPY.....	1
1.1.1 Principle.....	1
1.1.2 Instrumentation.....	5
1.1.3 History.....	9
1.1.4 Absorption and emission profiles.....	11
1.2 THE ZEEMAN EFFECT.....	19
1.2.1 Principle.....	19
1.2.2 The normal Zeeman effect.....	20
1.2.3 The anomalous Zeeman effect.....	21
1.3 BACKGROUND CORRECTION.....	27
1.3.1 Continuous-source background correction.....	29
1.3.2 The Smith-Hieftje method.....	30
1.3.3 Zeeman background correction.....	31
1.3.4 Theory of Zeeman atomic absorption spectrometers.....	34
1.4 SPUTTERING CELLS IN SPECTROSCOPY.....	38
1.5 ELECTRODEPOSITION AS A PRECONCENTRATION TECHNIQUE IN ATOMIC ABSORPTION SPECTROSCOPY.....	40
2. HARMONIC ANALYSIS OF A FIELD-ON-SOURCE CONFIGURATION.....	44
2.1 PURPOSE.....	44
2.2 EXPERIMENTAL.....	49
2.3 RESULTS AND DISCUSSION.....	52
2.3.1 Ne results.....	52

2.3.2	Li and Mg results.....	53
3.	DETECTION OF SPECTRAL INTERFERENCES BY HARMONIC ANALYSIS WITH A FIELD-ON-SOURCE CONFIGURATION.....	62
3.1	PURPOSE.....	62
3.2	EXPERIMENTAL. ....	66
3.2.1	Harmonic measurements. ....	66
3.2.2	Selection of the d.c. field.....	72
3.3	RESULTS AND DISCUSSION. ....	75
3.3.1	Li isotopes.....	75
3.3.2	Platinum-Iron.....	78
4.	ZEEMAN-BACKGROUND CORRECTION IN PULSED DISCHARGE CELLS AT ATMOSPHERIC PRESSURE.....	86
4.1	PURPOSE.....	86
4.2	EXPERIMENTAL. ....	87
4.2.1	Faraday configuration.....	87
4.2.2	Voigt configuration.....	92
4.2.3	Procedure.....	98
4.3	RESULTS AND DISCUSSION. ....	99
4.3.1	Faraday configuration.....	99
4.3.2	Li emission measurements. ....	105
4.3.3	Li dichroic measurements. ....	108
5.	APPLICATION OF ZEEMAN BACKGROUND CORRECTION IN THE DETERMINATION OF Al, Cd, Co, Cr, Cu, Fe, Pb, Mg, Ni, Ag, and Zn ATOMISED IN A CONTINUOUS DISCHARGE CELL AT ATMOSPHERIC PRESSURE.....	116
5.1	PURPOSE.....	116
5.2	EXPERIMENTAL. ....	117
5.2.1	Direct atomisation of Al, Cd, Co, Cr, Cu, Fe, Pb, Mg, Ni, Ag, and Zn .....	117
5.2.2	Deposition of silver and lead.....	119
5.3	RESULTS AND DISCUSSION. ....	123
5.3.1	Direct atomisation of Al, Cd, Co, Cr, Cu, Fe, Pb, Mg, Ni, Ag, and Zn .....	123

5.3.2	Deposition of silver.....	134
5.3.3	Electrodeposition of lead.....	141
6.	GENERAL CONCLUSIONS.....	147
6.1	Harmonic analysis using the Faraday configuration.....	147
6.2	Harmonic analysis using the Voigt configuration.....	147
6.3	Zeeman background correction applied to discharge cells filled with helium at atmospheric pressure.....	148
	APPENDIX A. Jones calculus.....	150
A.1	Theory.....	150
A.2	Matrix representation of common optical components.....	153
A.3	Prediction of the performance of the optical systems by means of Jones calculus.....	158
A.3.1	System No 1: d.c. Zeeman scanning.....	158
A.3.2	System No. 2: field-on-atomiser, Voigt configuration.....	159
A.3.3	System No. 3: absorption cell, Faraday configuration.....	162
	APPENDIX B. MEASUREMENT OF MAGNETIC FIELDS.....	164
B.1	Theory.....	164
B.2	Experimental.....	165
	APPENDIX C. MODEL FOR THE DICHOIC SIGNAL OF THE 670.8 nm Li DOUBLET VERSUS FIELD STRENGTH.....	171
C.1	Calculation of the frequency shifts and intensities of the Zeeman components.....	171
C.2	Total intensity of the $\sigma$ and $\pi$ components.....	174
C.3	Computer program.....	177
	BIBLIOGRAPHY.....	188

## LIST OF FIGURES.

FIGURE 1.1 Simplified diagram of the process of absorption and emission of radiation. . . . .	3
FIGURE 1.2 Block diagram of the components of an atomic absorption system . . . . .	6
FIGURE 1.3 Simplified diagram of a Gaussian profile . . . . .	14
FIGURE 1.4 The normal Zeeman effect of the transition $1S_0 \text{ --- } 1P_1$ . . . . .	21
FIGURE 1.5 The Zeeman effect of the transition $2S_{1/2} \text{ --- } 2P_{3/2}$ . . . . .	24
FIGURE 1.6 Absorption profile of the 328.1 nm Ag line in presence of a transverse magnetic field . . . . .	25
FIGURE 1.7 Coupling of the momentum vectors of the atom with the external field . . . . .	27
FIGURE 1.8 Simplified description of the performance of the Zeeman background correction systems . . . . .	32
FIGURE 1.9 Some examples of Zeeman background-corrected systems . . . . .	36
FIGURE 2.1 Diagram of the field-on-source configuration used to measure the first and second harmonics . . . . .	48
FIGURE 2.2 Signal processing block diagram for the measurement of the first and second harmonics in the field-on-source configuration . . . . .	50
FIGURE 2.3 Second harmonic of the 585.2 nm neon (I) line versus coil position . . . . .	53
FIGURE 2.4 First harmonic of the 585.2 nm neon (I) line versus coil position . . . . .	54
FIGURE 2.5 First and second harmonics of the 377.7 nm neon (II) line versus coil position . . . . .	56
FIGURE 2.6 Second harmonic of the 670.8 nm lithium line versus coil position . . . . .	57
FIGURE 2.7 First harmonic of the 670.8 nm lithium line versus coil position . . . . .	58
FIGURE 2.8 Second harmonic of the 285.2 nm magnesium line versus coil position . . . . .	59
FIGURE 2.9 First harmonic of the 285.2 nm magnesium line versus coil position . . . . .	60
FIGURE 3.1 Block diagram of the instrument used to measure $b(0)$ , $a(1)$ , and $b(2)$ . . . . .	68
FIGURE 3.2 Diagram of the burner and the nebuliser . . . . .	69
FIGURE 3.3 Circuit diagram of the magnetic field supply . . . . .	70
FIGURE 3.4 Block diagram of the optical arrangement used in Zeeman scanning . . . . .	74

FIGURE 3.5 Dependence of the change in the absorbance of the lithium isotopes versus field strength.....	76
FIGURE 3.6 Harmonics of the lithium isotopes .....	77
FIGURE 3.7 Ratios of the harmonics of the lithium isotopes .....	79
FIGURE 3.8 Dependence of the change in the absorbance of Pt and Fe versus field strength .....	80
FIGURE 3.9 Harmonics of Pt and Fe .....	82
FIGURE 3.10 Ratios of the harmonics of Pt and Fe.....	84
FIGURE 4.1 Diagram of the discharge cell used in the Faraday configuration .....	88
FIGURE 4.2 Description of the switch for the magnetic field .....	90
FIGURE 4.3 Block diagram of the processing of the Zeeman, absorption, and emission signals. Faraday configuration.....	91
FIGURE 4.4 Time diagram of the discharge, the signal, and the magnetic field.....	93
FIGURE 4.5 Diagrams of the discharge cells used in the Voigt configuration .....	95
FIGURE 4.6 Block diagram of the processing of the dichroic signal. Voigt configuration.....	97
FIGURE 4.7 Block diagram of the processing of the emission signal. Preliminary measurement to the detection of the dichroic signal. ....	100
FIGURE 4.8 Decay of the copper emission at the 324.8 nm Cu line .....	102
FIGURE 4.9 Decay of the absorption and the Zeeman signals of the 324.8 nm Cu line .....	103
FIGURE 4.10 Absorption and Zeeman signals of the 324.8 nm Cu line versus discharge current .....	106
FIGURE 4.11 Emission at the 670.8 nm Li line versus discharge current in a pulsed discharge cell.....	107
FIGURE 4.12 Dependence of the dichroic signal of the 670.8 nm Li line on the duty cycle of the discharge cell .....	109
FIGURE 4.13 Dependence of the dichroic signal of the 670.8 nm Li line on the delay of the reference pulse. Discharge off 52% of the repetition period .....	110
FIGURE 4.14 Dependence of the dichroic signal of the 670.8 nm Li line on the delay of the reference pulse. Discharge off 24% of the repetition period .....	111
FIGURE 4.15 Dichroic signal of the 670.8 nm Li line versus field strength .....	113

FIGURE 4.16 Comparison of the dichroic signal produced by lithium vapour surrounded by a magnetic field and a quartz plate .....	114
FIGURE 5.1 Block diagram of the processing of the dichroic signal when the atomiser is a continuous discharge cell. Voigt configuration.....	118
FIGURE 5.2 Detail of the cell and the electric circuit used in the electrodeposition of lead ions on the electrode.....	122
FIGURE 5.3 Dichroic signal of Cu, Ag, Cd, Mg, and Ni versus RF current.....	129
FIGURE 5.4 Dichroic signal of Cu, Ag, Cd, Mg, and Ni versus field strength .....	132
FIGURE 5.5 Dependence of the dichroic signal of the 328.1 nm silver line on the time of deposition .....	136
FIGURE 5.6 Dependence of the dichroic signal of the 328.1 nm silver line on the concentration of the solution used to deposit the metallic silver .....	137
FIGURE 5.7 Dichroic signal of silver versus the amount of silver deposited on the electrode .....	140
FIGURE 5.8 Dependence of the dichroic signal of the 283.3 nm lead line on the RF current.....	143
FIGURE 5.9 Dependence of the dichroic signal of the 283.3 nm lead line on the field strength .....	144
FIGURE 5.10 Dependence of the dichroic signal of the 283.3 nm lead line on the length of electrodeposition .....	145
FIGURE B.1 Electronic device used to measure the strength of d.c. fields.....	168
FIGURE B.2 Calibration curves for the d.c. magnetic field used in the Voigt configurations.....	169
FIGURE C.1 Dependence of the dichroic signal on the frequency shift. Simulated data.....	178
FIGURE C.2 Dependence of the dichroic signal on the width of the absorption profile. Simulated data .....	179
FIGURE C.3 Dependence of the dichroic signal on the width of the source profile. Simulated data .....	180
FIGURE C.4 Dependence of the dichroic signal on the absorption profile. Simulated data .....	181
FIGURE C.5 Simulated and experimental data of dichroism versus field strength at the 670.8 nm Li doublet .....	182

## LIST OF TABLES.

TABLE 5.1 Selected wavelengths for atomic absorption and background absorption measurements.....	124
TABLE 5.2 Elements that showed a dichroic signal .....	128
TABLE B.1 Parameters used in field measurements.....	170
TABLE C.1 Program PB-AT2S.BAS .....	183

## SUMMARY.

The Zeeman effect which causes splitting of atomic lines has been applied in atomic absorption spectroscopy to correct for background absorption. In this study, two aspects of Zeeman background correction were investigated: (i) Fourier analysis of the response of the instruments using a.c. magnetic fields; (ii) application to discharge cells used as atomisers operated at atmospheric pressure.

Fourier analysis was applied to study the profiles transmitted by hollow-cathode lamps surrounded by a.c. fields (Faraday configuration). Self-absorption (and its frequency shift) inside the lamp affected the amplitudes of the first and second harmonics. The following lines were explored: 585.2 nm Ne, 377.7 nm Ne, 670.8 nm Li, and 285.2 nm Mg.

Another application of the Fourier analysis was in study of line overlap of absorbing species experiencing an a.c. field (Voigt configuration). The d.c. term, the first harmonic and the second harmonic (or their ratios) depended on concentration and were selective. The line overlap of Pt and Fe at 271.9 nm and the isotopic overlap of  $^6\text{Li}$  and  $^7\text{Li}$  at the 670.8 nm are reported.

Application of Zeeman background correction to discharges operating at atmospheric pressure was feasible. The use of the Faraday configuration imposed some limitations in design; the Voigt configuration was applied to metallic Al, Cd, Co, Cr, Cu, Fe, Pb, Mg, Ni, Ag, and Zn atomised directly, and to Ag and Pb solutions. The detection limit of the system for Ag and Pb was estimated from indirect determination of the amounts of these metals deposited on the electrode prior to the atomisation step.

## **ACKNOWLEDGEMENTS.**

The author is grateful to Dalhousie University for the Graduate Scholarship, to Dr. Roger Stephens for his supervision and orientation, to members of the Trace Analysis and Research Centre for their collaboration, and to all friends that provided suggestions and comments through the development of this research.

## **1. INTRODUCTION.**

In this work, the elimination or identification of background absorption by means of Zeeman background correction are the topics investigated. The technique is applied in order to identify spectral interferences and to eliminate background absorption in a discharge cell at atmospheric pressure.

This chapter introduces the reader to the topic by reviewing generalities about atomic absorption spectroscopy, background correction methods, sputtering cells in spectroscopy, use of electrodeposition in atomic absorption spectroscopy, and the theoretical principles involved.

### **1.1 ATOMIC ABSORPTION SPECTROSCOPY.**

#### **1.1.1 Principle.**

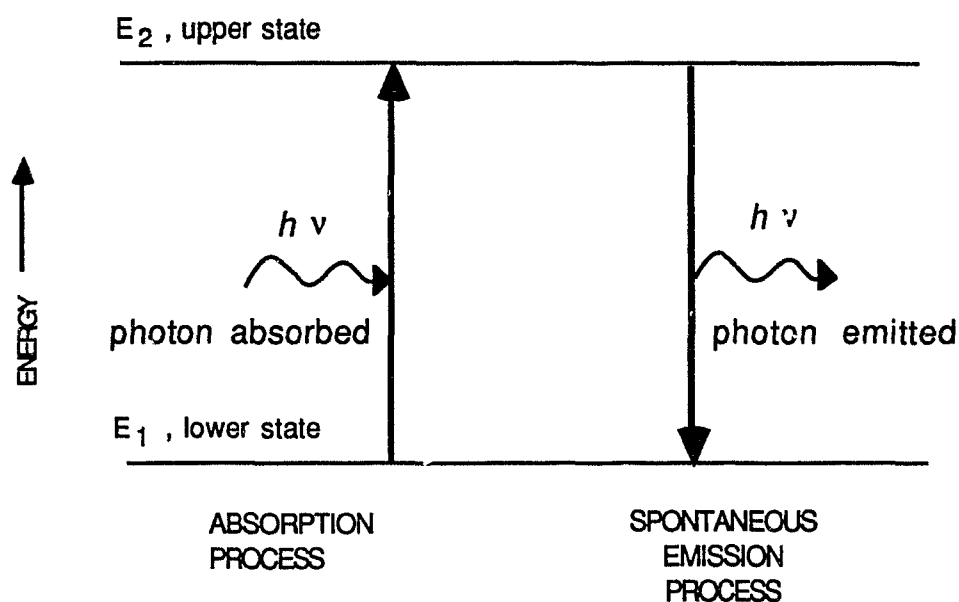
This technique is based on the absorption of radiation by a population of neutral atoms in the vapour phase. The amount of radiation absorbed by the vapour measures the concentration of the absorbing material. The wavelength at which absorption occurs has to provide selectivity, which is usually ensured by the narrow width of atomic spectral profiles.

After the radiation has been absorbed, the excited atom may decay back to the ground state, re-emitting radiation. This is the process called atomic fluorescence, which may occur at the same

frequency as that of the original absorption. The techniques of emission and fluorescence are also available as the basis of methods in analytical spectroscopy. Emission spectroscopy is a technique where the excitation is provided by collisional excitation (for instance in a flame or plasma) and the emission of the atomic species is measured at a specific wavelength. Atomic fluorescence spectroscopy is based on the excitation of the atomic population using a suitable intense source of radiation, and subsequent measurement of the emission of the atomic population. These techniques will not be covered since they are not directly related to the development of this project.

The process of atomic absorption occurs when an atom in a lower state is excited to an upper electronic state by absorbing a photon with energy  $h\nu$  which is equal to the energy difference of the two electronic states involved in the transition (Figure 1.1). Moreover, an atom in the upper state can relax to the lower state by emitting one photon with the same energy. A photon with a different energy will not correspond to a transition between these two states mentioned above, so the frequency (or the wavelength) of the photons being absorbed is determined by the energy levels of the atom. A more detailed description of the absorption process is presented by Mitchell and Zemansky [1].

**FIGURE 1.1** Simplified diagram of the process of absorption and emission of radiation.



The difference in energy between the two electronic states corresponds to the energy of the photon absorbed or emitted in the transition. This relationship can be expressed as  $E_2 - E_1 = h\nu = hc/\lambda$  where  $h$  is the Planck constant and  $c$  is the speed of light;  $\nu$  is the frequency and  $\lambda$  is the wavelength of the spectral line.

In addition to the specific energy of the photon, the probability of a transition between two electronic states is determined by their quantum nature; thus, certain selection rules must be obeyed. Only selection rules deduced from the evaluation of transitions involving the electric dipole moment are considered here. Transitions caused by quadrupole moments and magnetic dipole moments have low probability and are not important in this work. The selection rules derived for an electric dipole transition are: the change in  $J$  has to be  $\pm 1, 0$ ; the change in  $M_J$  has to be  $\pm 1, 0$ ; and, the change in the spin quantum number  $S$  has to be 0; the change in principal quantum number  $n$  does not have any restrictions. These rules are based on the assumption of a strong coupling between the **S** and **L** vectors. (Vectors and their magnitudes will be printed in bold type and plain type respectively). The selection rules are applied to determine the transitions between the energy levels of the Zeeman effect in section 1.2.

Using spectroscopic notation, the energy levels are represented by an electronic term denoted by  $^{2S+1}L_J$  where  $S$  is the magnitude of the total spin vector and  $2S+1$  is called the multiplicity of the state;  $L$  describes the total angular momentum and can be replaced by S, P, D, F, ... when  $L = 0, 1, 2, 3, \dots$  respectively; and  $J = |L+S|, |L+S-1|, \dots, |L-S|$  is the magnitude of the resultant vector of the Russell-Saunders coupling (**L** and **S** coupling). According to the selection rules described above, an allowed transition has to be of the general type:

$$2S+1L_J \longrightarrow 2S+1(L')_{J,J\pm 1} \quad (1)$$

Thus  $^1S_0 \longrightarrow ^1P_1$  and  $^3P_{3/2} \longrightarrow ^3P_{1/2}$  are allowed transitions, while  $^1S_0 \longrightarrow ^1P_{3/2}$  and  $^1P_1 \longrightarrow ^3P_{1/2}$  are forbidden transitions.

In general the atomic lines of absorption or emission spectra are represented as above. This nomenclature is used throughout this work.

### 1.1.2 Instrumentation.

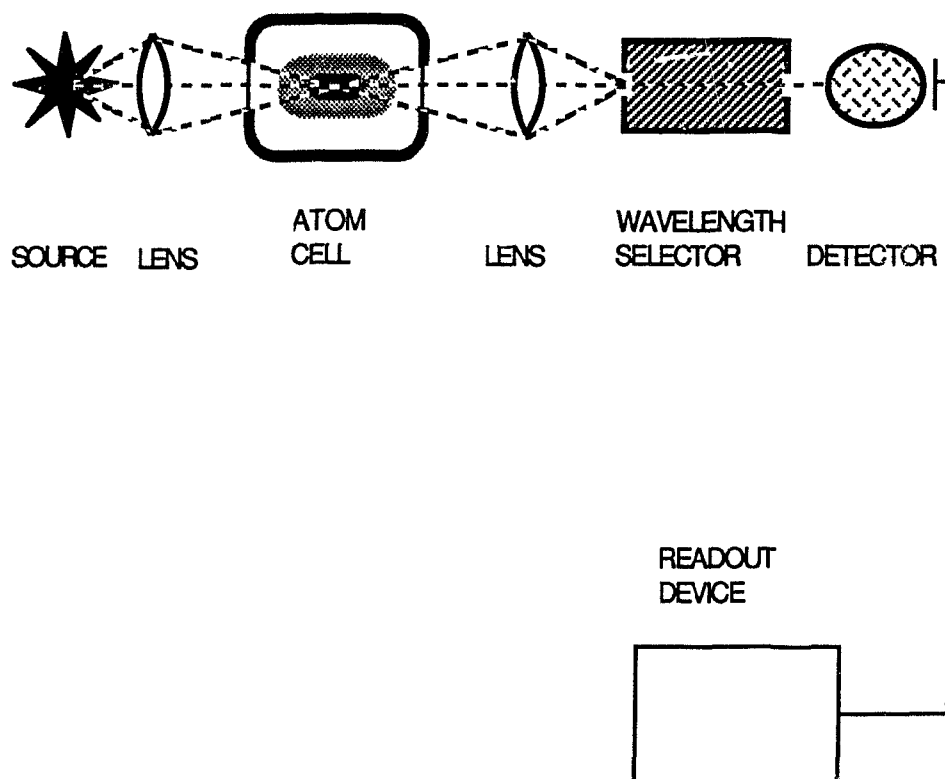
The basic components of an atomic absorption system are

- i. a source of radiation,
- ii. an atomic absorption cell,
- iii. a wavelength selector,
- iv. a detector,
- v. a readout device.

Figure 1.2 shows the scheme of the components of an atomic absorption system.

The source of radiation can be a continuous source, a hollow-cathode lamp or an electrodeless discharge lamp. The use of a hollow-cathode lamp for atomic absorption analysis is now widely

**FIGURE 1.2** Block diagram of the components of an atomic absorption system.



The lenses are chosen to direct as much light as possible through the region of maximum atom density and onto the detector system; the wavelength selector is placed directly in front of the detector to minimise stray light; the readout device also allows electronic discrimination against stray light.

accepted. Nevertheless, efforts are still made to use continuous sources for atomic absorption systems [2].

The atom cell could be a quartz cell at low temperature (for instance in Hg analysis), a flame, or a graphite furnace. In each of the methods, the atomisation occurs through different fundamental processes and the instrumentation is different [3].

The use of flames to produce an atom population is applicable to samples in solution. The sample is aspirated into a nebuliser which produces an aerosol in combination with the oxidant gas (for instance, air or  $N_2O$ ). The aerosol is then pre-mixed with the fuel gas (for instance, acetylene or propane) before it reaches the burner head where the flame is produced. The thermal energy of the flame will cause evaporation of the droplets of the solution and vaporisation of the material to produce the atom population. Therefore, the number of atoms present in the optical path depends on the efficiency of the processes of nebulisation and gas mixing, and on other parameters such as the oxidant/fuel ratio, which controls the composition and temperature of the flame, and the geometry and flow velocity of the flame, which control the residence time within the beam.

The use of graphite furnaces to produce an atom population is potentially applicable to either solid samples or solutions. The sample is placed or introduced into a graphite furnace filled with an inert gas (for instance, argon). The furnace is resistively heated and

controlled by a temperature programme. In the first stage, the temperature is just high enough to vaporise the solvent; in the second, it is raised to char the organic material and to break down complex salts; finally, the highest temperature provides the energy to vaporise the material and produce the atom population.

The wavelength selector may be a filter or a prism, but a diffraction grating is commonly used [4]. The diffraction grating has a large number of parallel grooves of constant separation. When radiation strikes the grating, it is dispersed in different directions and only a very narrow wavelength range forms an image on the exit slit placed in front of the photodetector. Except for the higher orders of the fundamental wavelength, other wavelengths will not be transmitted. By changing the position of the grating in relation to the incident radiation another wavelength can be selected.

A grating monochromator of low resolving power can be used in conjunction with a hollow-cathode lamp as a source of radiation since the resolving power of the instrument is sufficient to isolate the line of interest from stray light. However the use of a continuous source, or the presence of intense background emission, requires the use of an apparatus of high optical resolution. The result will be poor sensitivity unless the resolving power is high enough to isolate the narrow region where atomic absorption occurs from the unwanted background that may be transmitted over the whole bandpass of the monochromator.

Another device used to select a specific wavelength is the resonance detector. The radiation reaches a chamber filled with vapour of the element of interest instead of reaching the diffraction grating. The photomultiplier is at a right angle with respect to the optical axis and measures the fluorescent radiation resulting from the radiation reaching the resonance detector.

The detector is usually a photoelectric device [4]. It is made of a photo-conductive semi-conducting material which emits photoelectrons under illumination. The photoelectrons are directed to the dynodes which are responsible for an enhanced secondary emission of electrons. The number of electrons reaching the anode will produce an amplified electric response which can be readily processed.

### 1.1.3 History.

The first observations of atomic absorption spectra, other than those produced in the spectrum of the sun were done by L. Foucault in 1860 [5].

In 1875, J.N. Lockyer [6] studied the absorption spectra of metal vapours. He used a continuous source, a furnace heated by charcoal to produce the vaporisation of the metals inside an iron tube, and a spectroscope to detect the absorption.

In 1905, A.S. King made use of an arc-heated and a resistively-heated (in 1908) tubular graphite furnace to measure the emission

spectra and the absorption spectra of elements [6]. This furnace type is considered the precursor of the modern electro-thermal atomisers. In 1935-36, F.W. Paul reported the observation of the absorption spectra of rare-earth elements, Mn, and Ag using the King furnace as an atomiser [6]. In 1952-54 Garton and Bovey also used a King furnace to observe the absorption spectra of Cu, Ga, Lu, and Tl.

Up to this point in the evolution of the atomic absorption systems, the source of radiation was a continuous source in conjunction with an optical system of high resolving power. Sources included a 500-W tungsten filament lamp, the positive crater of a carbon arc, a hydrogen lamp, and a high-pressure xenon arc. The limitations in the source and the tedious photographic recording of the absorption spectra limited the use of atomic absorption for quantitative analysis.

The early applications of the atomic absorption technique were basically for spectroscopic investigations such as astronomical observations and measurement of oscillator strengths. Emission spectroscopy was preferred as a quantitative analytical technique. However, in 1953 the first patent in atomic absorption was registered by Walsh; two years later the former introduced the hollow-cathode lamp as a monochromatic source of radiation to provide an alternative to the continuous sources [7]. Also, in 1955, Alkemade and Milatz reported a spectrometer able to measure the absorption by sodium vapour in a propane-air flame when a sodium discharge lamp was used as a monochromatic source [8]. These

developments reduced the need for optical systems of high resolving power. In addition to the monochromatic sources, the availability of photodetectors of high sensitivity permitted the use of electronic rather than photographic detection. This combination provided the basis for instruments which were suitable for routine analytical measurements.

Atomic absorption instrumentation has proliferated in recent years [4, 9]. New designs and approaches are being evaluated, applications of basic spectrometer components are being extended to (and combined with) other techniques, and computerised data control and signal processing are flourishing. One review that deals with trends in instrumentation design for atomic absorption systems has been published recently [9].

#### 1.1.4 Absorption and emission profiles.

Knowledge of line profiles is relevant to atomic absorption measurements. The conventional parameter is the absorbance  $A$ , defined as

$$A = - \log \frac{I}{I^0} \quad (2)$$

where  $I^0$  is the intensity of the incident radiation and  $I$  is the radiation transmitted by the absorption cell. This transmitted

radiation is generally expressed as a function of the absorption coefficient  $K$ , the density of absorbing atoms  $N$ , and the pathlength  $L$ :

$$I = I^0 \exp (-KNL) \quad (3)$$

In general,  $I^0$ ,  $K$  and  $I$  have a finite width and are frequency dependent, say  $I^0(\nu)$ ,  $K(\nu)$ , and  $I(\nu)$ , respectively. The first one is called an emission profile and the second one is called an absorption profile. Their mathematical representation is presented below. The intensity of the source is then calculated by integrating the profile  $I(\nu)$  over the frequency interval determined by the frequency bandwidth  $w$  of the instrument:

$$I^0 = \int_w I(\nu) d\nu \quad (4)$$

The transmitted intensity is calculated from the convolution of the emission and absorption profiles over the bandwidth of the instrument as

$$I = \int_w I^0(\nu) \exp (-K(\nu) N L ) d\nu \quad (5)$$

In order to obtain a linear relation between absorbance and atom density in the absorbing medium, the source profile  $I(\nu)$  must be much narrower than the absorption profile  $K(\nu)$ . This makes  $K(\nu)$

almost constant over the entire source profile, say  $K(\nu) = k_0$  where  $k_0$  is a constant. Under these conditions, substitution of equations (4) and (5) in (2) leads to

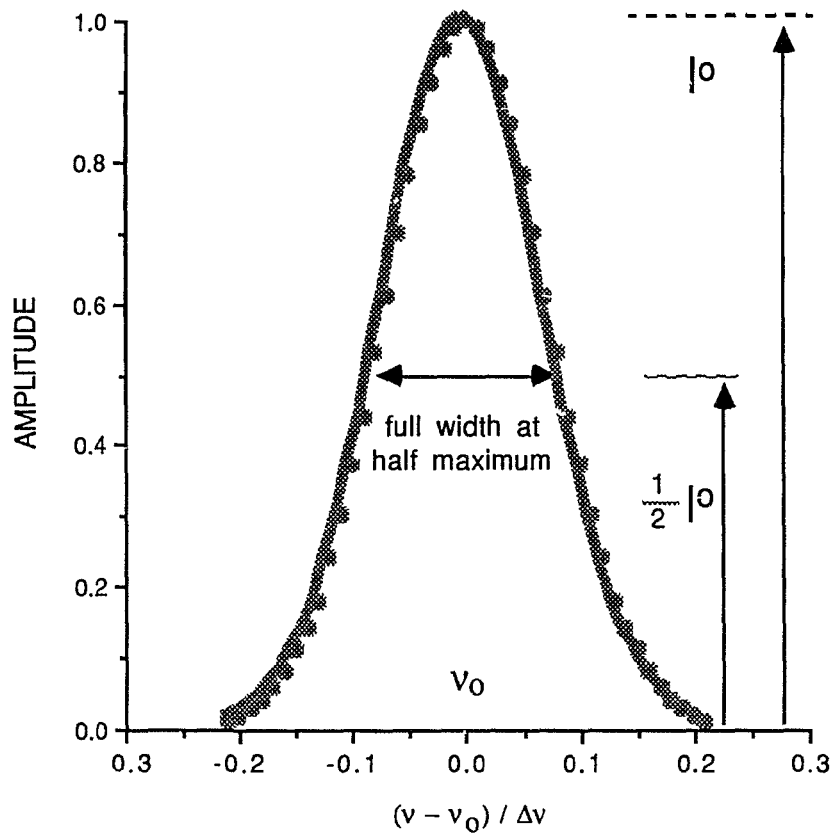
$$A = \log (\exp k_0 N \ell) = (\log e) (k_0 N \ell) = 0.43 k_0 N \ell \quad (6)$$

which shows a linear relation between absorbance and atom density. The correctness of this assumption is determined by the relative width of the source and the absorption profiles and by other factors such as stray light [4].

A useful way to characterise a line profile is by its full width at half the maximum value (Figure 1.3) which will be referred as line width or profile width hereafter. The occurrence of a minimum finite profile width is a direct consequence of the uncertainty of the energy levels of the corresponding electronic transition, which depends on the lifetimes of the states involved in such a transition [1]. Other parameters may produce further broadening:

- i. pressure, which produces further broadening caused by collisions with foreign gases (Lorentz effect), collisions with the same gas particles (Holtzmark effect), and collisions with charged particles (Stark effect);
- ii. temperature, which produces further broadening determined by the motion of the emitting or absorbing species (Doppler effect).

**FIGURE 1.3** Simplified diagram of a Gaussian profile.



Profiles can be described mathematically by Gaussian functions  $g(x) = A \exp(-[b (\nu - \nu_0) / \Delta\nu]^2)$ ; In this figure  $A=1$ ;  $b=1$ ;  $\nu$  is the frequency,  $\nu_0$  is the frequency at maximum amplitude, and  $\Delta\nu$  is the full width at half maximum

Emission and absorption profiles have been described by mathematical expressions that are a function of the frequency (or wavelength) of the radiation, usually Gaussian or Lorentzian curves. Different mathematical approaches, depending on the factor that contributes the most to line broadening, have been reported in the literature [1].

When the Doppler effect is dominant, and the other broadening processes are insignificant, the absorption coefficient  $k(\nu)$  at a determined frequency  $\nu$  is expressed by

$$k(\nu) = k_0 \exp \left[ -2 \sqrt{\ln 2} \frac{\nu - \nu_0}{\Delta \nu_D} \right]^2 \quad (7)$$

where  $\nu_0$  is the frequency of maximum absorption,  $k_0$  is the peak absorption coefficient, and  $\Delta \nu_D$  is the Doppler width.

Integrating  $k(\nu)$  from 0 to  $\infty$ ,  $k_0$  is found to be

$$k_0 = \frac{2}{\Delta \nu_D} \sqrt{\frac{\ln 2}{\pi}} \frac{\lambda_0^2}{8 \pi} \frac{g_1}{g_2} \frac{\mathcal{N}}{\tau} \quad (8)$$

where  $g_1, g_2$  are the statistical weights of the ground and excited states of the transition,  $\tau$  is the lifetime of the transition, and  $\mathcal{N}$  is the number of atoms in the ground state [1].

The Doppler width  $\Delta v_D$  is a function of the absolute temperature  $T$ , and the molecular mass  $M$ , and can be expressed by:

$$\Delta v_D = 2 \frac{\sqrt{2 R \ln 2}}{c} v_0 \sqrt{\frac{T}{M}} \quad (8)$$

where  $R$  is the gas constant, and  $c$  is the velocity of light.

Another approach is currently used when natural or pressure broadening is the most important factor. In this case,  $k(\nu)$  is expressed as

$$k(\nu) = k_0 \frac{1}{1 + \left[ 2(\nu - \nu_0) / \Delta v_L \right]^2} \quad (9)$$

where  $\Delta v_L$  is the summation of every broadening process which contributes to the profile width, including the natural broadening  $\Delta v_N$ . The latter is the reciprocal of  $2\pi$  times the lifetime  $\tau$  of the corresponding transition,

$$\Delta v_N = \frac{1}{2\pi \tau} \quad (10)$$

In general, Doppler broadening and Lorentz broadening may occur simultaneously. If it is assumed that both processes are independent, the mathematical expression which is widely used to describe the effect is the Voigt approximation of the line profile. A simplified approach to the problem is presented by Mitchell and Zemansky [1]. The expression they suggest is:

$$\frac{k(\nu)}{k_0} = \frac{a}{\pi} \int_{-\infty}^{+\infty} \frac{\exp(-y^2)}{a^2 + (b-y)^2} dy \quad (11)$$

where  $a$  (the damping ratio),  $b$ , and  $y$  are respectively:

$$a = \frac{\Delta\nu_L}{\Delta\nu_D} \sqrt{\ln 2} \quad (12)$$

$$b = 2 \frac{\nu - \nu_0}{\Delta\nu_D} \sqrt{\ln 2} \quad (13)$$

$$y = \frac{2\xi}{\Delta\nu_D} \sqrt{\ln 2} \quad (14)$$

where  $\xi$  represents the Doppler broadening of a frequency band at a distance  $\nu - \nu_0$  from the centre of the line showing only natural broadening.

In some cases, the profiles of sources of radiation show the effect of self-absorption caused by the re-absorption of radiation before it leaves the source. Under these circumstances the emission

profile is attenuated at its maximum frequency  $\nu_0$ , and in extreme situations, the re-absorption is strong enough to create secondary maxima at each side of the central frequency. A self-absorbed emission profile is also described by equation (5).

The formulae given above for the description of profiles are appropriate for lines which are completely resolved. However, common laboratory sources of radiation may show more than one overlapping line, and the overall profile is the summation of the profiles of the hyperfine components. For instance, Wagenaar and de Galan [10] use the summation of the individual components represented by Gaussian profiles and Voigt profiles to describe hollow-cathode lamp lines at low lamp currents and high lamp currents, respectively, and to simulate experimental profiles [11].

Absorption profiles in flames or other conventional atomisation devices are wider than for hollow-cathode emission lines as a result of collisional broadening and enhanced Doppler broadening [10]. The theory of collisional broadening predicts that a red shift will be observed as a result of adiabatic interactions. Wagenaar and de Galan [10] report damping ratio values, described in equation (12), of between 0.5 and 1.5 for eighteen electronic transitions (ten different elements). For the same transitions, they also describe red shifts of 20 to 30% of the collisional width of absorption profiles obtained with an acetylene-nitrous oxide flame.

The line profile in a flame or other atomisation device is also calculated as a summation of the individual components. Wagenaar and de Galan use Voigt functions for individual hyperfine components [10]. They assume that the collisional broadening and the line shift are equal for all the components in one transition and that all sorts of collisions are included in the damping ratio described in equation (12).

## **1.2 THE ZEEMAN EFFECT.**

### **1.2.1. Principle.**

When a magnetic field is applied to atomic species which are emitting or absorbing radiation, their respective emission or absorption lines split into a multiplet. This phenomenon is called the Zeeman effect [12]. The same number of components with the same relative intensities and frequency displacements are seen in both emission and absorption. Moreover, the line profile of each component is the same as that of the original zero-field line profile.

There are two types of Zeeman effect phenomena. One is called the normal Zeeman effect which is found in singlet lines of many-electron spectra. In a transverse magnetic field the normal Zeeman effect causes a spectral line to split into three components, two  $\sigma$  components which are shifted to either side of the zero field line, and one  $\pi$  component which shows no frequency shift. The other type of Zeeman effect is known as the anomalous Zeeman

effect, in which the effect of electron spin causes further splitting of each component of the normal triplet.

### 1.2.2. The normal Zeeman effect.

The displacement of the lines from the original frequency in the presence of a magnetic field  $H$  is dictated by the change in the energy levels of the electronic transition. In the case of the normal Zeeman effect, the change in energy  $\Delta E$  is predicted by the equation

$$\Delta E = \mu_B H \Delta M_J \quad (15)$$

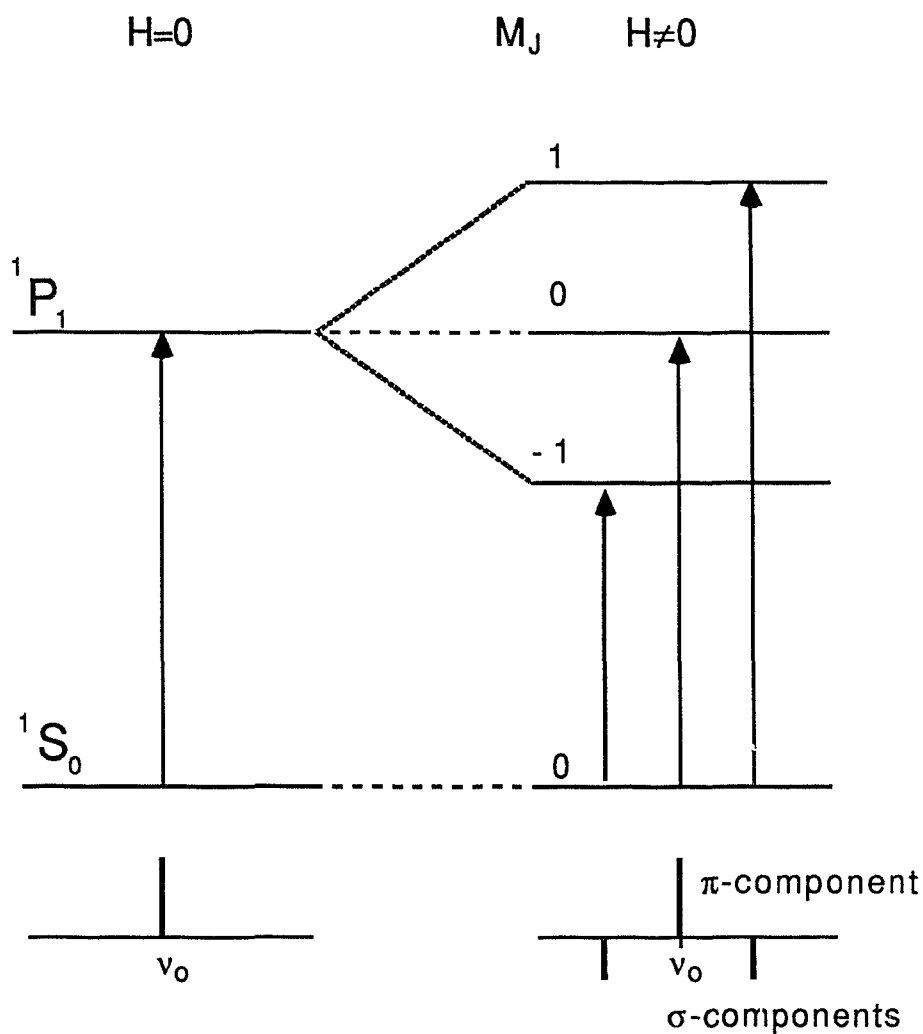
where the Bohr magneton  $\mu_B$  is calculated as

$$\mu_B = \frac{e}{4\pi m_e c} \quad (16)$$

$c$  is the velocity of light,  $e$  is the charge of the electron, and  $m_e$  is its mass.

The selection rules of an electric dipole transition require  $\Delta M_J = 0, \pm 1$ , and the corresponding components are named  $\pi$  and  $\sigma$  components, respectively. These components show a selective interaction with polarised radiation. In a transverse magnetic field (perpendicular to the optical axis), the  $\pi$  component interacts with or emits radiation which is polarised parallel to the direction of the magnetic field; such radiation is said to be  $\pi$  polarised. On the other hand,  $\sigma$  components show similar behaviour with respect to

FIGURE 1.4 The normal Zeeman effect of the transition  $^1S_0 \longrightarrow ^1P_1$



The transition in the presence ( $H \neq 0$ ) and absence ( $H = 0$ ) of a magnetic field is shown at the right and the left respectively; the displacement of the maximum frequency of each component is indicated at the bottom of each transition; the Zeeman splitting presents one  $\pi$ -component ( $\Delta M_J = 0$ ) which does not show a frequency displacement and two  $\sigma$ -components ( $\Delta M_J = \pm 1$ ).

radiation which is polarised perpendicularly to the magnetic field. In a longitudinal field the  $\pi$  components are absent and the  $\sigma$  components interact with or emit circularly polarised radiation; they are said to be  $\sigma_+$  or  $\sigma_-$  polarised.

Figure 1.4 shows the energy level diagram and the normal Zeeman splitting of the  $^1S_0 \rightarrow ^1P_1$  transition. The observed transitions are indicated by arrows and the corresponding spectral lines are shown at the bottom of the diagram. The selection rule  $\Delta M_J = 0, \pm 1$  is observed for the  $\pi$  components (above the frequency axis) and  $\sigma$  components (below the frequency axis) respectively. The two  $\sigma$  components have the same displacement from the original wavelength, while the  $\pi$  component is not displaced from the original wavelength. The total intensity of the  $\sigma$  components is observed to be equal to the intensity of the  $\pi$  component.

### 1.2.3. The anomalous Zeeman effect.

In the case of the anomalous Zeeman effect, the change of the energy levels is predicted by

$$\Delta E = \mu_B B \Delta(M_J g) \quad (17)$$

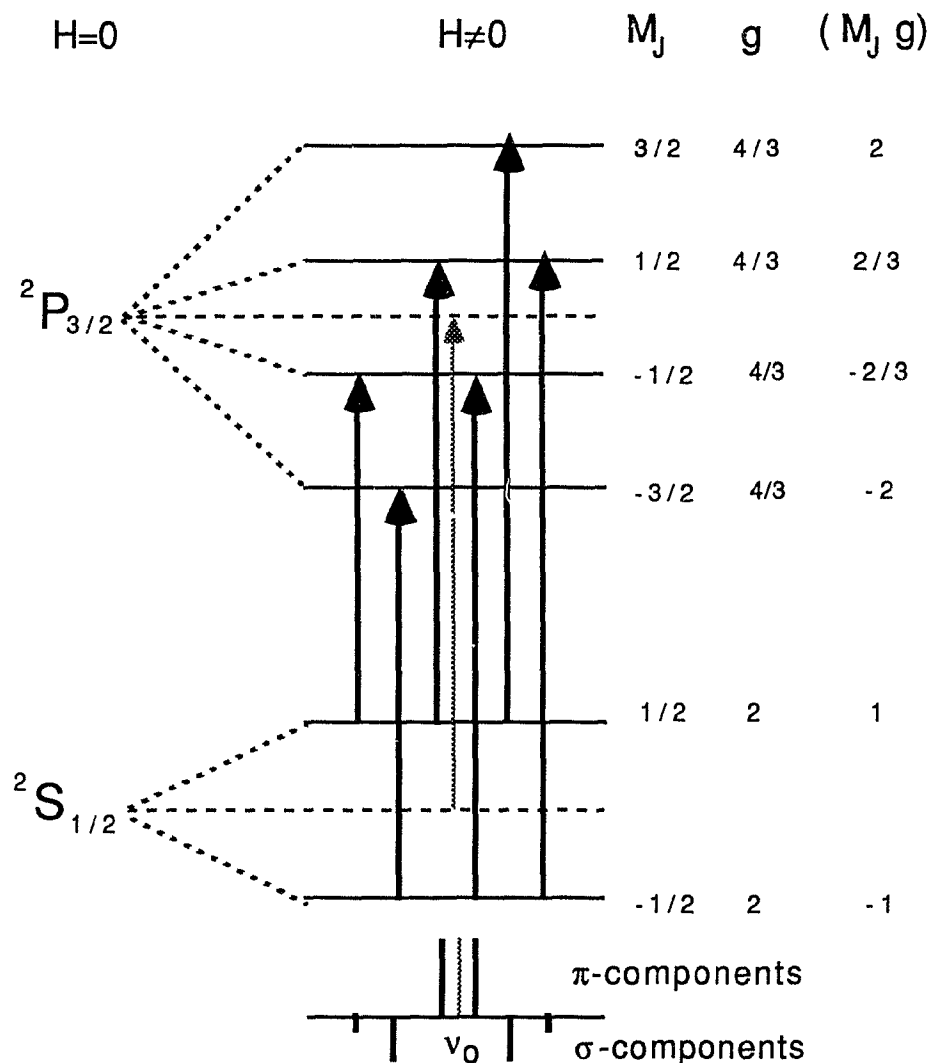
which is proportional to  $\Delta(M_J g)$ , the change in the product of  $M_J$  and  $g$ . The Landé factor  $g$  is the result from the quantised precession of  $\mathbf{J}$  around the field direction and is calculated as

$$g = 1 + \frac{J(J+1) + S(S+1) - L(L+1)}{2 J(J+1)} \quad (18)$$

Figure 1.5 shows the energy diagram and the anomalous Zeeman splitting of the  ${}^2S_{1/2} \longrightarrow {}^2P_{3/2}$  transition. The permitted transitions are indicated by arrows and the spectral lines are shown at the bottom of the energy level diagram. The corresponding  $\pi$  components (above the frequency axis) correspond to transitions with  $\Delta M_J = 0$  and  $\sigma$  components (below the frequency axis) correspond to transitions with  $\Delta M_J = \pm 1$ . Since the displacement from the original wavelength is controlled by the change in the product  $M_J g$ ,  $\pi$  components ( $\Delta M_J = 0$ ) as well as  $\sigma$  components ( $\Delta M_J = \pm 1$ ) are displaced from the original zero field wavelength. The displacement of both  $\pi$  and  $\sigma$  components is symmetrical about the original zero field line, the  $\pi$  displacements being, in general, less than the  $\sigma$  displacements. As with the normal Zeeman effect the total intensity of the  $\sigma$  components is equal to the total intensity of the  $\pi$  components. However, the intensities of each component in a particular polarisation state are not the same. The square of the transition probability of each component has to be calculated to estimate its relative intensity [13].

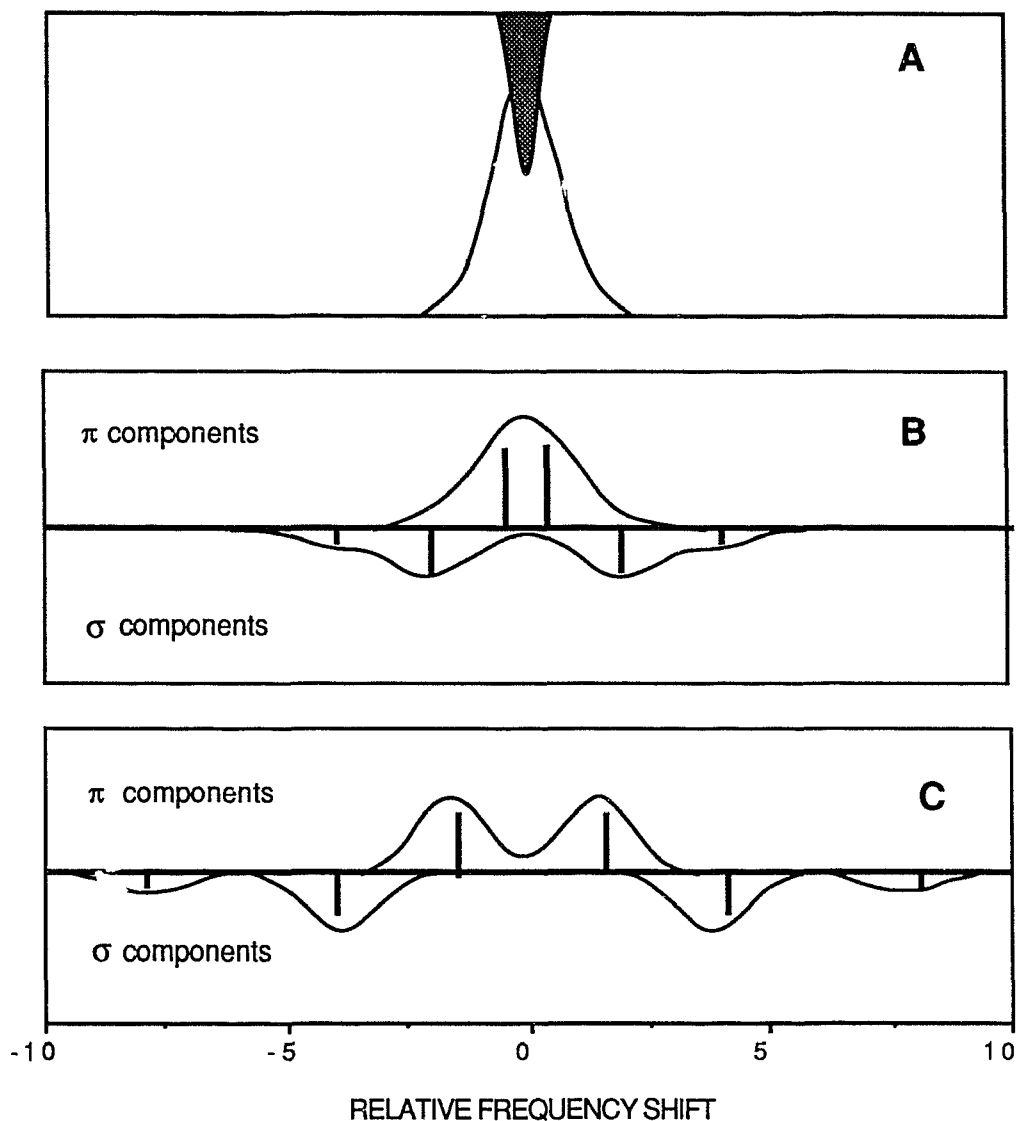
The effect of a magnetic field on the experimental absorption profile of the 328.1 nm Ag line in an air-acetylene flame is shown in Figure 1.6. The profile was recorded with a Fabry-Perot interferometer [10]. This transition shows an anomalous Zeeman effect. As the field strength is increased the profile broadens and

FIGURE 1.5 The Zeeman effect of the transition



The allowed transitions in the presence of a magnetic field ( $H \neq 0$ ) are shown by the arrows; the Zeeman multiplet has two  $\pi$ -components ( $\Delta M_J = 0$ ) and four  $\sigma$ -components ( $\Delta M_J = \pm 1$ ); the displacement from the maximum frequency  $\nu_0$  and the relative intensity of each component is shown at the bottom of the corresponding transition.

**FIGURE 1.6 Absorption profile of the 328.1 nm Ag line in presence of a transverse magnetic field.**



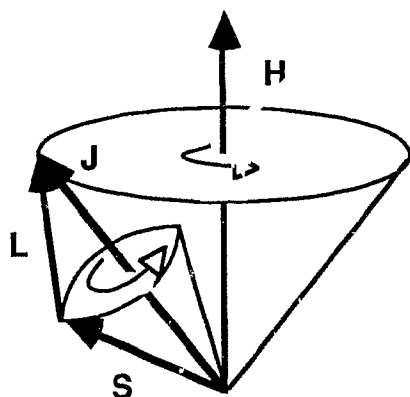
The field strength in A, B, and C is 0, 0.4, and 1.0 Tesla respectively; the source and absorption profiles are represented in gray and white respectively; the  $\pi$  and  $\sigma$  components are represented above and below the horizontal axis respectively; the maximum frequency and relative intensity of each component is indicated by a vertical line.

eventually shows the presence of Zeeman splitting. At 0.4 Tesla, the  $\sigma$  components (shown under the frequency axis) and the  $\pi$  components (shown above the frequency axis), are separated, as can be seen by the positions of the line centres (represented by the vertical lines). However, good resolution is lost due to the associated degree of line broadening. At 1.0 Tesla the magnetic displacements exceed the profile widths, and the individual  $\pi$  components and  $\sigma$  components can be resolved.

As shown in the examples above, the Zeeman effect is a function of the  $L$ ,  $S$ , and  $J$  vectors and not of the principal quantum number  $n$  or of the inner core electrons. This suggests that transitions for any elements can be classified in "Zeeman types" which will be determined absolutely in number, displacement, and intensity by the two terms of the transition regardless of which is the initial and which is the final state. For example the transitions  $4\ ^2P_{3/2} \longrightarrow 1\ ^2S_{1/2}$  of Na and  $5\ ^2S_{1/2} \longrightarrow 2\ ^2P_{3/2}$  of Cs belong to the same "Zeeman type" and will show similar behaviour in the presence of a magnetic field.

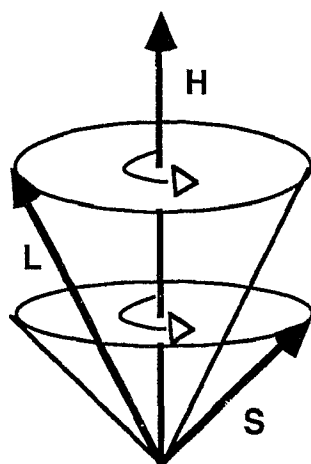
Zeeman splitting behaves in the manner described above when the magnetic field is not so strong that it destroys the coupling between the  $L$  and  $S$  vectors. Figure 1.7 shows a diagram of the precession of  $L$  and  $S$  around  $J$ , and of  $J$  around the magnetic field vector  $H$ . The precession of  $J$  is restricted, since its projection on  $H$  is quantised. If a strong magnetic field is applied, the splitting pattern changes as a result of an interaction of the field with  $L$  and

**FIGURE 1.7 Coupling of the momentum vectors of the atom with the external field.**



A

ZEEMAN EFFECT: STRONG  
L, S COUPLING.



B

PASHEN-BACK EFFECT: STRONG  
L,H AND S,H COUPLING.

The Zeeman effect is observed at moderate fields; **L** and **S** precess around **J** and the latter precesses around the external field **H** as shown in A. The Paschen-Back effect is observed when **L** and **S** precess individually around the strong external field **H** as shown in B.

**S** that is stronger than the interaction of **L** and **S** with each other. This phenomenon is known as the Paschen-Back effect.

### 1.3 BACKGROUND CORRECTION.

Atomic absorption is susceptible to spectral interferences which occur when the instrument fails to distinguish the absorption of the element of interest from the background absorption produced by some other species [14]. It is not unusual to find background absorption problems in the analysis of samples by atomic absorption, limiting its applicability.

Background absorption may be caused by light scattering due to solid particles in the atomiser, absorption by molecular rotational bands, such as the OH, NO, NO<sub>2</sub>, SO<sub>2</sub> absorption bands, and line overlap which, in some cases, occurs with resonance lines [14]. Except in the latter case, background absorption extends over a much wider frequency range than the atomic line. This has permitted the design of instrumentation to correct for background absorption. On the other hand, the detection of line overlap is more subtle and its correction is more complicated. Norris and West have reported the occurrence of 29 spectral overlaps in atomic absorption and 5 in atomic fluorescence [15]. The spectral overlap can be significant when the frequency separation between two resonance lines of two elements is as great as 0.05 nm.

Several approaches to eliminate background absorption in atomic absorption have been reviewed recently [9]. Background correction methods include continuous-source background correction, the Smith-Hieftje method, and Zeeman background correction. Ideally, each of the methods should provide the background absorption measurement at the same position in the atomiser as the gross absorption signal, at the same wavelength, and at the same time as the atomic absorption signal. The limitations of each of these methods are discussed below.

#### 1.3.1 Continuous-source background correction.

The first method used for background correction employed a continuous source, usually a deuterium arc lamp [14]. This method relies upon two measurements:

- i. a narrow-band measurement of the total absorption (the element plus the background absorption) using an atomic line from a hollow-cathode lamp as the source,
- ii. a broad band measurement, determined by the spectral bandwidth of the optical system, using a continuous source. Here background absorption is basically determined.

Subtraction or division of the two measurements provides the absorption by the element alone. The method is applicable when the background absorption is due to either molecular absorption or scattering of the radiation by solid particles. It should not be used

when the absorption is due to spectral overlap of concomitant elements.

Some disadvantages of this method are that it requires use of a double beam optical system and that careful optical alignment is needed to balance optical intensities of the two sources. In practice, the efficiency of the technique is limited because it is never possible to produce an identical matching of beam geometry and intensity distribution over the wavefronts for the two sources.

### 1.3.2 The Smith-Hieftje method.

This method is based on two measurements of absorption using a two-step pulse lamp current mode [16]. In the first step, the lamp is driven by a low current pulse. During this time the atomic absorption plus the background absorption are measured. The second step of the pulse is at a high lamp current, which is characterised by a broader, strongly self-absorbed emission profile. The intensity of the self-absorbed profile at  $\nu_0$  is greatly reduced in comparison to the wings, say at  $\nu_0 \pm \delta$ ; thus the background absorption measurement at  $\nu_0 \pm \delta$  remains unaffected while the atomic absorption is insignificant at  $\nu_0$ . The difference (or ratio) of the absorbance signals which are observed for the two pulses provides the background-corrected atomic absorption measurement.

The optical instrumentation required in this method is the same as in the conventional atomic absorption spectrometer, but the processing of the electronic signals and the modulation of the

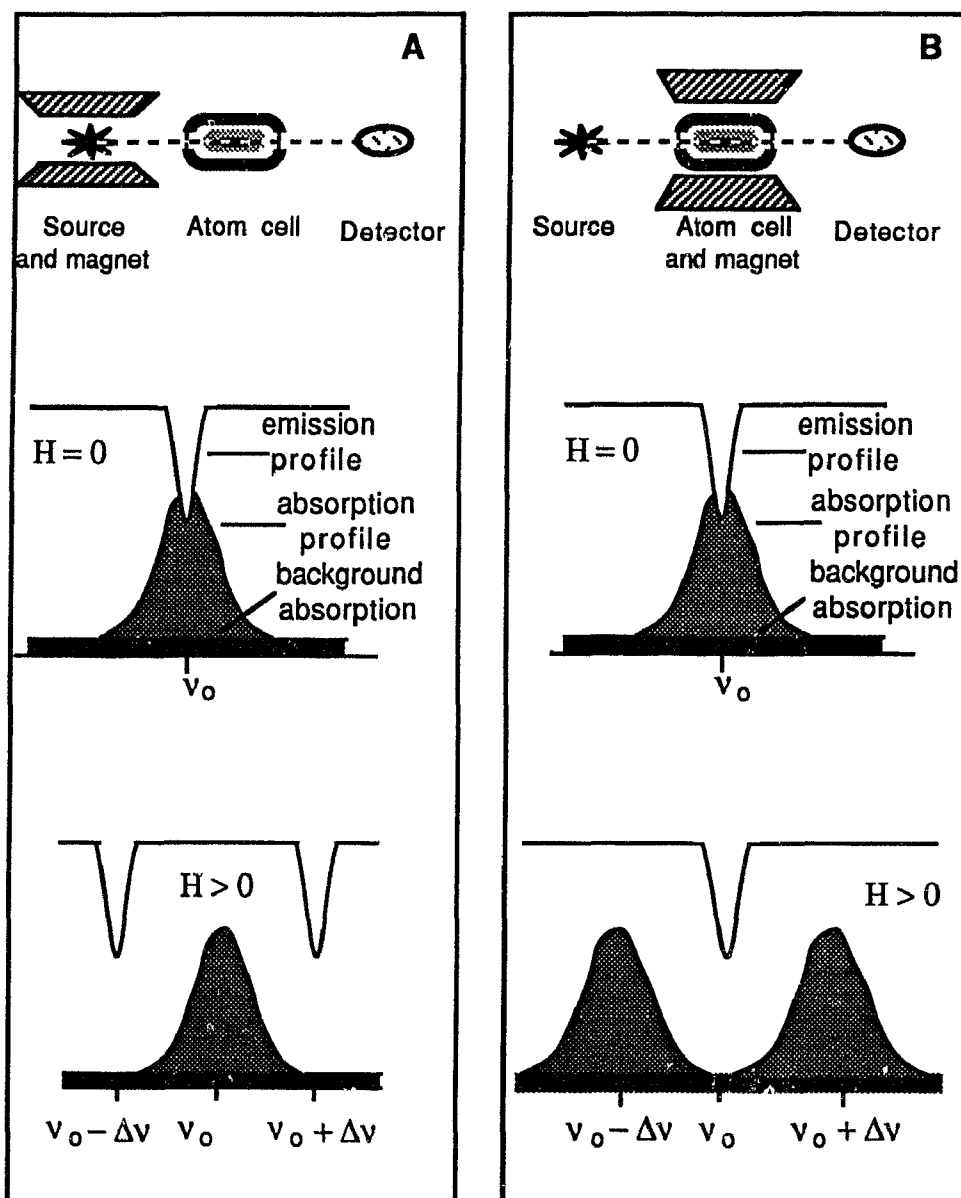
hollow-cathode lamp is more complex. In addition, the double pulse has to be adjusted for each lamp due to the different sputtering and spectroscopic profiles of the elements of interest. This method is effective in correcting for background absorption caused by particle scattering or band absorption. It is suggested that the method is effective in correcting a background due to spectral overlap, provided a suitable step pulse is selected to modulate the lamp [16].

### 1.3.3 Zeeman background correction.

The Zeeman effect is used in atomic absorption spectroscopy as a device for background correction [14,17]. It has been proved to be superior to continuous-source lamp correction when the background absorption is caused by light scattering or rotational bands which do not experience strong Zeeman splitting. In addition to offering a single-beam optical system, the method has the advantage that the background correction is effected essentially at the wavelength of the undisturbed source line.

Two general types of Zeeman correction have been employed using instruments in which the field is applied (i) to the source, (ii) to the atomiser. The spectroscopic advantages of one arrangement over the other depend upon the nature of the background. A qualitative comparison between the two systems is shown in Figure 1.8. Systems with the field applied to the source correct for the background at a slightly different wavelength from the absorption line, since the  $\sigma$  components of the emission profile are selected.

**FIGURE 1.8** Simplified description of the performance of the Zeeman background correction systems.



The application of the magnetic field to the source of radiation or to the atomiser causes splitting of the emission (A) or absorption profile (B), respectively; background absorption is determined at  $\Delta\nu$  from, or at  $\nu_0$  respectively; only the  $\sigma$  components are shown.

This system is effective even when the background absorption shows Zeeman splitting.

When the field is applied to the atomiser, the background correction is carried out at exactly the same wavelength as that of the zero field line. However, the measurement is susceptible to error if the background shows a Zeeman effect. Examples include radicals and molecules such as OH, NO, NO<sub>2</sub>, SO<sub>2</sub>. Restrictions on the application of Zeeman background correction due to this cause have been published [14, 18-24].

The Zeeman background correction method is usually compromised when the background absorption is a consequence of line overlap [19]. Neither configuration is able to effect the background correction in this case unless a specific field is chosen to eliminate the background interference [25].

A case related to atomic line overlap involves spectral overlap of different isotopic lines, observed when an element absorbs the radiation emitted by a source of different isotopic composition. For instance, the spectral overlap of lithium isotopes has been used in conventional atomic absorption spectroscopy to determine <sup>6</sup>Li and <sup>7</sup>Li using natural and <sup>6</sup>Li enriched hollow-cathode lamps [26-29]. Obviously, Zeeman background correction is not effective when the background absorption is due to another isotope of the element of interest.

#### 1.3.4 Theory of Zeeman atomic absorption spectrometers.

Different systems have been described in the literature [14]. The magnetic field in a Zeeman background correction system may be either longitudinal (Faraday configuration) or transverse (Voigt configuration) to the optical axis. The fields then can be either a.c. or d.c. The orientation of the field determines the nature of the splitting, as discussed in section 1.2. The transverse configuration is the most common, because the design of the optical system is correspondingly simplified, although it requires a polariser to block the  $\pi$  components. Figure 1.9 shows the diagram of some Zeeman atomic absorption systems.

The theoretical description of a system with the atomiser surrounded by a magnetic field is presented here. It shows qualitatively the way in which background is eliminated. A more comprehensive description of the Zeeman atomic absorption systems is most easily carried out by use of Jones calculus (Appendix A). This theoretical approach will be applied when required.

The following assumptions are usually made when describing the response of Zeeman corrected instruments [14]:

- i. the spectral bandwidth is wide enough to pass all relevant radiation without significant perturbation, even in a strong magnetic field;

ii. the source line and absorption line are considered to be symmetrical and the source line to be narrower than the absorption line. When a magnetic field is applied to either the source of radiation or the atomiser, the line profile of each component of the multiplet components remains the same as that of the zero field line;

iii. stray light is negligible;

iv. the emission signal from the atomiser has been eliminated, by modulation of the source of radiation for instance.

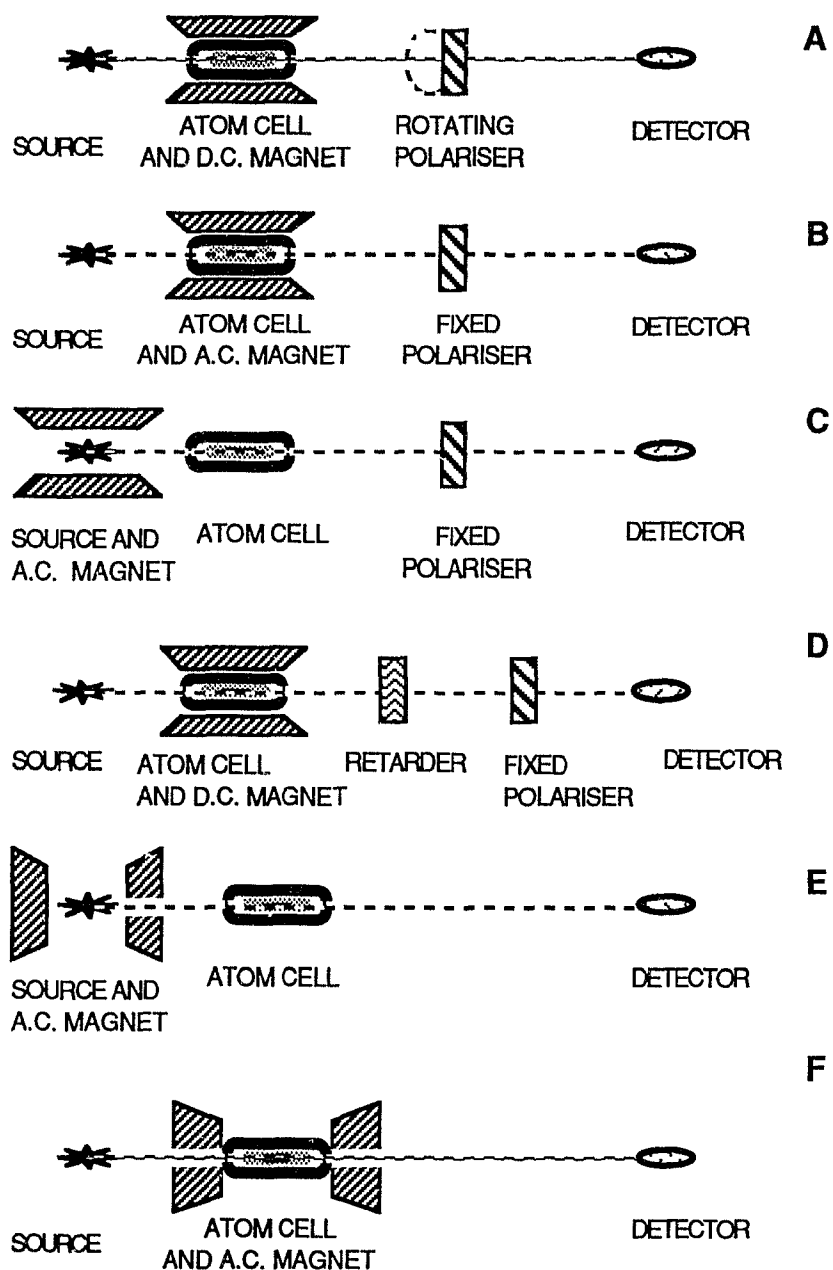
In a system with a transverse magnetic field around the atomiser, the  $\pi$  polarised,  $\sigma$  polarised, and zero field intensities are given by:

$$I_{\pi} = \int_w \frac{I^0(\nu)}{2} [\exp\{-\sum_{i=1}^n a_{K_{\pi;j}(\nu)} N \ell - b_{K_{\pi;j}(\nu)}\}] d\nu \quad (19)$$

$$I_{\sigma} = \int_w \frac{I^0(\nu)}{2} [\exp\{-\sum_{j=1}^{n'} a_{K_{\sigma;j}(\nu)} N \ell - b_{K_{\sigma;j}(\nu)}\}] d\nu \quad (20)$$

$$I_{H=0} = \int_w I^0(\nu) \exp\{-a_K(\nu) N \ell - b_K(\nu)\} d\nu \quad (21)$$

**FIGURE 1.9** Some examples of Zeeman background corrected systems.



The magnetic field can be transverse (A-D) or parallel (E-F) to the optical axis. The field could also be applied to the source in A and D.

Where  $I^0(\nu)$  is the intensity of the source and  $K(\nu)$  is an absorption coefficient;  $a$  or  $b$  represents the analyte or the background;  $\pi$  or  $\sigma$  represents the polarisation state of the  $i$ th or  $j$ th component of the multiplet; and  $N$  and  $l$  are the atom density and pathlength, respectively (see equation (5)).

The difference in absorbance between two polarisation states can be measured with a rotating polariser in a d.c. field or by comparing the signals in the ON and OFF cycle of an a.c. field.

In order to derive the associated signal of conventional Zeeman spectrometers, a narrow source profile, as in equation (6), is assumed. Under this condition, the absorption coefficient is basically constant over the source profile ( $aK(\nu)Nl = a_kNl$  and  $bK(\nu) = b_k$  where the right sides of the equalities are constants). The logarithm of the ratio of the intensities in the presence and absence of absorption in equation (21) is the signal  $S$  of a conventional instrument. This signal is represented as:

$$S = \log \left[ \frac{I^0}{I_{H=0}} \right] = 0.43 (-a_kNl - b_k) \quad (22)$$

Similarly the ratio of the logarithm of the equations (19) and (20) gives the Zeeman background-corrected signal as:

$$S_2 = \log \left[ \frac{I_\sigma}{I_\pi} \right] = 0.43 \left\{ \sum_{i=1}^n a_{k\pi;i} N_i - \sum_{j=1}^{n'} a_{k\sigma;j} N_j \right\} \quad (23)$$

where the atomic and background absorption of each component is assumed to be constant over the narrow width of the source profile ( $a_{K\sigma;j}(\nu) = a_{k\sigma;j}$  and  $a_{K\pi;i}(\nu) = a_{k\pi;i}$ ; the right sides of the equalities are constants). In addition, the background absorption is independent of the state of polarisation for every component of the multiplet ( $b_{K\pi;i}(\nu) = b_{K\sigma;j}(\nu) = b_k$ ).

The absence of background absorption in the response signal of the Zeeman system is shown in equation (23). This description is equally applicable in the case of the Faraday configuration, where the ratio of the logarithm of equations (20) and (21) leads to:

$$S_3 = \log \left[ \frac{I_\sigma}{I_{H=0}} \right] = 0.43 \left( a_k - \sum_{j=1}^{n'} a_{k\sigma;j} \right) \quad (24)$$

Moreover, a system with the field-on-source configuration can be described in a similar way to the field-on-atomiser configuration. Description of such a system is not included here.

#### 1.4 SPUTTERING CELLS IN SPECTROSCOPY.

Atomic vapours can be produced not only by flames and furnaces but also by sputtering, which in principle is applicable to all metallic elements irrespective of their melting point [30].

Sputtering cells have been used both as emission sources and for the production of atomic vapours.

Applications for the production of atomic vapours by sputtering include atomisation cells, resonance monochromators and optical filters [30, 31].

Applications of sputtering cells as emission sources include the hollow-cathode lamp and the Grimm discharge lamp in which the filler gas is kept at low pressure. The successful use of low pressure sputtering cells has been reviewed [3]. The advantages described in that review include an increased linear range of working conditions and a versatile excitation source for a wide range of metals; the major disadvantage is the strong emission of radiation in the visible and ultra-violet region of the spectrum, reducing the signal-to-noise ratio as a result of the random noise. Matsuta and Hirokawa [31] have reported an approach to eliminate this problem. The discharge is switched off periodically and the absorption measurement is delayed until background emission is absent. This is possible since the lifetime of the ground state population is relatively longer than of the emission of the discharge. Other related problems are the need for a particular gas, a specific power supply, and a low operating pressure.

Advances in atmospheric pressure discharge cells have been published recently [32]. Stephens uses a discharge cell operating up to or slightly above atmospheric pressure and filled with helium

gas. The selection of helium to fill the cell stops the discharge from quenching or changing to a spark or an arc. This design permits measurements of emission and absorption of several elements, although some elements cannot be atomised due to the formation of a stable oxide layer on the surface of the electrode.

### **1.5 ELECTRODEPOSITION AS A PRECONCENTRATION TECHNIQUE IN ATOMIC ABSORPTION SPECTROSCOPY.**

Electrodeposition has been used as a preconcentration technique in conjunction with different analytical methods [33, 34]. Some of its advantages are that it can separate trace metals from interfering matrix components, improve detection limits, enhance accuracy, ease calibration procedures, and allow the use of increased sample sizes [33].

Electrodeposition has been combined with atomic absorption spectroscopy, mainly with the use of a graphite furnace as the atomiser [35-39]. The method has been quite successful, since electrodeposition can selectively preconcentrate the species of interest, lower the detection limit and eliminate the matrix interferences usually found in flameless atomic absorption. In addition, it can be effected directly onto the inner wall of the graphite furnace tube when the latter is used as the cathode of an electrolytic cell. When the elements have low atomisation temperatures electrodeposition can also be done on a tungsten wire which is then inserted into a preheated miniature furnace [38]. A tungsten-rhenium wire loop atomiser [40], a carbon rod atomiser

[41], and an argon-hydrogen flame [42] have also been used as atomising devices following the electrodeposition step.

The elements that have been analysed by the combination of electrodeposition and atomic absorption include Ag, As, Au, Be, Cd, Co, Cr, Cu, Fe, Hg, La, Mg, Mn, Ni, Pb, Sb, Se, Sn, V, and Zn in matrices such as sea water, natural water, beverages, urine, and digested biological samples [35-41]. In these cases, the electrodeposition time has varied from 30 seconds to 60 minutes.

In order to improve the efficiency of the electrodeposition step, several conditions and parameters have been investigated. Some authors use a continuous flow through the graphite tube during the deposition process [37, 38], while others use a confined electrolytic cell to deposit the element [40, 42]; the advantages and disadvantages of each approach depend on the other experimental conditions and on the requirements of the analysis. The selection of a particular cathodic potential is important in speciation studies when only a particular species has to be deposited [36] and when the presence of oxygen shifts the reduction potential [35]; otherwise, the selection of a deposition potential will affect only the maximum amount of material that can be deposited on the electrode [43] and the speed at which deposition takes place. In one particular case, Newton observed spontaneous preconcentration in the absence of an applied potential [40], which was attributed to an ion exchange process.

A model that accounts for the experimental observations has been proposed by Sioda [43] and confirmed experimentally for Cu and Pb by Ciszewski et. al. [33]. The model is based on the kinetics of formation and dissolution of the metallic deposit on the electrode. The kinetic equation for the process is:

$$dC/dt = -s(k_1C - xk_2) \quad (25)$$

where  $dC/dt$  is the rate of change of the concentration of the solution,  $s = A/V$  (area of the electrode/volume of solution) is the specific area of the electrolytic cell,  $k_1$  is the mass-transport coefficient of the reduction-deposition process,  $x$  is the fraction of total area covered by the metal deposit, and  $k_2$  is the specific rate of deposit dissolution. The first term of this equation refers to the formation of the deposit, which is a first order reaction. The second term of the equation refers to the rate of dissolution. The specific rate of deposit dissolution depends upon the metal itself and upon the oxidative and complexing power of the solution. Traces of oxidants such as oxygen, chlorine, nitric acid, and anodic products inevitably affect the value of  $k_2$ . Predictions of the concentrations at equilibrium, of the percentage of recovery, and of the time required to reach equilibrium can be made using this model. The predicted equilibrium concentrations are similar to their corresponding experimental values, while the predictions based solely on the Nernst equation are much lower [33]. Another important prediction is the dependence of the equilibrium concentration on the original concentration when the amount of original material in solution is not large enough to form such a

monolayer on the surface of the electrode [43]. On the other hand, if this amount is more than enough to form an atomic monolayer, the equilibrium concentration equals  $k_2/k_1$  and is independent of the original concentration.

Stirring speeds up the electrolysis in all cases, reducing the time required to achieve a fixed percentage of recovery, but it does not have a significant influence on equilibrium concentration; pH may also affect the electrodeposition process, but its influence is different for each element.

## 2. HARMONIC ANALYSIS OF A FIELD-ON-SOURCE CONFIGURATION

### 2.1 PURPOSE.

Air-cored solenoids have been successfully used to produce alternating magnetic fields on commercial hollow-cathode lamps [25, 44, 45] facilitating the Zeeman background correction method in field-on-source configurations. As explained later (Chapter 3), Zeeman scanning, attained by use of an alternating magnetic field, provides information about the Zeeman multiplet. In this work, Fourier analysis is used to extract information about the transmitted profile of the source, which in turn depends upon the emission and the self-absorption profiles.

In order to understand the way in which Fourier analysis reveals information about the transmitted profile of the source, the following model, based on the normal Zeeman effect, is adopted. The profiles are described by Gaussian functions (Doppler broadening) and hyperfine structure is ignored. The alternating magnetic field is chosen to be parallel to the optical axis (Faraday configuration); thus  $\pi$  components are absent. In the presence of a magnetic field,  $H$ , the emission profile  $I(\nu)$  is split into its  $\sigma_+$  and  $\sigma_-$  components,  $I_{\sigma_+}(\nu)$  and  $I_{\sigma_-}(\nu)$  respectively. They are:

$$I_{\sigma\pm}(\nu) = \frac{I_0}{2} \exp \left[ -2 \sqrt{\ln 2} \frac{\nu - \nu_s \pm 14H}{\Delta\nu_s} \right]^2 \quad (26)$$

and  $I(\nu)$  can be expressed as

$$I(\nu) = I_{\sigma+}(\nu) + I_{\sigma-}(\nu) \quad (27)$$

where  $I_0$  is the peak intensity at the source centre frequency  $\nu_s$ ,  $\Delta\nu_s$  is the width of the emission profile, and  $14H$  is the frequency shift due to the Zeeman effect (section 1.2).

Similarly, in the presence of a magnetic field  $H'$  (which may be different from the field strength experienced by the emission profile  $H$ ), the self-absorption coefficient  $K_{sa}(\nu)$  can be expressed by the sum of its  $\sigma_+$  and  $\sigma_-$  components,  $K_{sa,\sigma+}(\nu)$  and  $K_{sa,\sigma-}(\nu)$  respectively. They are:

$$K_{sa,\sigma\pm}(\nu) = \frac{K_{0,sa}}{2} \exp \left[ -2 \sqrt{\ln 2} \frac{\nu - \nu_{sa} \pm 14H'}{\Delta\nu_{sa}} \right]^2 \quad (28)$$

and  $K_{sa}(\nu)$  can be expressed as

$$K_{sa}(\nu) = K_{sa,\sigma+}(\nu) + K_{sa,\sigma-}(\nu) \quad (29)$$

where  $K_{0,sa}$  is the maximum coefficient of self-absorption at the absorption centre frequency  $\nu_{sa}$ ,  $\Delta\nu_{sa}$  is the width of the self-absorption profile, and  $14H'$  is the frequency shift due to the Zeeman effect (section 1.2).

According to the model, the transmitted profile, which corresponds to the response of the system used in this work (see Appendix A), is obtained by combining equations (26-28) and integrating over the optical bandwidth  $w$  of the instrument (see section 1.1). The signal associated with the intensity at the detector is

$$I = \int_w \{I_{\sigma+}(\nu) + I_{\sigma-}(\nu)\} \{\exp-[K_{sa,\sigma+}(\nu) + K_{sa,\sigma-}(\nu)]N_{sa} l_{sa}\} d\nu \quad (30)$$

where  $N_{sa}$  and  $l_{sa}$  are the density of atoms and the pathlength responsible for the self-absorption of the source line.

When the fields  $H$ ,  $H'$  are sinusoidal the signal  $S$  described in equation (30) may be expressed by a Fourier series (see equations (35-37); Chapter 3). For now only the following qualitative comments will be given.

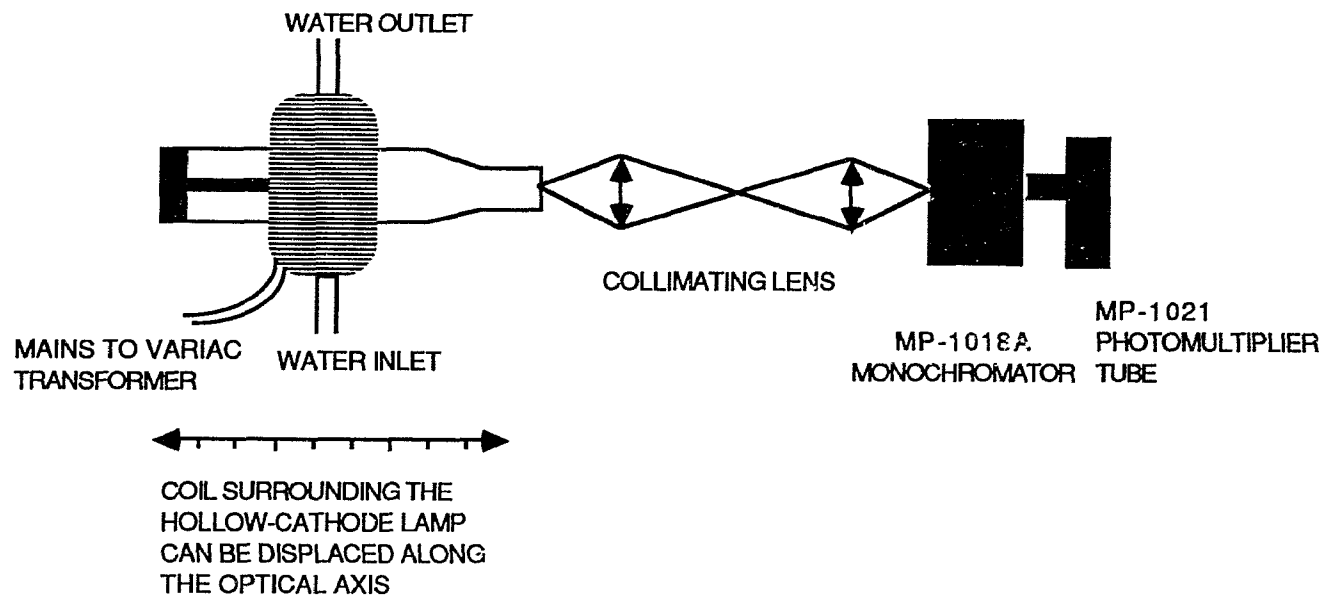
The first and second harmonics depend on the overlap of the emission and self-absorption profiles and are functions of the variables of the equation (30):  $N_{sa}$ ,  $l_{sa}$ ,  $H$ ,  $H'$ ,  $\Delta\nu_{sa}$ ,  $K_{0,sa}$ ,  $\nu_{sa} - \nu_s$ . Their origin can be simply explained in terms of the symmetry of the

Zeeman multiplet of the aforementioned profiles. When the symmetry is conserved between the  $\sigma_+$  and  $\sigma_-$ -components of the transmitted profile, only even harmonics are detected (for instance, the second harmonic). This condition is met in the absence of self-absorption ( $K_{sa}(\nu)N_{sa}L_{sa} = 0$ ), or when there is no frequency shift ( $\nu_{sa} - \nu_s = 0$ ) between the emission and self-absorption profiles at zero field strength.

In order to detect an odd harmonic (for instance, the first harmonic) an asymmetry must exist between the  $\sigma_+$  and  $\sigma_-$  components of the transmitted profile. The asymmetry is the result of either (or both) of: (i) a shift between the maximum frequencies of self-absorption  $\nu_{sa}$  and emission  $\nu_s$  profiles at zero field; (ii) a different field strength at the emitting and self absorbing regions of the hollow-cathode lamp ( $H \neq H'$ ). Thus the existence of self-absorption is essential for the detection of the first harmonic.

The purpose of this experiment was the comparison of the behaviour of the first and second harmonics of 670.8 nm Li, 285.2 nm Mg, 585.2 nm Ne(I), and 377.7 nm Ne(II) lines at different field strengths. The displacement of the solenoid along the axis of the hollow-cathode lamp was used to vary the field strength at the cathode and to provide characteristic harmonic signals at each position along the lamp axis.

**FIGURE 2.1** Diagram of the field-on-source configuration used to measure the first and second harmonics.



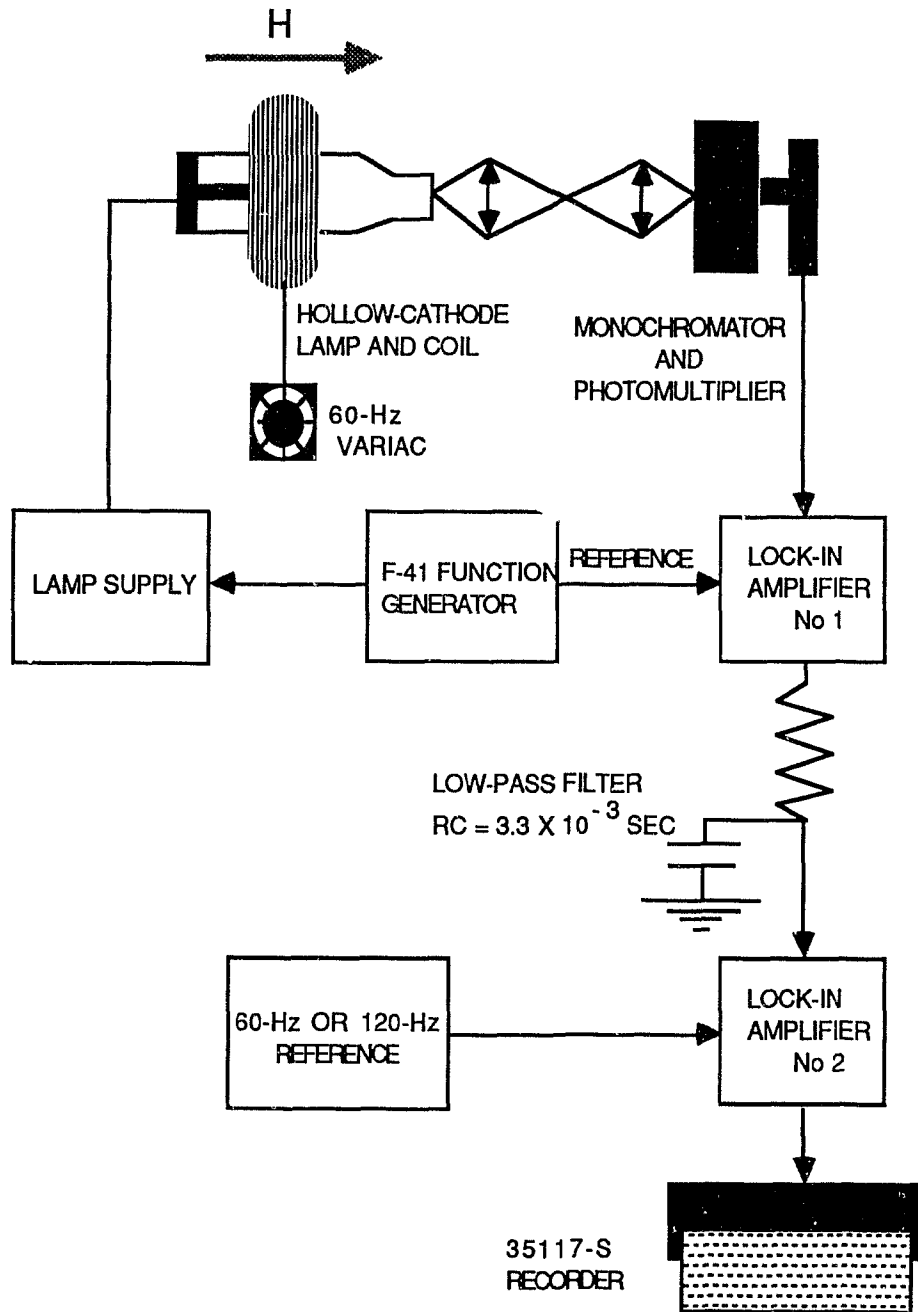
## 2.2 EXPERIMENTAL.

A diagram of the optical arrangement is shown in Figure 2.1. Hollow-cathode lamps, Na, Mg (Varian Techtron Pty Ltd., Australia), and Li (63060, Instrumentation Laboratory, Wilmington, MA), were the sources of radiation. The fact that the lamps were filled with neon also permitted measurement of the harmonics for neon lines.

The hollow-cathode lamp was surrounded by a magnetic field aligned parallel to the optical axis and produced by an air-cored water-cooled coil placed concentrically around the lamp. The coil (built in the laboratory) was made of 22 gauge magnet wire (B & S Wire Products Inc., Oakville, Connecticut) wound on a 40 mm I.D. pyrex tube and coated with epoxy resin. The water inlet and outlet were made of 8 mm O.D. pyrex. The power supply for the coil was a 60 Hz 146 Variac Powerstat (The Superior Electric Co., Bristol, CN). The coil could be displaced along the axis of the hollow-cathode lamp to change the field strength at the cathode.

The optical beam was focussed by two quartz biconvex lenses onto the entrance slit of an MP-1018A monochromator (McKee-Pedersen Instruments, Danville, CA). An MP-1021 photomultiplier tube (McKee-Pedersen Instruments, Danville CA) was used as detector.

**FIGURE 2.2** Signal processing block diagram for the measurement of the first and second harmonics in the field-on-source configuration.



The power supply of the hollow-cathode lamp was driven by a 1.3 kHz pulse train from a F-41 function generator (Interstate Electronics, Anchorage, CO) (Figure 2.2) which allowed high lamp currents to be attained. The electric signal from the photomultiplier/pre-amplifier was processed at the reference frequency of the hollow-cathode lamp by lock-in amplifier No 1. The first or second harmonic was determined by selecting the 60 Hz or 120 Hz reference to lock-in amplifier No 2. The harmonic signals were recorded in a 35117-SI Omniscrite recorder (Omniscrite, Austin, TX).

Prior to any measurement, the hollow-cathode lamp was warmed up for half an hour to allow the output intensity to stabilise. Mg and Na hollow-cathode lamps were chosen to measure the harmonics of the 377.7 nm Ne and 585.2 nm Ne lines respectively. The field strength at the cathode was varied by displacing the coil along the axis of the hollow-cathode lamp. The maximum field strength was 0.042 Tesla (see Appendix B), obtained at the centre of the coil. The amplitude of the selected harmonic was determined in a series of consecutive measurements at each selected position as the coil was displaced along the axis of the lamp. Each harmonic measurement was carried out by applying the magnetic field for up to 15 seconds, to avoid overheating of the coil. In order to correct for intensity changes when the field was applied, the gain of the photomultiplier tube was adjusted as the coil was displaced along the axis of the lamp. The phase between the signal and the reference was adjusted during the first measurement when

the centre of the coil was at the cathode. The phase adjustment for the first harmonic was monitored on an oscilloscope, and for the second harmonic by adjusting for maximum output from lock-in amplifier No 2.

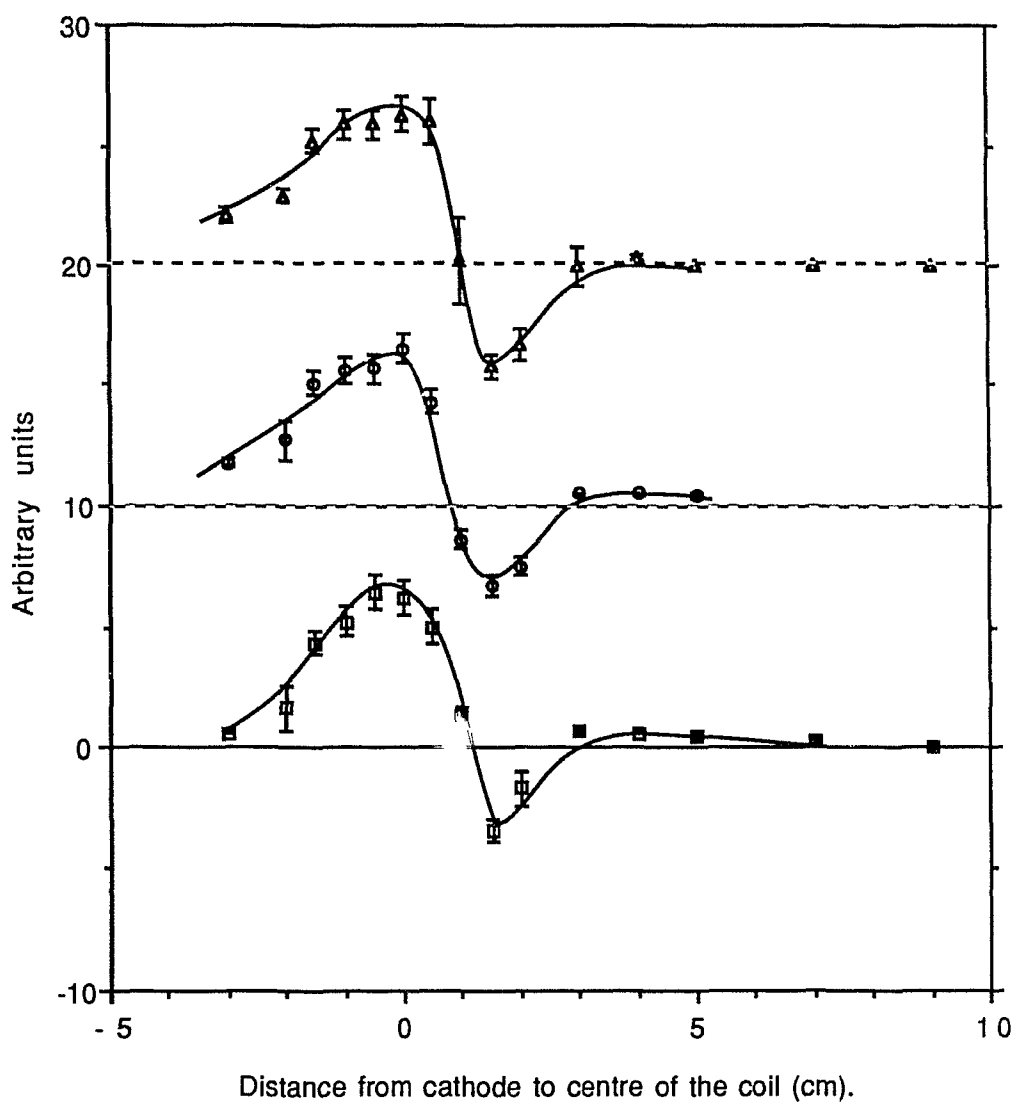
## **2.3 RESULTS AND DISCUSSION.**

### **2.3.1. Ne results**

The results for the 585.2 nm Ne(I) line are shown in Figure 2.3 and 2.4. This line corresponds to a transition between the ground state and a non-ionised electronic state [46]. The emission has to be located in the plasma, close to the cathode-anode region, while self-absorption is produced by the long path in front of the cathode filled with neon gas. As expected, when the lamp current is changed, the first and second harmonics of the 585.2 nm Ne(I) line show very similar behaviour at every field strength (position of the coil along the lamp axis), which indicates that self-absorption is largely independent of the lamp current. The first and second harmonics both show an inversion as the centre of the coil is displaced, and are of comparable magnitude.

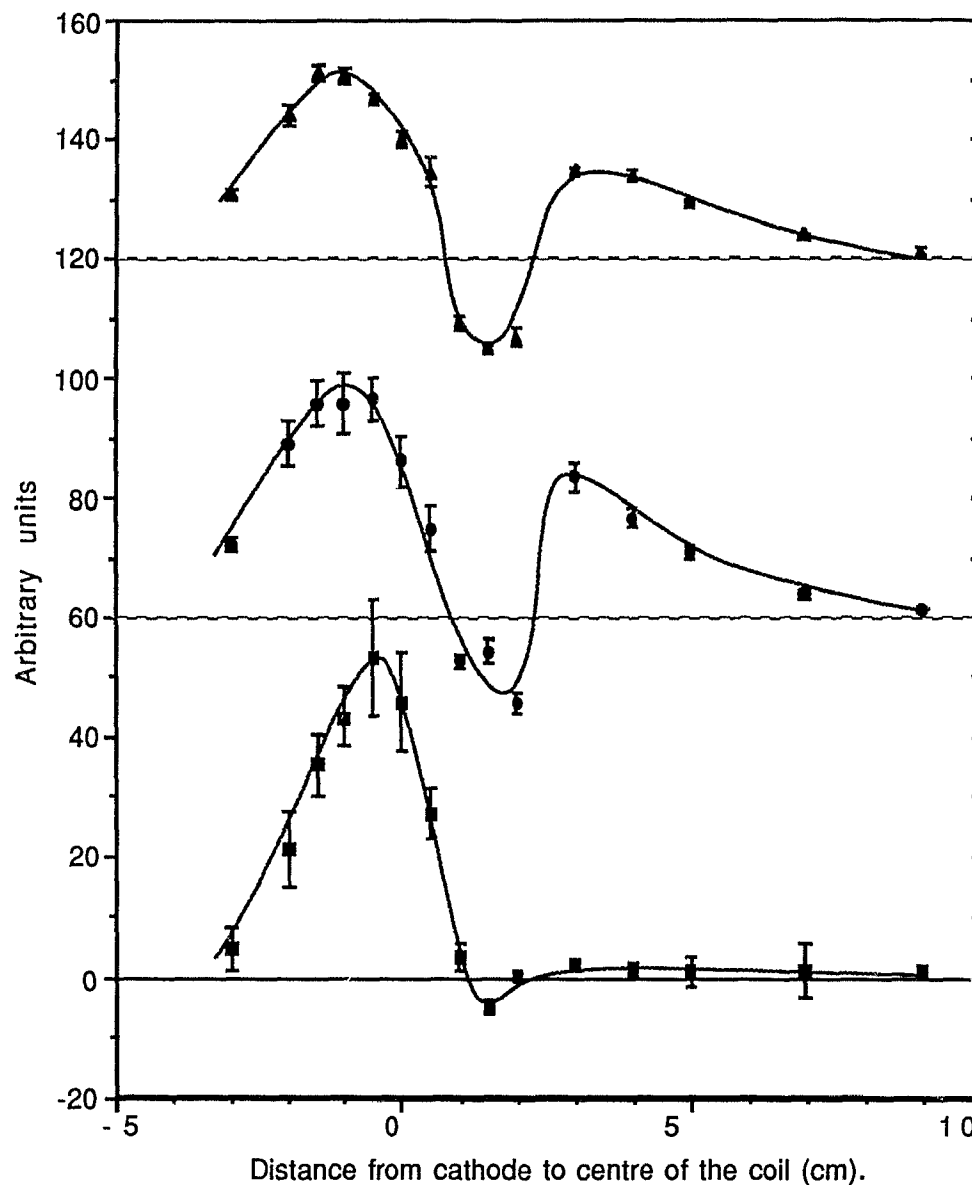
The results for the 377.7 nm Ne(II) line are shown in Figure 2.5. This line corresponds to a transition between two singly ionized electronic states [46]. The amplitude of the first harmonic is relatively small compared to the amplitude of the second harmonic at each of the lamp currents investigated. The high potential energy of the lower state above the ground state (27.2 eV) suggests a reduced population there which is not able to produce

**FIGURE 2.3** Second harmonic of the 585.2 nm neon(I) line versus coil position.



The second harmonic measurements at 24, 34, and 48 mA are represented by  $\square$ ,  $\circ$ , and  $\Delta$  respectively; they have an offset of 0, +10, and +20 arbitrary units respectively; error bars are the standard deviation of three measurements; the peak field strength at the centre of the coil was  $0.042 \pm 0.003$  Tesla.

**FIGURE 2.4** First harmonic of the 585.2 nm neon(I) line versus coil position.



The first harmonic measurements at 10, 17, and 27 mA are represented by  $\blacksquare$ ,  $\bullet$ , and  $\blacktriangle$  respectively; they have an offset of 0, +60, and +120 arbitrary units respectively; error bars are the standard deviation of three measurements; the peak field strength at the centre of the coil was  $0.042 \pm 0.003$  Tesla.

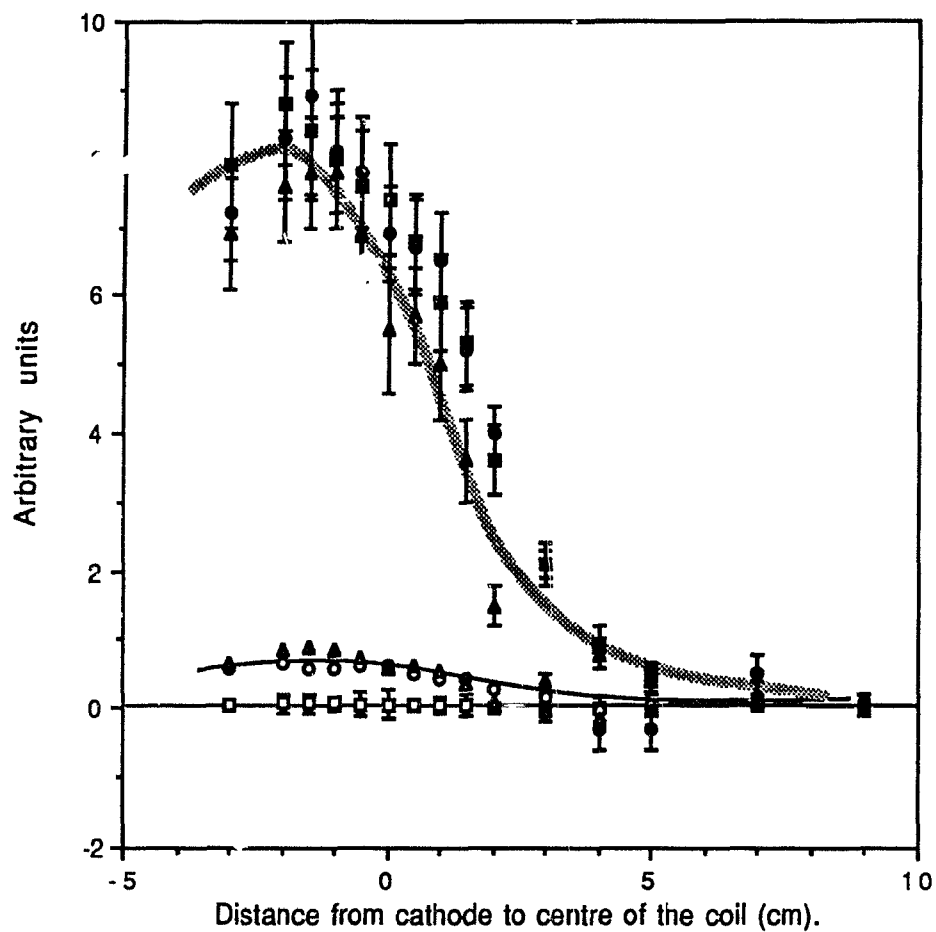
self-absorption. This fact explains the small amplitude of the first harmonic, because the existence of self-absorption is required in order to determine the first harmonic. Another consequence of the weak self-absorption is the lack of dependence of both harmonics on the lamp current since the transmitted profile is basically equal to the emission profile of the lamp, which is normalised at each lamp current.

The difference in the harmonic profiles of the 377.7 nm and the 585.2 nm Ne lines (Figures 2.3, 2.4, and 2.5, respectively) clearly indicates that harmonic analysis can detect the presence of self-absorption of, and is selective for, different electronic transitions.

### 2.3.2 Li and Mg results.

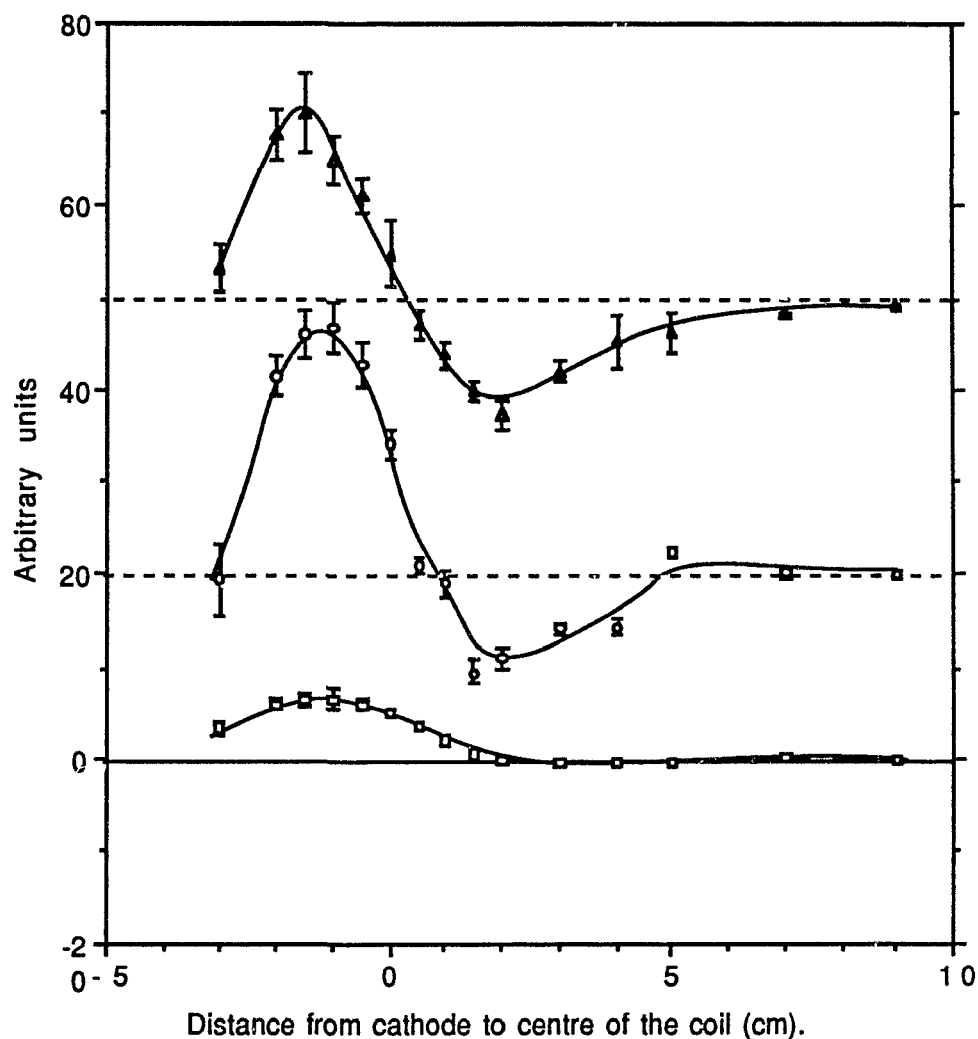
The harmonics of the 670.8 nm Li line (Figures 2.6 and 2.7) and 285.2 nm Mg line (Figures 2.8 and 2.9) show that the harmonic profiles of spectral lines of elements sputtered at the cathode are very susceptible to changes of the internal conditions within the lamp. The degree of self-absorption increases with increasing lamp current. The first and second harmonics are evidently sensitive to the degree of self-absorption and emission as indicated by their profiles at different lamp currents.

**FIGURE 2.5** First and second harmonics of the 377.7 nm neon (II) line versus coil position.



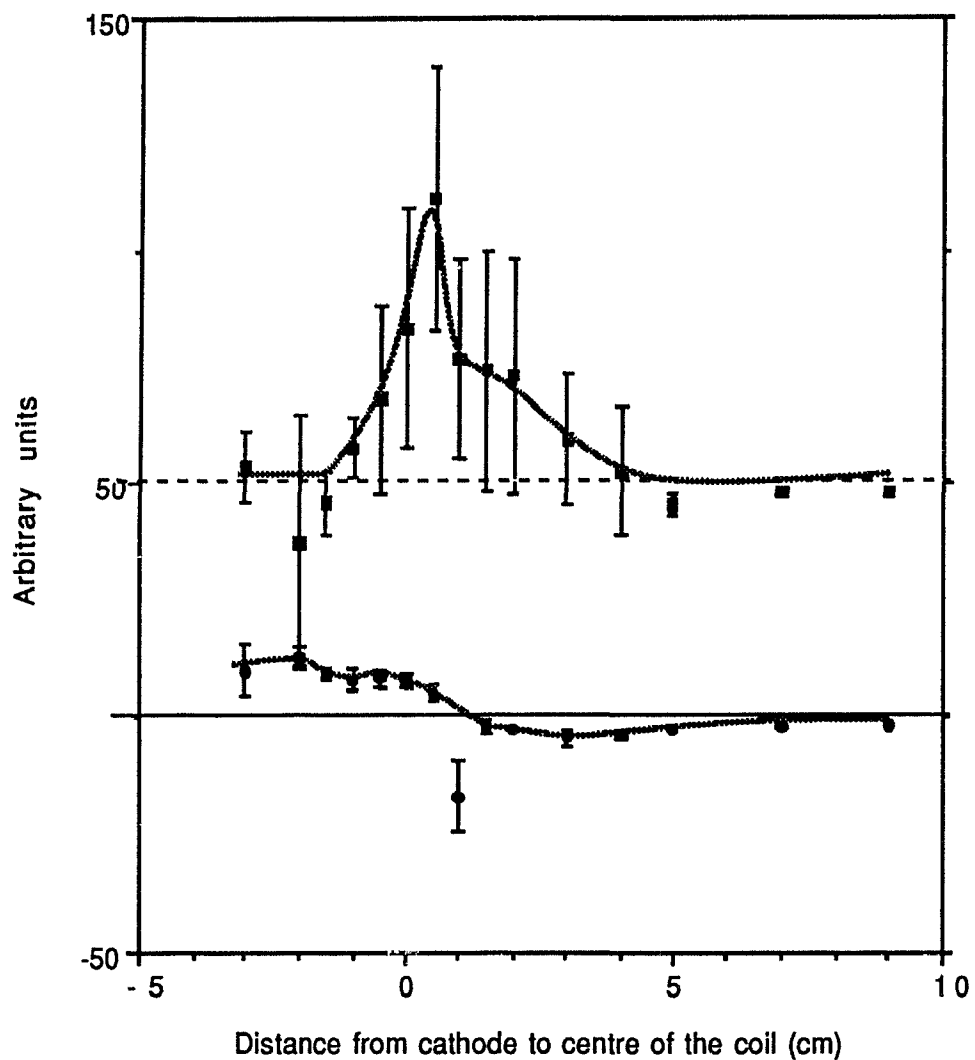
The first harmonic measurements at 17, 32, and 40 mA are represented by  $\square$ ,  $\circ$ , and  $\triangle$  respectively. The second harmonic measurements at 19, 29, and 48 mA are represented by  $\blacksquare$ ,  $\bullet$ , and  $\blacktriangle$  respectively; error bars are the standard deviation of three measurements; the peak field strength at the centre of the coil was  $0.042 \pm 0.003$  Tesla.

**FIGURE 2.6** Second harmonic of the 670.8 nm lithium line versus coil position.



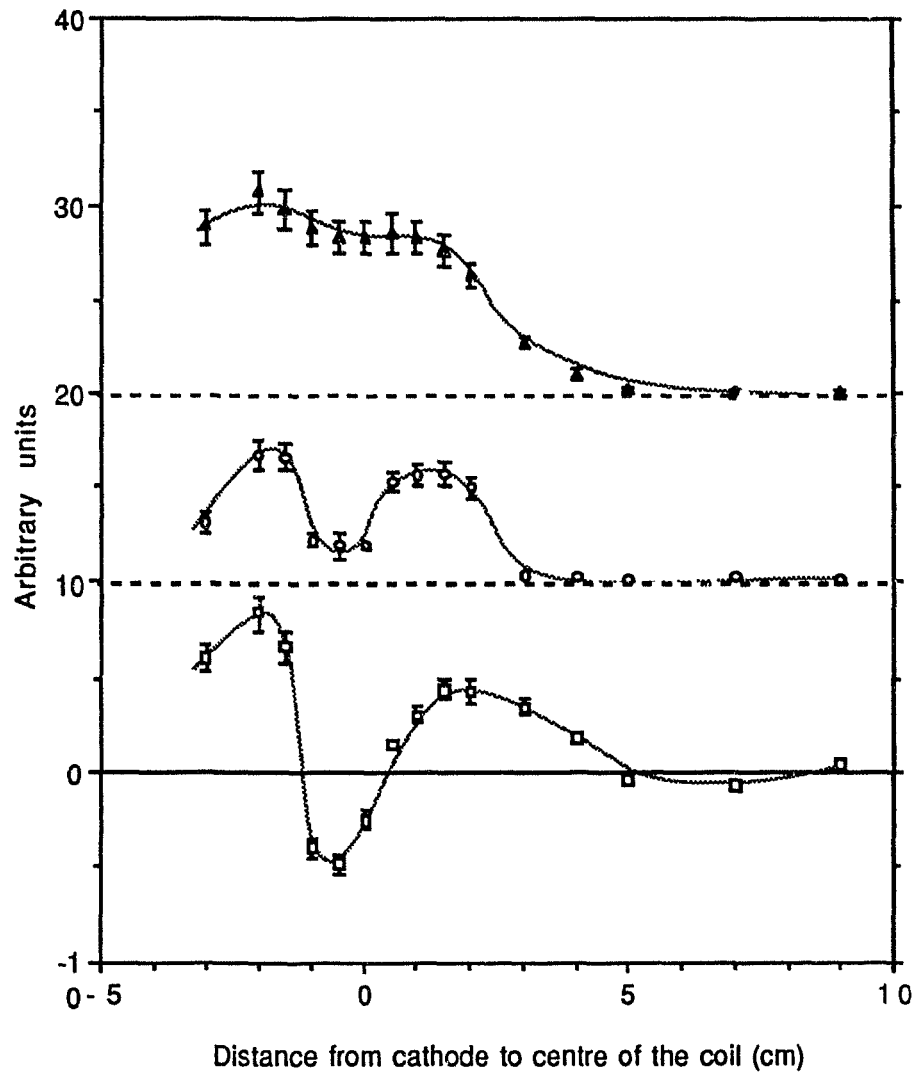
The second harmonic measurements at 24, 34, and 48 mA are represented by  $\square$ ,  $\circ$ , and  $\Delta$  respectively; they have an offset of 0, +20, and +50 arbitrary units respectively; error bars are the standard deviation of three measurements; the peak field strength at the centre of the coil was  $0.042 \pm 0.003$  Tesla.

**FIGURE 2.7** First harmonic of the 670.8 nm lithium line versus coil position.



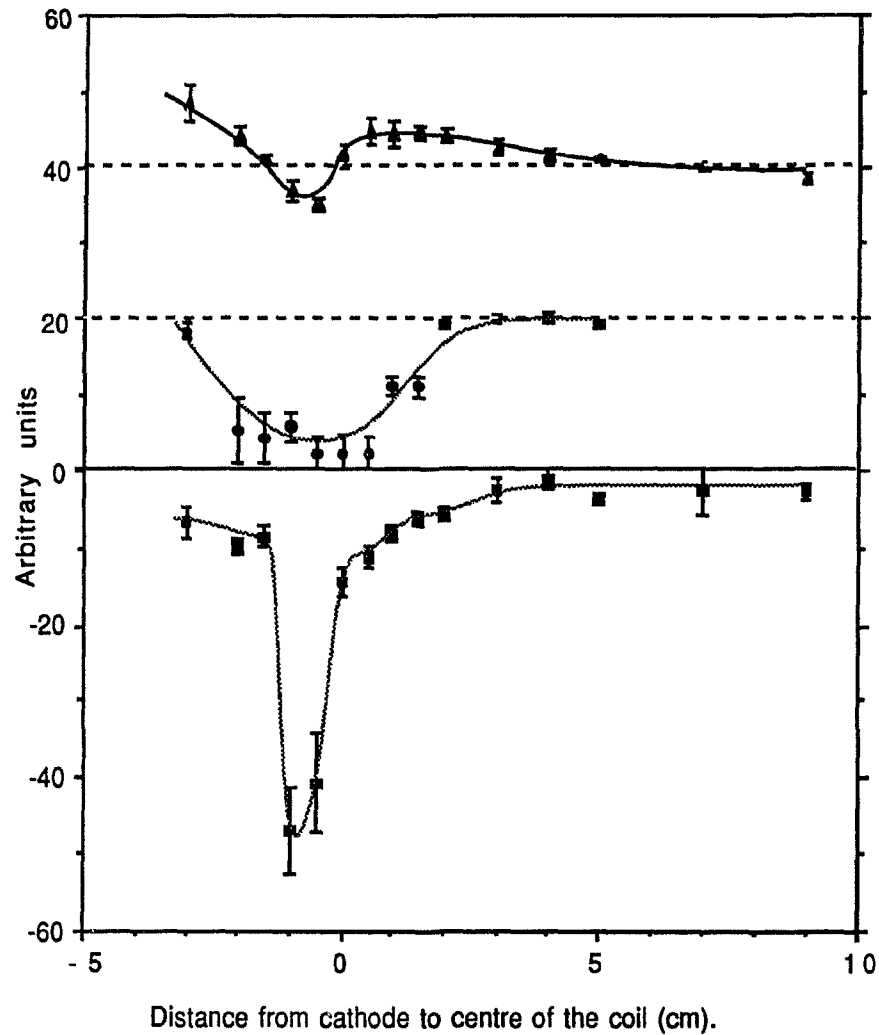
The first harmonic measurements at 36, and 51 mA are represented by ■ and ● respectively; they have an offset of 0, and +50, arbitrary units respectively; error bars are the standard deviation of three measurements; the peak field strength at the centre of the coil was  $0.042 \pm 0.003$  Tesla.

**FIGURE 2.8** Second harmonic of the 285.2 nm magnesium line versus coil position.



The second harmonic measurements at 19, 29, and 48 mA are represented by  $\square$ ,  $\circ$ , and  $\Delta$  respectively; they have an offset of 0, +10, and +20 arbitrary units respectively; error bars are the standard deviation of three measurements; the peak field strength at the centre of the coil was  $0.042 \pm 0.003$  Tesla.

**FIGURE 2.9** First harmonic of the 285.2 nm magnesium line versus coil position.



The first harmonic measurements at 10, 17, and 32 mA are represented by  $\blacksquare$ ,  $\bullet$ , and  $\blacktriangle$  respectively; they have an offset of +20, 0, and +40 arbitrary units respectively; error bars are the standard deviation of three measurements; the peak field strength at the centre of the coil was  $0.042 \pm 0.003$  Tesla.

Replicates of the measurements done at the same lamp current on several occasions were usually markedly different from each other. This fact suggests that the combined interactions between the plasma in the lamp and the external probe field are poorly controlled in the present apparatus. However it appears that a comparison of first and second harmonic amplitudes does contain selective experimental information on the nature of the atomic line profiles encountered in an atomic absorption measurement. A potentially more useful application of this observation is described in the next chapter.

### **3. DETECTION OF SPECTRAL INTERFERENCES BY HARMONIC ANALYSIS WITH A FIELD-ON-ATOMISER CONFIGURATION.**

#### **3.1 PURPOSE.**

The presence of spectral interferences is a potential weakness of the Zeeman background correction technique [14, 18, 20]. As mentioned in section 1.3, the effective performance of the Zeeman-corrected spectrometer requires that the background absorption in the wavelength region of interest be independent of the presence of a magnetic field. However, this may not be the case: extraneous absorption lines close to the line of interest, rotational molecular bands, and radicals can produce background absorption and may show Zeeman splitting. A lack of awareness of their presence may produce under or over correction by the spectrometer. In this chapter, a technique which indicates the presence of a spectral interference is described.

Zeeman scanning can reveal, in principle, differences in line profiles, centre frequency, and the nature of the Zeeman multiplet of different spectral lines; say the analyte line and the extraneous line. One way to obtain a Zeeman scan is by use of an alternating magnetic field (a.c. field) which generates a corresponding a.c. signal containing the information about the absorption line. The information can then be extracted by Fourier analysis. Furthermore, the proper selection of the results of the Fourier analysis can enormously simplify the calculations and measurements involved

without a significant loss of the encoded information. The selection of the three lowest harmonics provides enough information to characterise the presence or absence of interferences [47].

In order to understand the way in which Fourier analysis reveals information about the line of interest and the potential interference the following model, based on the normal Zeeman effect, is adopted. The profiles are described by Gaussian functions (Doppler broadening) and hyperfine structure is ignored. It is assumed that a magnetic field is applied to the atomiser perpendicularly to the optical axis (Voigt configuration). The absorption coefficients of the  $\pi$  and  $\sigma$  components  $K_{\pi}(\nu)$ ,  $K_{\sigma}(\nu)$  are dependent on the frequency  $\nu$ , the magnetic field strength  $H$ , the line centre frequency  $\nu_0$  ( $H = 0$ ), the width of the absorption profile  $\Delta\nu_a$ . They are represented as,

$$K_{\pi}(\nu) = \frac{K_0}{2} \exp \left[ -2 \sqrt{\ln 2} \frac{\nu - \nu_0}{\Delta\nu_a} \right]^2 \quad (31)$$

$$K_{\sigma}(\nu) = \frac{K_0}{2} \exp \left[ -2 \sqrt{\ln 2} \frac{\nu - \nu_0 \pm 1.4H}{\Delta\nu_a} \right]^2 \quad (32)$$

where  $K_0$  is the maximum absorption coefficient ( $H = 0$ ). The frequency shift of the Zeeman components caused by the magnetic field has been described in section 1.2.

The source profile  $I(\nu)$  is also described as a Gaussian profile. It is dependent on the frequency  $\nu$ , the source centre frequency  $\nu_s$ , and the width of the source profile  $\Delta\nu_s$ .

$$I(\nu) = I^0 \exp \left[ -2 \sqrt{\ln 2} \frac{\nu - \nu_s}{\Delta\nu_s} \right]^2 \quad (33)$$

where  $I^0$  is the peak intensity.

According to the model, a signal which measures the difference between the  $\pi$  and  $\sigma$  absorption, which is the response of the instrument used in this work, is obtained by combining equations (31-33) and integrating over the optical bandwidth  $w$  of the instrument:

$$S = \frac{I^0}{2} \int_w \exp \left[ -2 \sqrt{\ln 2} (\nu - \nu_s) / \Delta\nu_s \right]^2 \Delta K \, d\nu \quad (34)$$

where

$$\Delta K = \exp[-K_\pi(\nu)N\ell] - \exp[-K_\sigma(\nu)N\ell]$$

and  $N, \ell$  are the atom density and absorption pathlength respectively.

The field strength  $H$  can be expressed as  $H = H_{dc} + H_{ac} \sin \omega_H t$ , where the first term is the d.c. field and the second term is the a.c. field. Then the Fourier series of the equation (34) can be expressed as:

$$S = \frac{b(0)}{2} + \sum_{j=1}^{\infty} a(j) \sin(j\omega_H t) + b(j) \cos(j\omega_H t) \quad (35)$$

where

$$a(j) = \frac{1}{\pi} \int_w S \sin(j\omega_H t) dt \quad (36)$$

and

$$b(j) = \frac{1}{\pi} \int_w S \cos(j\omega_H t) dt \quad (37)$$

The integration is carried out over one cycle;  $S$  is given by the equation (34).

The harmonics  $b(0)/2$ ,  $a(1)$ ,  $b(2)$ , etc. are functions of the variables of equation (34). Thus they must vary when parameters such as  $N$ ,  $H$ ,  $\Delta v_s$ ,  $\Delta v_a$ ,  $v_s - v_o$  change. Particularly important is the dependence of the harmonics on the two latter parameters since they are characteristically different for the interfering line. Based on this simple model, identification of the presence or absence of interferences is possible [47]. Further discussion about this model is included in section 3.3.

Two cases of spectral interferences were evaluated: the overlap of the  ${}^6\text{Li}$  and  ${}^7\text{Li}$  isotopes at the 670.8 nm doublet and the

spectral overlap of the 271.904 nm Pt and 271.902 nm Fe lines. The two transitions of the lithium doublet,  $^2P_{3/2} \text{ --- } ^2S_{1/2}$  and  $^2P_{1/2} \text{ --- } ^2S_{1/2}$ , are separated by 0.015 nm, which is also equal to the isotopic shift between the individual lines of the  $^6\text{Li}$  and  $^7\text{Li}$  doublets. As a result, the doublet of each isotope is only partially resolved [26].

### 3.2 EXPERIMENTAL.

#### 3.2.1 Harmonic measurements.

A block diagram of the instrument used to measure the d.c. signal  $b(0)/2$ , the first harmonic  $a(1)$ , and the second harmonic  $b(2)$  is shown in Figure 3.1. The model described in section 3.1 predicted that other terms of the series are comparatively small with respect to these three terms [47].

The sources of radiation were modulated hollow-cathode lamps; a natural Li lamp (Instrumentation Laboratory, Wilmington, MA) was used for the detection of natural Li (referred to as  $^7\text{Li}$  hereafter) and  $^6\text{Li}$  and a Pt lamp (Cathodeon Ltd, Cambridge, England) for the detection of Fe and Pt. Amplitude modulation of the lamps was necessary to correct for emission from the atomiser.

Atomisation was achieved by means of an air-acetylene flame (air flow: 2500 ml/min air at S.T.P.; acetylene flow: 540 ml/min air at S.T.P.) surrounded by a water-cooled magnet (Hammond Transformer Co., Guelph, Ontario). A diagram of the burner and nebuliser can be seen in Figure 3.2. The nebulisation was produced

by a modified Babington nebuliser in order to decrease sample consumption. The solutions were injected by means of a syringe. The Li solutions were prepared from LiCl (Fisher Scientific Co., Fair Lawn, NJ) and  $^6\text{LiOH}$  (Stöhler Isotope Chemicals, Montreal), respectively. The Fe and Pt solutions were prepared from  $\text{FeCl}_3 \cdot 6\text{H}_2\text{O}$  (Nichols Chemicals Co. Ltd., Montreal) and  $\text{H}_2\text{PtCl}_6 \cdot 6\text{H}_2\text{O}$  (EM Science, NJ), respectively.

The magnet was oriented to keep the field perpendicular to the optical axis (Voigt configuration). The direction of the field also defined the x axis. The magnet was driven by a laboratory-built power supply (Figure 3.3) that provided independent drive for the a.c. and d.c. fields. The a.c. field used was set at its maximum, 0.10 Tesla peak, while the d.c. field (range: 0-0.7 Tesla) was adjusted to optimise discrimination.

A PEM-80 photoelastic modulator (Hinds International Inc., Portland, Oregon) with its main axis rotated by  $45^\circ$  from the x axis modulated the signal at 100 kHz, permitting reduction of flicker noise and allowing the photon noise limit to be reached.

A polaroid sheet or a calcite prism (Melles-Griot, Irvine, CA) blocked the  $\pi$ -polarised radiation. The polaroid sheet was used to study the spectral interference of the lithium isotopes at the 670.8 nm doublet, while the calcite prism was used to study the spectral interference of the Pt/Fe system at 271.9 nm.

FIGURE 3.1 Block diagram of the instrument used to measure  $b(0)$ ,  $a(1)$ , and  $b(2)$ .

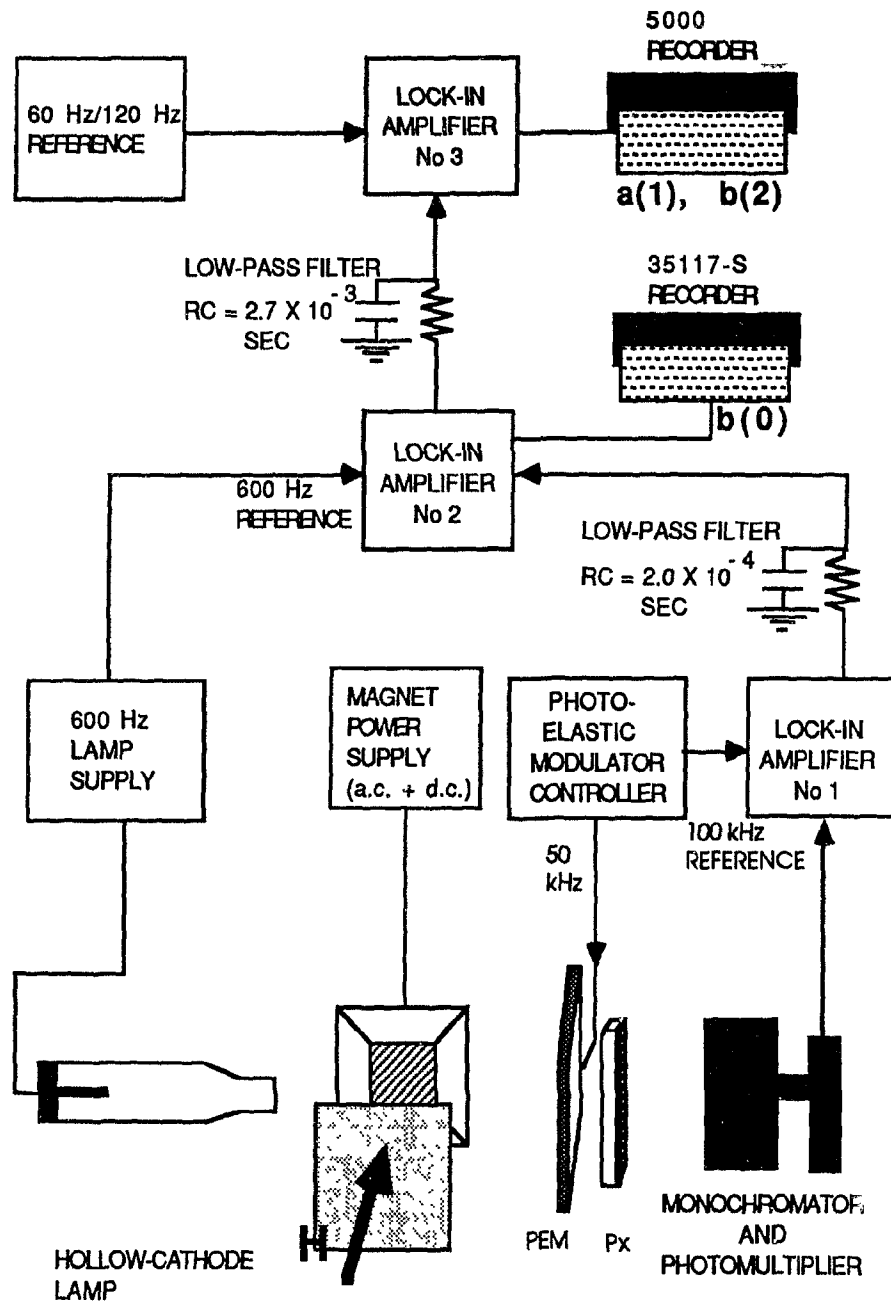


**FIGURE 3.2** Diagram of the burner and the nebuliser.

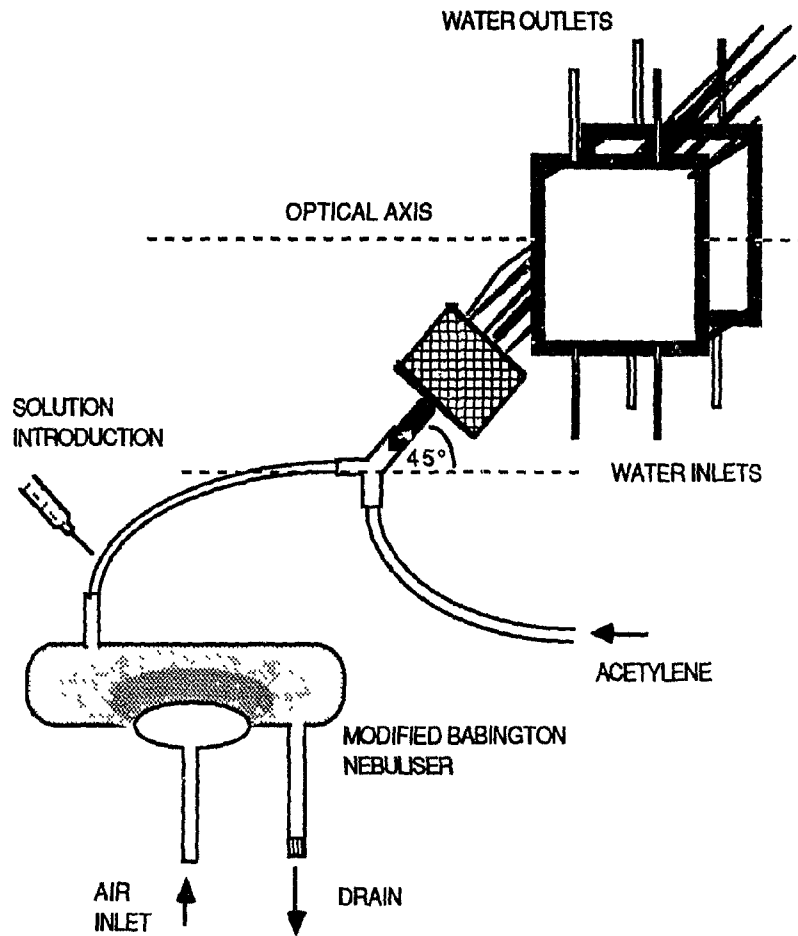
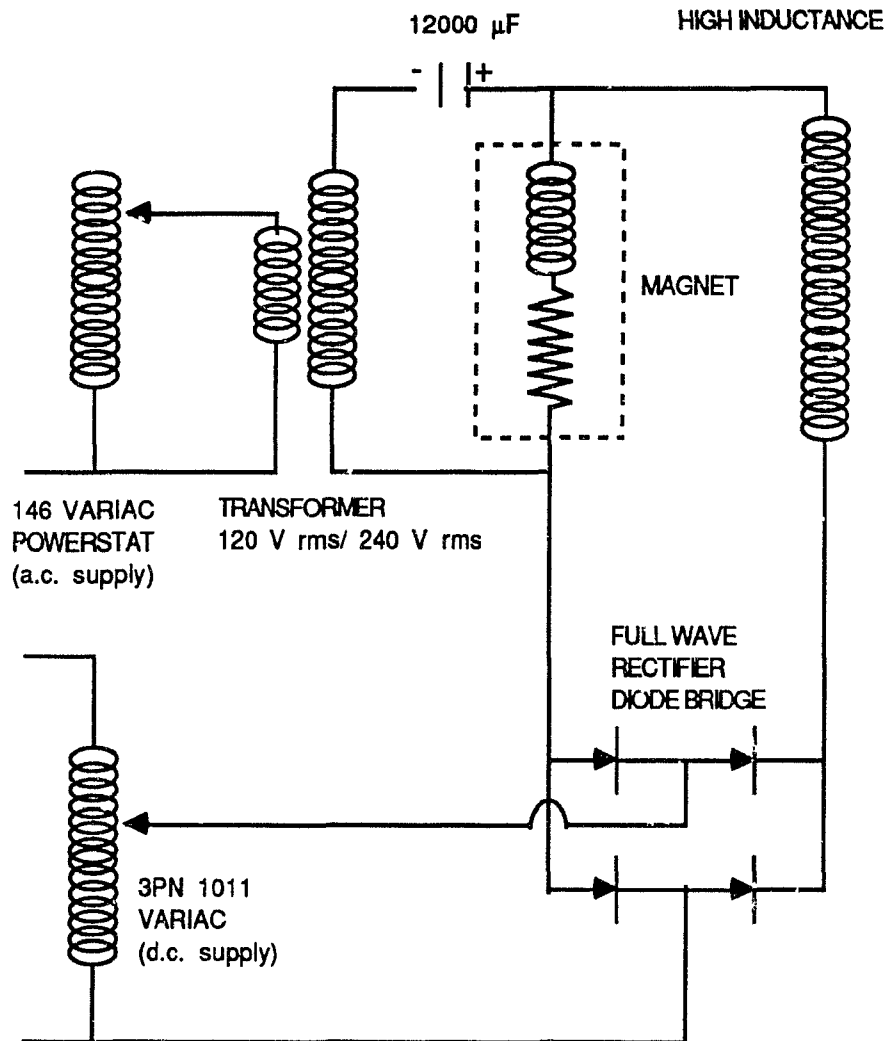


**FIGURE 3.3** Circuit diagram of the magnetic field supply.



Maximum d.c. output: 50 V (Variac setting: 50%);  
 Maximum a.c. output: 240 V rms (Variac setting: 100%)

The line of interest was isolated and detected by an MP-10118A monochromator (McKee-Pedersen Instruments, Danville, CA) and a IP-28 RCA photomultiplier connected to a 100 kHz tuned pre-amplifier.

The response of the optical system can be found by application of the Jones Calculus (see Appendix A). The observed intensity at the detector is

$$I = \frac{1}{4} \int_0^{\infty} I(\nu) \{ \exp(-K_{\pi}(\nu)NL) - \exp(-K_{\sigma}(\nu)NL) + \cos 2\delta [\exp(-K_{\pi}(\nu)NL) - \exp(-K_{\sigma}(\nu)NL)] \} d\nu \quad (38)$$

where  $\delta = \delta^0 \sin \omega_p t$  is the retardance of the photoelastic modulator ( $\omega_p = 2\pi \cdot 50$  kHz). The other variables have the same meaning as in equations (31-33). Based on equation (38), the output of lock-in amplifier No 1 (Reference:  $2\omega_p = 2\pi \cdot 100$  kHz) can be predicted to be:

$$S = \text{constant} \int_0^{\infty} I(\nu) \{ \exp(-K_{\pi}(\nu)NL) - \exp(-K_{\sigma}(\nu)NL) \} d\nu \quad (39)$$

The constant term  $b(0)$  was recorded by a 35117-SI Omniscrite recorder (Omniscrite, Austin, TX) as the d.c. output of lock-in amplifier No 2 (Figure 3.1). The first and second harmonics  $a(1)$  and  $b(2)$  were recorded by a model 5000 Fisher recorder (B&L, Austin, TX) as the d.c. output of lock-in amplifier No 3 (Figure 3.1).

The first harmonic was measured by using the 60 Hz reference, the second harmonic by using the 120 Hz reference.

Prior to any measurement, the hollow-cathode lamp was warmed up for half an hour to allow the output intensity to stabilise. Wavelength setting, wavelength retardance of the photoelastic modulator, phase shift of the 100 kHz signal (lock-in amplifier No 1), and optical alignment were optimised by producing a dichroic signal with a quartz plate. The phase shifts of the 60 and 120 Hz signals were pre-selected by optimising the signals of either 500 ppm Li or 10,000 ppm Pt solutions and applying an a.c. field of 0.10 Tesla peak. The authenticity of the measurements was corroborated by aspirating distilled water and noticing the absence of the  $b(0)$ ,  $a(1)$ , and  $b(2)$  signals. This verification was done with an a.c. field only (0.1 Tesla peak) and with an a.c. plus d.c. field (0.1 Tesla peak + 0.7 Tesla d.c.).

In general, the first and second harmonics  $a(1)$  and  $b(2)$  at each concentration were measured consecutively at intervals of less than one minute. The nebuliser was rinsed with distilled water between solutions, and enough time was allowed so that no signal was noted in the presence of a magnetic field, as described above. In addition, all the solutions of the same type were analysed consecutively in order to decrease the risk of contamination.

### 3.2.2 Selection of the d.c. field.

Figure 3.4 shows a block diagram of the system used to determine the d.c. field that provided the best discrimination for the harmonic signals of the interfering lines. The equipment was the same as for the harmonic measurements except for the photomultiplier tube. An MP-1021 photomultiplier tube (McKee-Pedersen Instruments, Danville, CA) was used in this case and the pre-amplifier was not tuned to 100 kHz. Only the d.c. magnetic field was applied in this case.

Application of Jones calculus (see Appendix A) to the optical train (Figure 3.1) leads to:

$$S_{H \neq 0} = \text{constant} \int_w \frac{I(\nu)}{2} \exp[-K_{\sigma}(\nu)N\ell] d\nu \quad (40)$$

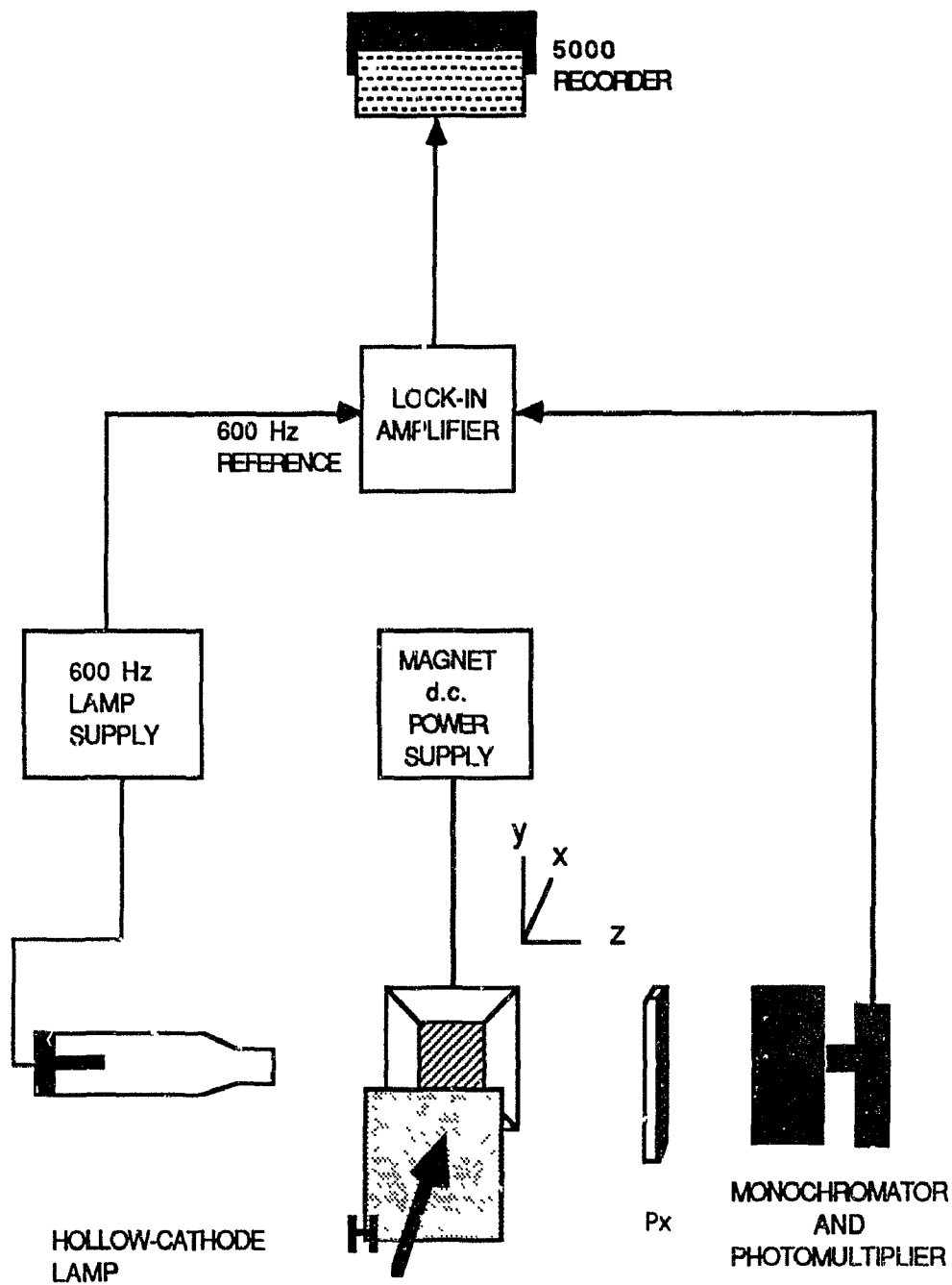
when  $H \neq 0$ .  $K_{\sigma}(\nu)$ , and  $I(\nu)$  are described by equations (32-33) and  $N, \ell$  have the same meaning as before.

If the d.c. field is not applied ( $H=0$ ), the response of the system is:

$$S_{H=0} = \text{constant} \int_w \frac{I(\nu)}{2} \exp[-K_{\pi}(\nu)N\ell] d\nu \quad (41)$$

where  $K_{\pi}(\nu)$  is described by equation (31).

**FIGURE 3.4** Block diagram of the optical arrangement used in Zeeman scanning.



A d.c. field ( $H \neq 0$ ) that provided  $S_{H \neq 0} = S_{H=0}$  for one of the lines of interest was found to show the best discrimination in the harmonic measurements.

### 3.3 RESULTS AND DISCUSSION.

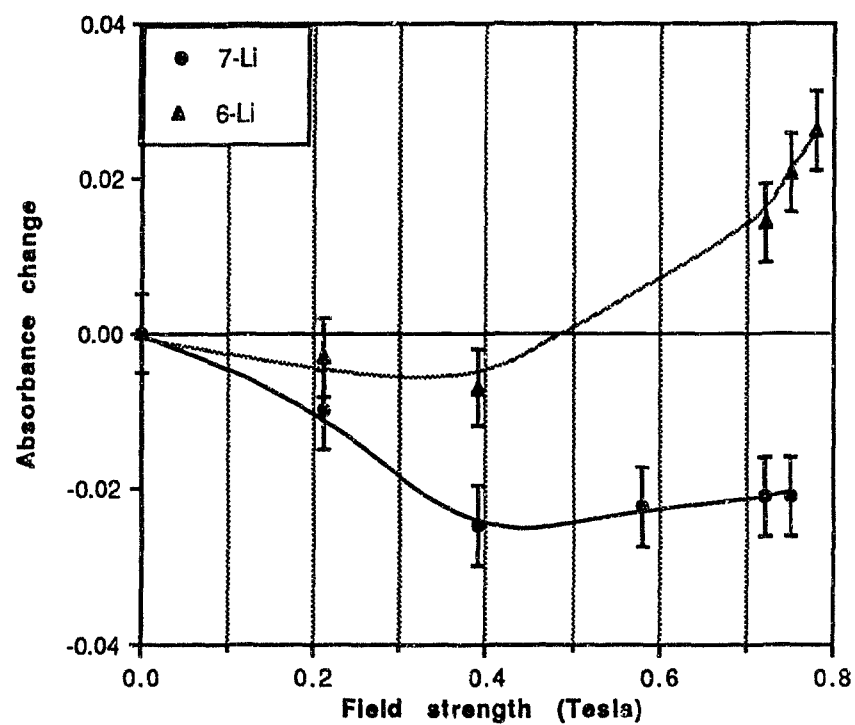
#### 3.3.1 Li isotopes.

For the two Li isotopes the 1% absorption sensitivity and the detection limit (signal-to-noise ratio equal to 2) on  $b(0)$  were 11 and 2 ppm, respectively, while in a conventional flame atomic absorption spectrometer they are 0.03 and 0.0006 ppm respectively [4].

The selection of the d.c. field was based on the results shown in Figure 3.5. The use of a 200 ppm  $^7\text{Li}$  or  $^6\text{Li}$  solution showed a selective response as the field strength was varied. The absorbance of  $^6\text{Li}$  below 0.49 Tesla was smaller than, at 0.49 Tesla was equal to, and above 0.49 Tesla was greater than the absorbance at zero field strength. On the other hand, the absorbance of  $^7\text{Li}$  was always less than the absorbance at zero field strength. The selection of 0.49 Tesla d.c. allowed good discrimination between measurement of the harmonics of the two isotopes.

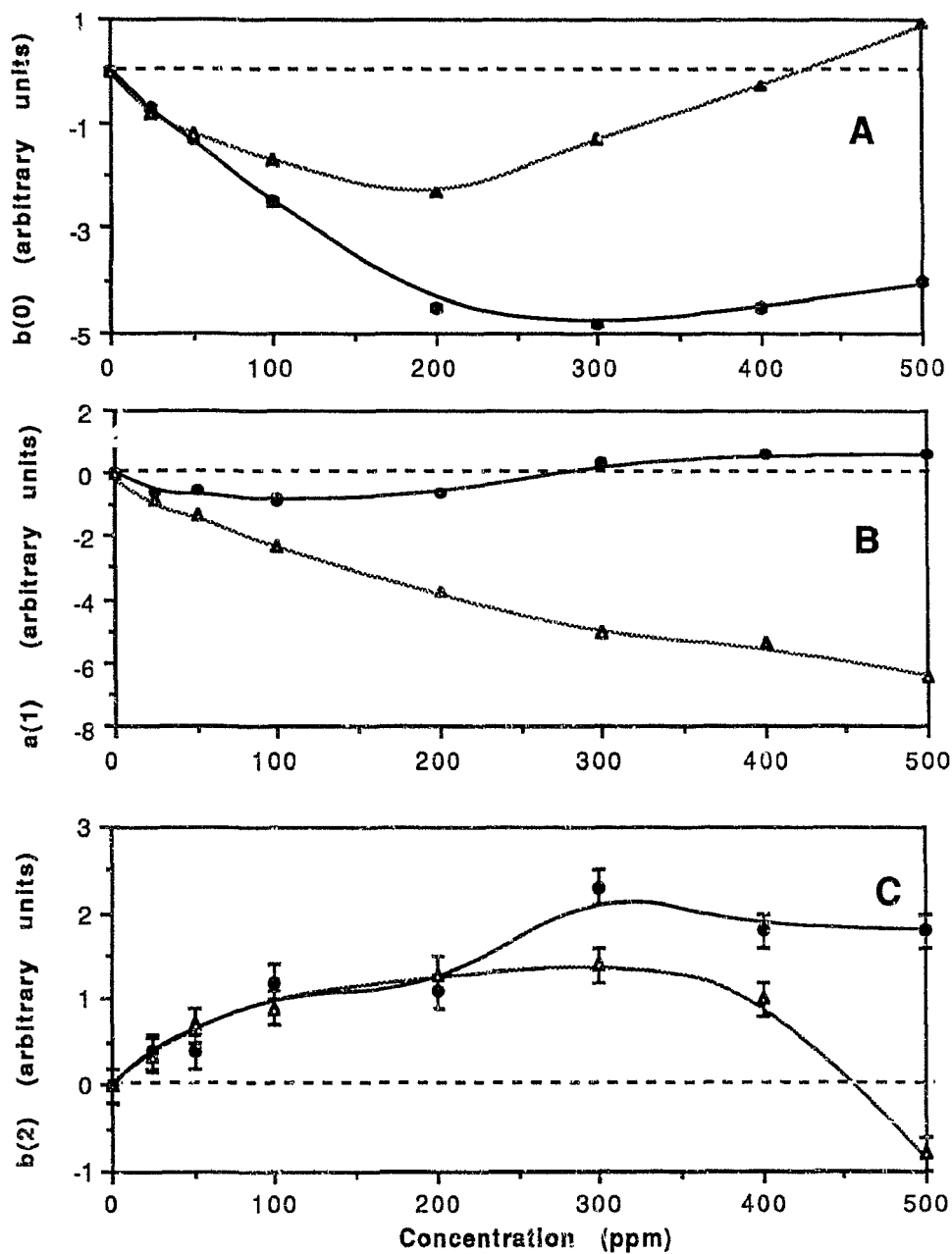
The harmonics of  $^7\text{Li}$  and  $^6\text{Li}$  at different concentrations are shown in Figures 3.6. Both  $b(0)$  and  $a(1)$  are sensitive to isotopic composition at concentrations above 50 ppm while  $b(2)$  requires

**FIGURE 3.5** Dependence of the change in the absorbance of the lithium isotopes versus field strength.



The absorbance of 200 ppm Li solution at zero field strength was 0.086 for both isotopes. Atomiser: air-acetylene flame. Source: natural Li hollow-cathode lamp; 670.8 nm; 20 mA pp; 600 Hz.

FIGURE 3.6 Harmonics of lithium isotopes.



${}^6\text{Li}$  and  ${}^7\text{Li}$  are identified by  $\Delta$ ,  $\bullet$  respectively. A, B, and C show the d.c. term  $b(0)$ , the first harmonic  $a(1)$ , and the second harmonic  $b(2)$  respectively. Atomiser: Air-acetylene flame in a 0.49 Tesla d.c. + 0.10 Tesla peak a.c. field. Source: natural Li hollow-cathode lamp; 670.8 nm; 20 mA; 600 Hz.

concentrations above 300 ppm. The amplitudes of the three harmonics are concentration dependent, as they should be [47].

In addition, different ratios of the harmonics of  ${}^7\text{Li}$  and  ${}^6\text{Li}$  were compared. The ratios  $a(1)/b(0)$ ,  $b(2)/b(0)$ , and  $a(1)/b(2)$  are shown in Figure 3.7. In general they showed less concentration dependence. The ratios  $a(1)/b(0)$  and  $a(1)/b(2)$  were selective for the two Li isotopes at concentrations above 50 ppm, while  $b(2)/b(0)$  was selective above 100 ppm. An additional feature which allows selective identification of the Li isotopes using the ratios of the harmonics is the zero crossing of the  $b(0)$  curve of  ${}^7\text{Li}$  at about 425 ppm, which produces a discontinuity in the  $a(1)/b(0)$  and  $b(2)/b(0)$  curves. This feature may be applied to characterise the absence of  ${}^6\text{Li}$ .

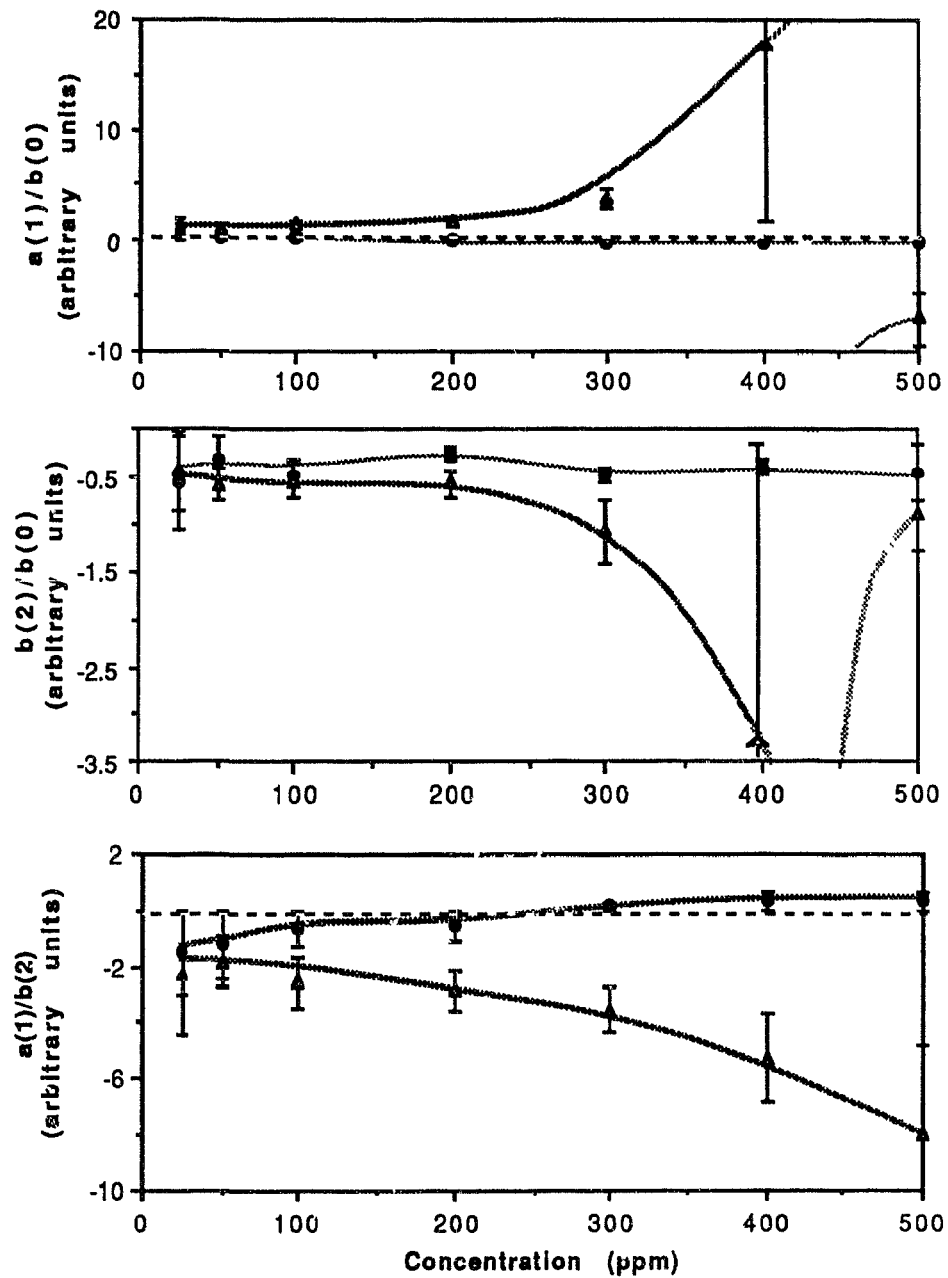
It can be concluded that, subject to the limitations mentioned above, the measurement of the the harmonics and/or their ratios allows selective determination of  ${}^7\text{Li}$  or  ${}^6\text{Li}$ . Other comments which also apply to the Pt/Fe system are given below.

### 3.3.2 Platinum-Iron.

The 1% absorption sensitivity of Pt and Fe on  $b(0)$  were 220 and 910 ppm respectively at 271.9 nm; the detection limit (signal-to-noise ratio equal to 2) on  $b(0)$  were 44 and 180 ppm, respectively.

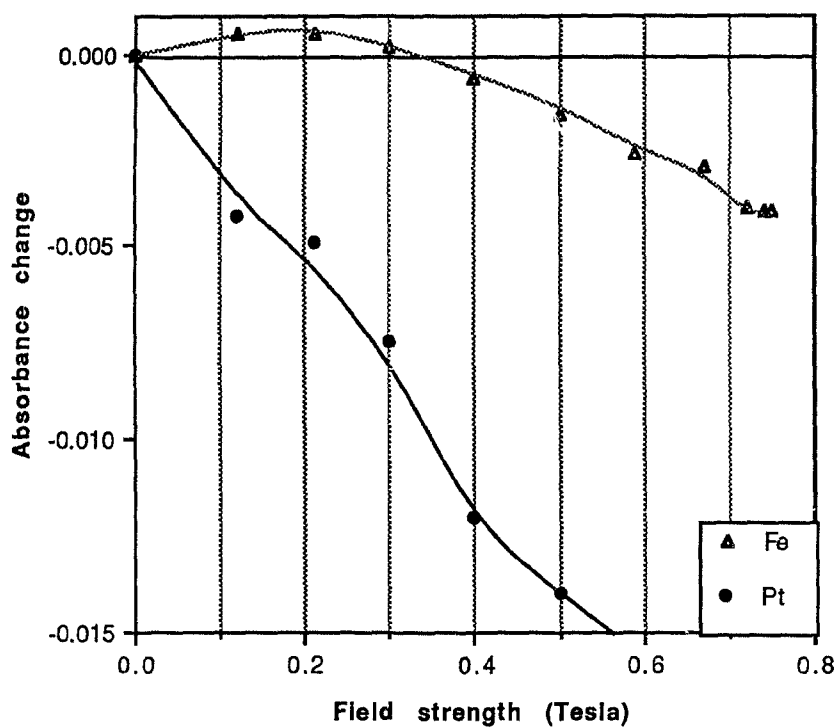
Selection of the d.c. field was based on the results shown in Figure 3.8. The use of 4700 ppm Pt or 10000 ppm Fe solutions

**FIGURE 3.7 Ratios of the harmonics of the lithium isotopes.**



${}^6\text{Li}$  and  ${}^7\text{Li}$  are identified by  $\Delta$ ,  $\bullet$ , respectively. Atomiser:  
 Air-acetylene flame in a 0.49 Tesla d.c. + 0.10 Tesla peak a.c. field.  
 Source: natural Li hollow-cathode lamp; 670.8 nm; 20 mA; 600 Hz.

FIGURE 3.8 Dependence of the change in the absorbance of Pt and Fe versus field strength.



The absorbances at zero field strength were 0.102 and 0.051 for 4700 ppm Pt and 10000 ppm Fe solutions respectively.

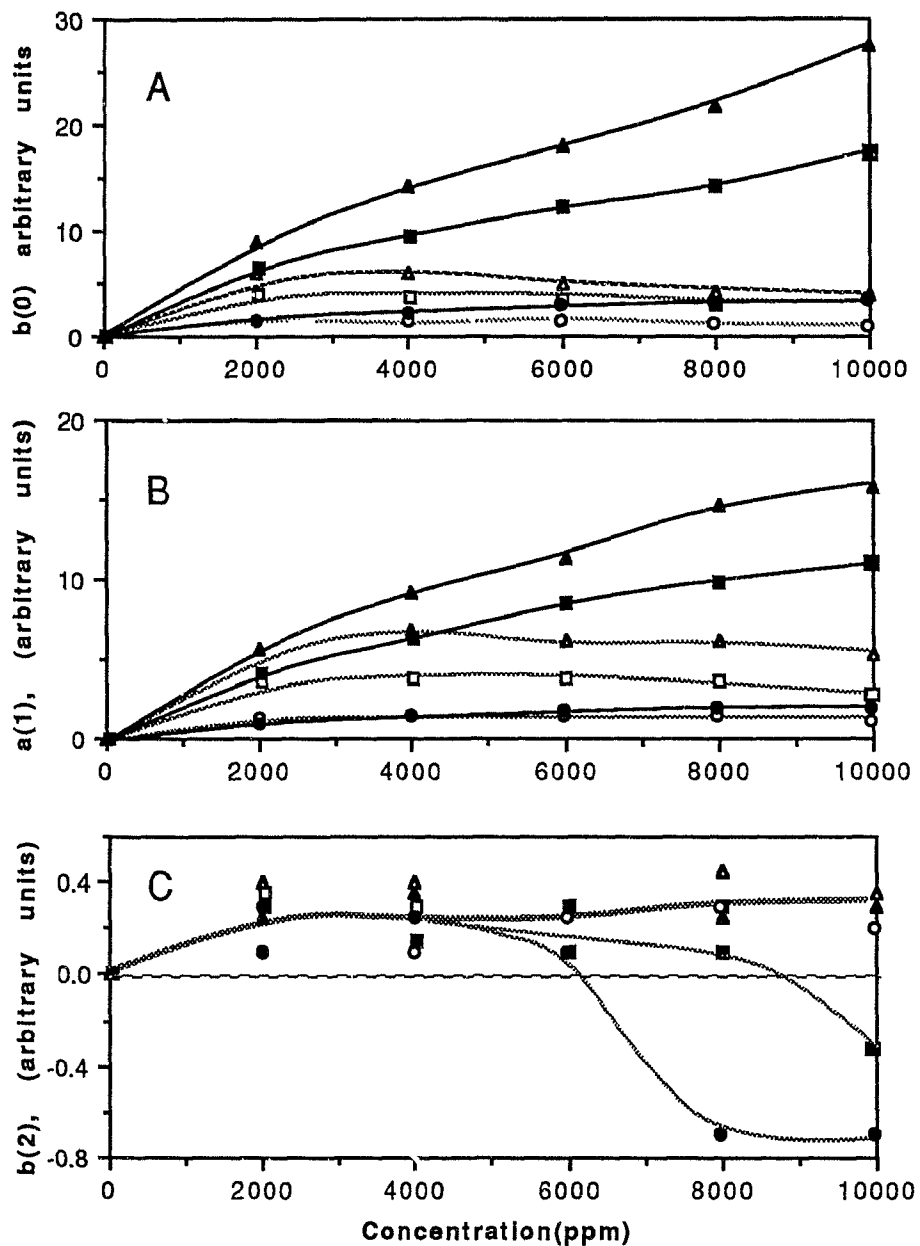
Atomiser: air-acetylene flame. Source: Pt hollow-cathode lamp; 271.9 nm; 12 mA pp; 600 Hz.

showed a selective response as the field strength was varied. Different concentrations of Pt and Fe were used, due to the different sensitivity of each element. The absorbance of iron was greater than the absorbance at zero field strength at fields below 0.34 Tesla, and smaller above that field. On the other hand, the absorbance of Pt decreased as the field strength increased. Based on this behaviour, the selection of 0.34 Tesla showed the most selective response in the measurements of the harmonics of Pt and Fe.

The harmonics of Pt and Fe at different cathode lamp currents and concentrations are shown in Figures 3.9. It is clearly seen that the harmonics of Fe and Pt are affected by the selected lamp current, although the harmonics of iron are less sensitive. The first harmonic  $a(1)$  and the d.c. term  $b(0)$  show better selectivity between Fe and Pt at low lamp currents, becoming practically indistinguishable as the current is increased to 20 mA. The trend of the second harmonic  $b(2)$  is apparently the opposite; but although it seems to show better discrimination at high currents, the poor signal-to-noise ratio of this harmonic hides such a behaviour.

Since the lamp current influences the width of the source profile, and harmonic amplitudes are affected by the lamp current, it can be said that the harmonic amplitudes are affected by the width of the source profile. The model based on the normal Zeeman effect predicted this behaviour qualitatively [47].

FIGURE 3.9 Harmonics of Pt and Fe.



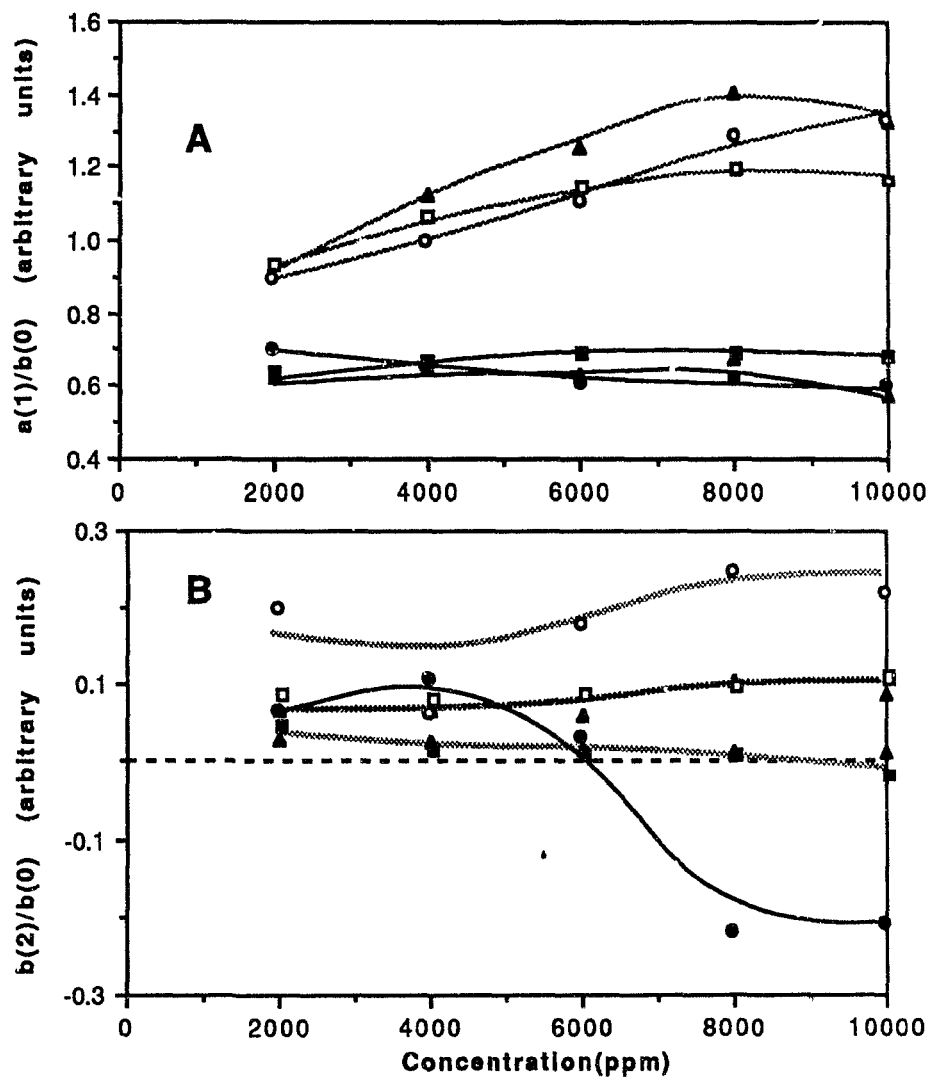
Fe measurements at 12, 16, and 20 mA are denoted by  $\blacktriangle$   $\blacksquare$   $\bullet$  respectively; Pt measurements at the same currents are denoted by  $\blacktriangle$   $\blacksquare$   $\bullet$  respectively. A, B, and C show the d.c. term  $b(0)$ , the first  $a(1)$ , and the second  $b(2)$  harmonics respectively; typical errors are 0.1, 0.1, and 0.2 arbitrary units respectively. Atomiser: Air-acetylene flame in a 0.34 Tesla d.c.+ 0.10 Tesla peak a.c. field. Source: Pt hollow-cathode lamp; 271.9 nm; 600 Hz.

The ratios  $a(1)/b(0)$  and  $b(2)/b(0)$  are shown in Figure 3.10. Based on the results of Figure 3.9 the ratio  $a(1)/b(0)$  was expected to show better selectivity at low currents. However Figure 3.10 A shows that the selectivity between Fe and Pt is essentially independent of the lamp current chosen, as opposed to  $b(2)/b(0)$  (Figure 3.10 B). The  $a(1)/b(2)$  ratio was not selective for the Fe and Pt measurements, and the results are not reported here. The poor signal-to-noise ratio of  $b(2)$  complicates comparison of the ratios of the harmonics including  $b(2)$ . Based on the model,  $b(2)/b(0)$  and  $a(1)/b(2)$  are potentially selective, but a better signal-to-noise ratio is required in their experimental determination to make them more attractive. The ratio  $a(1)/b(0)$  gives a useful response.

The experimental results of Pt and Fe can be predicted qualitatively by the model described in section 3.1. It has been observed that calculations including an anomalous multiplet improve the model further [47].

The two cases presented in this work, Li isotopes and Pt/Fe, clearly confirm the use of harmonic measurements to distinguish spectral interferences. On the basis of this work it appears to be feasible to use the technique to flag a warning if the amplitudes of the ratios of the harmonics are detected outside an expected range of a known analyte, and at that point to warn an operator of the presence of an uncorrected interference.

FIGURE 3.10 Ratios of the harmonics of Pt and Fe.



Fe measurements at 12, 16, and 20 mA are denoted by ▲ □ ○ respectively; Pt measurements at the same currents are denoted by ▲ ■ ● respectively. Atomiser: Air-acetylene flame in a 0.34 Tesla d.c. + 0.10 Tesla peak a.c. field. Source: Pt hollow-cathode lamp; 217.9 nm; 600 Hz.

The technique has the disadvantage that the harmonic ratios are dependent on concentration, which introduces the need for calibration curves.

In addition, the technique might allow simultaneous quantification of species showing spectral interferences, since calibration curves could presumably be prepared. An implied application would be the analysis of mixtures of isotopes using one source of radiation instead of isotopically enriched sources.

## **4. ZEEMAN-BACKGROUND CORRECTION IN PULSED DISCHARGE CELLS AT ATMOSPHERIC PRESSURE.**

### **4.1 PURPOSE.**

Sputtering has been applied successfully to produce atomic vapours [30-32]. This technique offers the advantage that it is largely independent of temperature, as opposed to flame atomisation or thermal vaporisation [30]. One disadvantage of the discharge cells is that they are usually operated at low pressures. Recently, Stephens introduced a helium discharge cell that operates at slightly above the atmospheric pressure [32].

Other problems found in discharge cells are background absorption, concomitant emission of radiation in the visible and ultraviolet region of the spectrum with production of atomic vapour [30, 31]. Although source modulation allows the separation of the radiation from the source and the emission of the discharge, the signal-to-noise ratio is reduced due to random noise. One approach to eliminating this problem includes using a discharge, which is periodically switched on and off, and an associated delayed measurement while the discharge is off. The main assumption here is that the emission from the sputtered atom and filler gas disappears faster than the atom population at the lower state of the electronic transition [31]. No correction for background absorption is provided by this system.

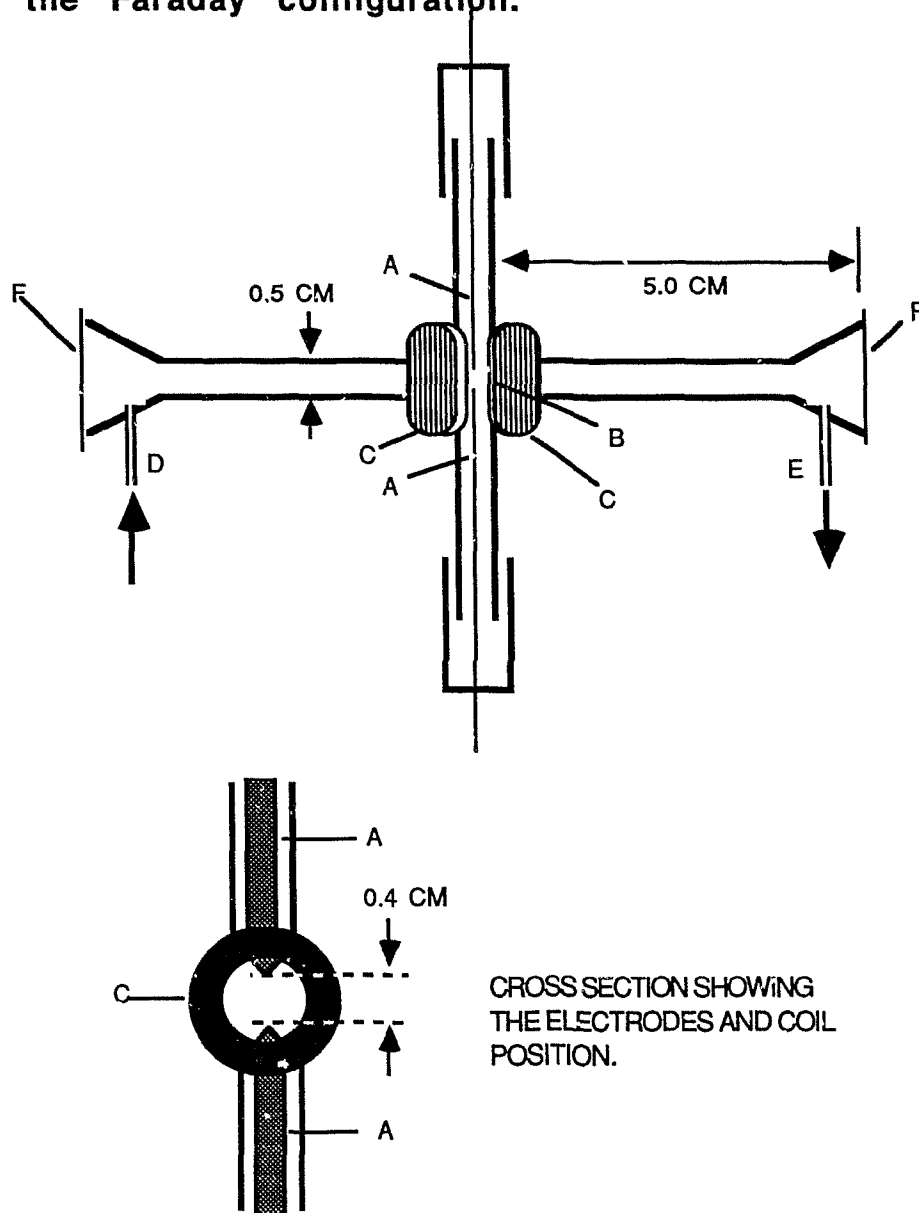
In the present work, the Zeeman effect was successfully applied to correct for the background absorption in a pulsed discharge cell at atmospheric pressure. The 324.5 nm Cu line was used to study the applicability of the Faraday configuration and the 670.8 nm Li doublet was selected in the case of the Voigt configuration.

## 4.2 EXPERIMENTAL.

### 4.2.1 Faraday configuration.

The pulsed discharge cell used to produce the atom population of copper was filled with helium gas at (or slightly above) atmospheric pressure, and had two coils wound at each side of the discharge area to provide for the magnetic field (Figure 4.1). The discharge cell was made out of Pyrex tubing (5 mm o.d.) with a constriction at the centre of the cell to permit more effective winding of the coils. The two coils were insulated from the glass wall by clay paper and wound at each side of the electrode (located in the vertical axis), with each coil centre aligned with the optical axis (horizontal axis). The wire used was 38 gauge (maximum current 0.8 A; 0.46 m/Ω) which was considered to be a good compromise between the number of turns and the current flux. Each coil had 700 turns; a further increase in the number of turns did not improve the magnetic field strength and did not make the field more homogeneous, as the coil geometry departed from the ideal Helmholtz coils (distance between coil centres equal to half the radius of each coil). The equivalent resistance of the two coils connected in parallel was 25 Ω.

**FIGURE 4.1** Diagram of the discharge cell used in the Faraday configuration.



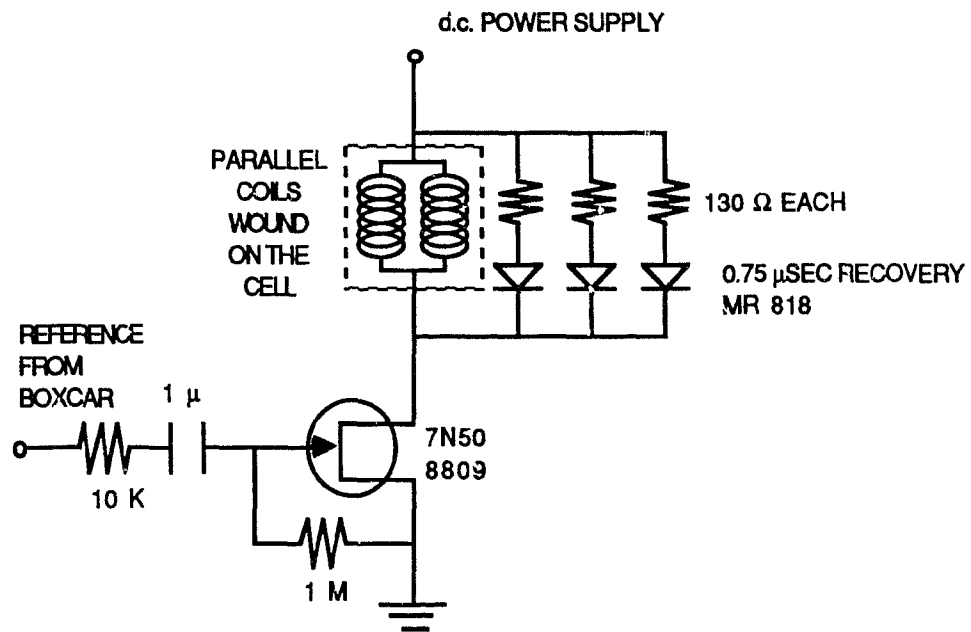
A, copper foil electrodes; B, insulating clay paper; C, coils connected in parallel; D, helium inlet; E, helium outlet; F, cell windows. The optical axis is perpendicular to the plane of the paper in the cross section showing the electrodes and coil position.

A pulsed voltage was applied across the coils to produce the magnetic field. The characteristics of the pulse were determined by the power supply and a FET switch (Figure 4.2) mounted on a heat sink and isolated by a wooden block. Applying the voltage longer than one minute produced overheating of the coils, which was a limitation of this design. A peak field strength of 0.25 Tesla was detected when a 40- $\mu$ sec wide pulse at a repetition rate of 570 Hz and an amplitude of 375 V was applied across the coils (see Appendix B).

The electrodes of the cell were made of copper foil, each of them fixed on a short piece of pyrex tubing into which the vertical ends of the cell were fitted. These pieces were held in place by masking-tape separators.

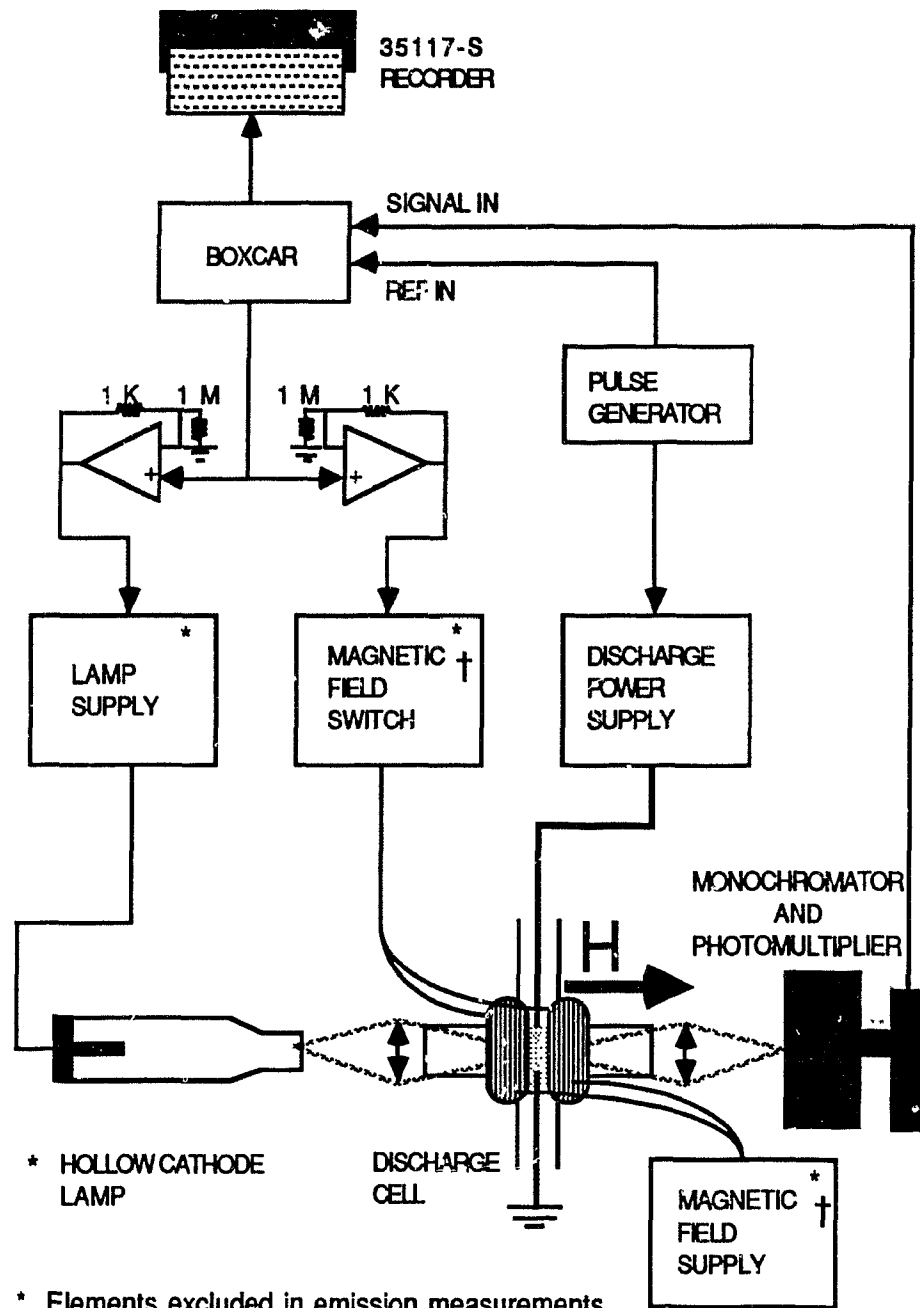
Preliminary measurements which included the emission and absorption of the 324.5 Cu line were carried out using the same system save for the device used to produce the magnetic field. A block diagram for the signal processing can be seen in Figure 4.3. The boxcar (built in the laboratory) took its reference from a pulse generator (built in the laboratory). The same pulse was used to control the timing of the lamp current, magnetic field and the discharge. The discharge was periodically switched off (repetition rate 570 Hz) for 450  $\mu$ sec to control overheating of the discharge cell. This characteristic allowed delayed measurements of the

**FIGURE 4.2** Description of the switch for the magnetic field.



See Figure 4.3 to locate the position of this switch in the system.

**FIGURE 4.3** Block diagram of the processing of the Zeeman, absorption, and emission signals. Faraday configuration.



\* Elements excluded in emission measurements.  
 † Elements excluded in absorption measurements.

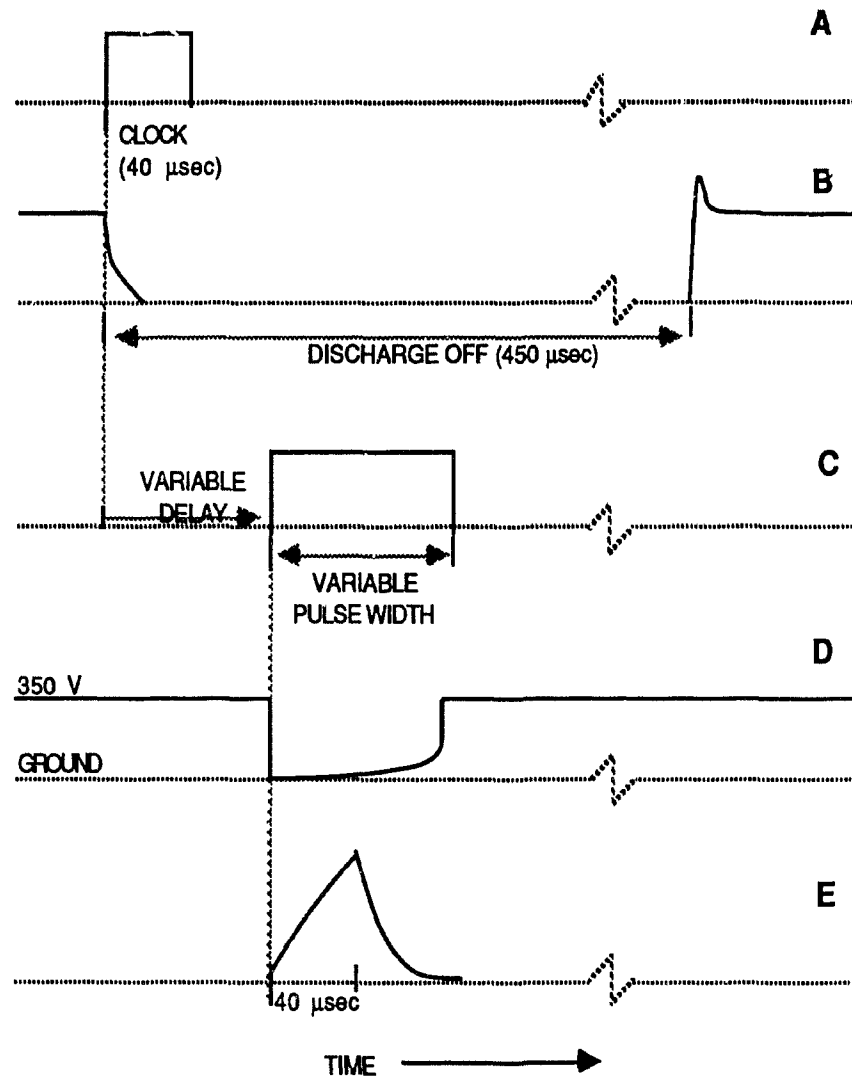
emission, absorption or Zeeman signal to be made over a few  $\mu$ seconds while the discharge was off, and eliminated the background noise from the discharge. Figure 4.4 shows the timing diagram of this system.

Prior to any measurement, the hollow-cathode lamp was warmed up for half an hour. A Be lamp (Varian Techtron Pty. Ltd., Australia) was used for Cu measurements and a Ni lamp (Corning Glass Works of Canada Ltd., Toronto) was used for background measurements. A constant helium flow of 0.3 ml/sec was injected into the cell. A 5-minute purge period was necessary to eliminate air from the cell. The zero baseline was adjusted by blocking the radiation and observing that no displacement to the baseline occurred. While the radiation was blocked, the magnetic field was switched on and the absence of any ghost signal was confirmed. For emission measurements, the lamp and the magnetic field were not turned on. In order to measure absorption, the discharge was stabilized for 5 minutes and the Zeeman signal was measured by switching on the magnetic field for about 20 seconds.

#### 4.2.2 Voigt configuration.

The pulsed discharge cell, filled with helium at atmospheric pressure, was placed in the gap between the poles of a d.c. electromagnet which produced the transverse magnetic field. This configuration eliminated the need for coils wound on the cell and the corresponding problems of overheating and the requirement for a rather complicated power supply.

**FIGURE 4.4** Time diagram of the discharge, the signal, and the magnetic field.

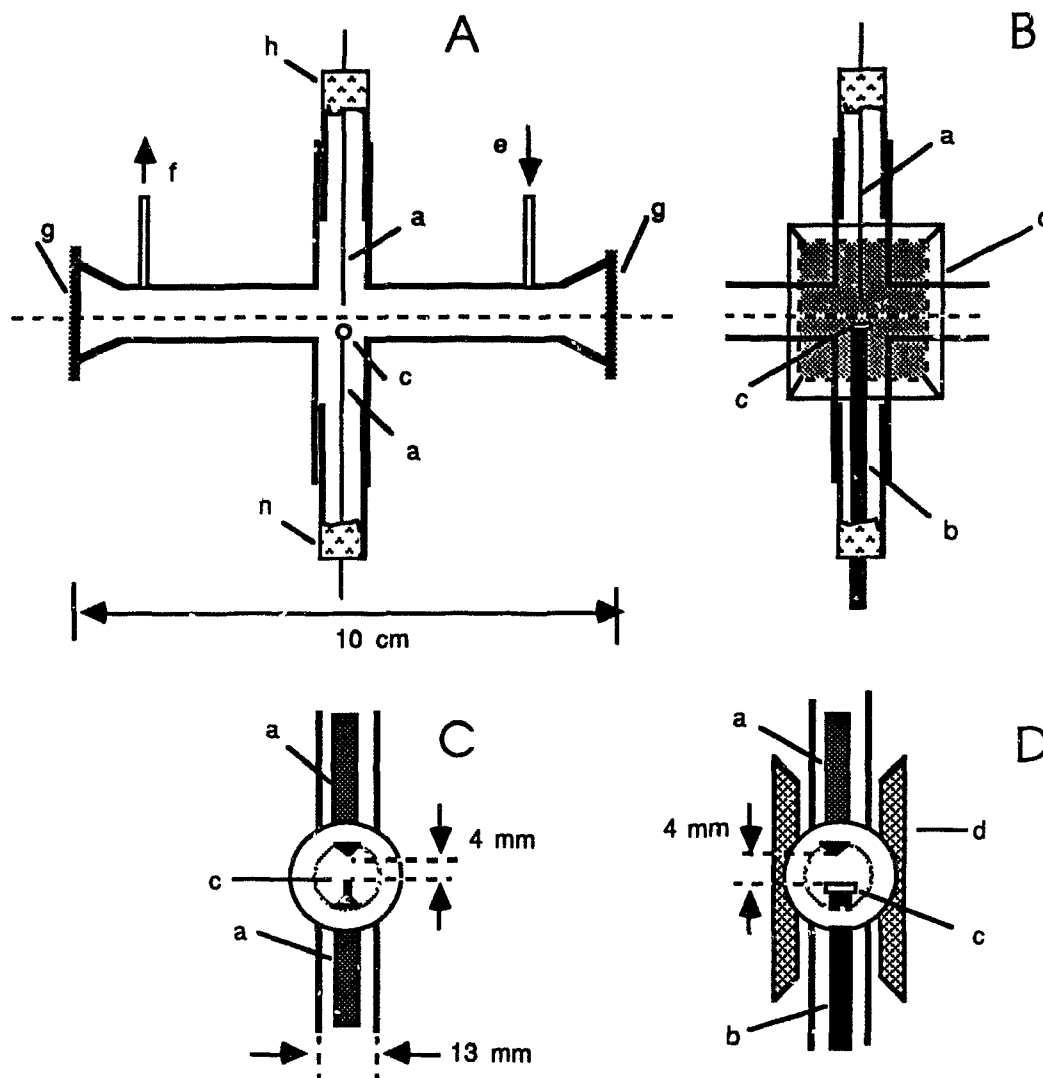


A, clock; B, voltage across the discharge cell; C, delayed reference; D, voltage across the parallel coils; E, magnetic field amplitude (see Appendix A). D and E apply only to the Faraday configuration.

The cell was made of 13 mm O.D. quartz tubing, which provided good dissipation of heat and eliminated the problem of overheating (Figure 4.5). The discharge area was at the intersection of the optical axis with the vertical axis, located approximately at the centre of the faces of the magnet poles. Controlling the position of the discharge area between the poles was not a critical factor, since the magnetic field was quite homogeneous at the centre of the magnet gap. On the other hand, the optical alignment of the discharge had to be controlled precisely. An adjustable holder (Ealing) mounted on the alignment rail fulfilled this requirement. The optical beam was focused on the electrode holding the material to be atomised.

The material tested was 20% LiCl (Fisher Scientific Co.) in graphite in the form of a pellet. The pellet was compacted manually by screwing a bolt ( diameter 3 mm) into a block of aluminium containing the powdered mixture. During the preliminary emission measurement, the pellet was held in place on the copper electrode with a mixture of epoxy glue and graphite powder, or by a thin copper wire compacted within the mixture and wrapped around the copper electrode (Figures 4.5 A and C). The second alternative was preferred to the first one to hold the material since it was more practical. For the dichroic and preliminary absorption measurements the pellet was placed on top of the flat end of a piece of copper tubing which served as the electrode (Figures 4.5 B and D). With this approach, the destruction of the pellet observed when it was held by a copper wire was retarded. The longer lifetime of the

**FIGURE 4.5** Diagrams of the discharge cells used in the Voigt configuration.



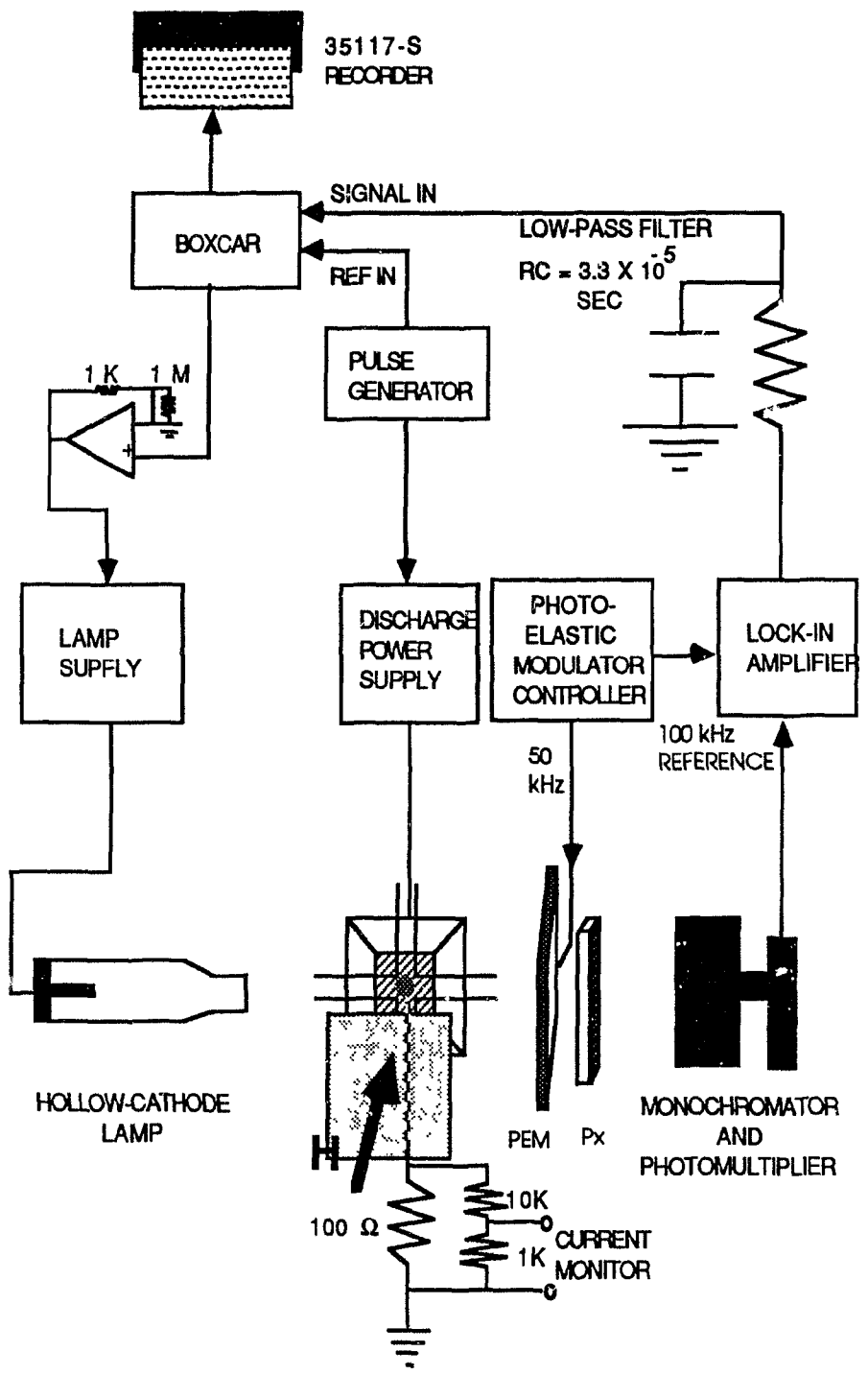
For emission measurements, the pellet was held by a thin copper wire compressed in the mixture and wrapped around the copper foil electrode, (A,C). For absorption and dichroic measurements, the pellet lay flat on the tip of the copper tube electrode, (B,D). In A and B the optical axis is parallel to the plane of the page; in C and D the optical axis is perpendicular to the plane of the page. a, copper foil electrodes; b, copper tubing electrode; c, pellet; d, magnet; e, helium inlet; f, helium outlet; g, cell windows; h, epoxy-glue.

pellet was attributed to better compaction and to the larger area on the surface of the pellet where the discharge occurred.

A diagram of the optical configuration and signal processing is shown in Figure 4.6. The source of radiation was a pulsed lithium hollow-cathode lamp (63060, Instrumentation Laboratory, Wilmington, MA). The absorbing discharge cell was placed in the gap of a d.c. electromagnet, where the radiation was focused by a collimating quartz lens. The  $P_x$  polariser provided discrimination between  $\pi$  and  $\sigma$  components, allowing the detection of dichroism. An MP-1018A monochromator (McKee-Pedersen instruments, Danville, CA) and a 100 kHz tuned photomultiplier pre-amplifier (assembled in the laboratory) were used as wavelength selector and detector respectively. A photoelastic modulator (Hinds International Inc., Portland, Oregon) rotated  $45^\circ$  with respect to the vertical axis, and modulated at 50 kHz, eliminated flicker noise.

The electronic signal was processed by a high-frequency lock-in amplifier to measure the 100 kHz dichroic signal resulting from the 50 kHz modulation of the retarder (Figure 4.6). A boxcar (built in the laboratory) was used to delay the measurement of the signal until the discharge was off. Both the boxcar and the discharge power supply took their reference pulse from a pulse generator (built in the laboratory). The reference for the hollow-cathode lamp power supply was a delayed pulse from the boxcar. The time diagram is the same as shown in Figures 4.4 A, B and C.

FIGURE 4.6 Block diagram of the processing of the dichroic signal. Voigt configuration.



The signal associated with the intensity of the detected radiation is calculated by means of the Jones calculus (see Appendix A) as:

$$S(2\omega_p) = \text{constant} \times I^0 [\exp(-K_\pi N \ell) - \exp(-K_\sigma N \ell)] \quad (42)$$

where  $I^0$  is the intensity of the incident radiation to the cell;  $K_\sigma$  and  $K_\pi$  are the absorption coefficients of the  $\sigma$  and  $\pi$  components respectively,  $N$  is the density of absorbing atoms, and  $\ell$  is the length of the absorption region. The expression  $2\omega_p$  represents the 100 kHz frequency used as a reference for the lock-in amplifier.

#### 4.2.3 Procedure.

Prior to any measurement, the Li hollow-cathode lamp was warmed up for half an hour. Parameters such as wavelength setting, wavelength retardance of the photoelastic modulator, phase shift of the 100 kHz signal, and optical alignment were optimised by producing a dichroic signal with a quartz plate at the discharge region. A constant helium flow of 0.3 ml/sec was injected into the cell and a 5-minute purge period was necessary to eliminate air from the cell. While the radiation was blocked, the magnetic field was switched on and the absence of any ghost signal was confirmed. There was no limitation on the time the field was kept on, although 30 to 60 seconds was normally enough to obtain reliable measurements.

The relative time for which the discharge was kept on and off at a constant repetition rate (i.e. the duty cycle) was also investigated. Usually, stabilisation of the discharge took about five minutes. Optimisation of the reference pulse length was also carried out. Since this changed the duty cycle of the hollow-cathode lamp current, adjustments to the lamp current were made and about 15 minutes were then allowed to elapse prior to any measurement.

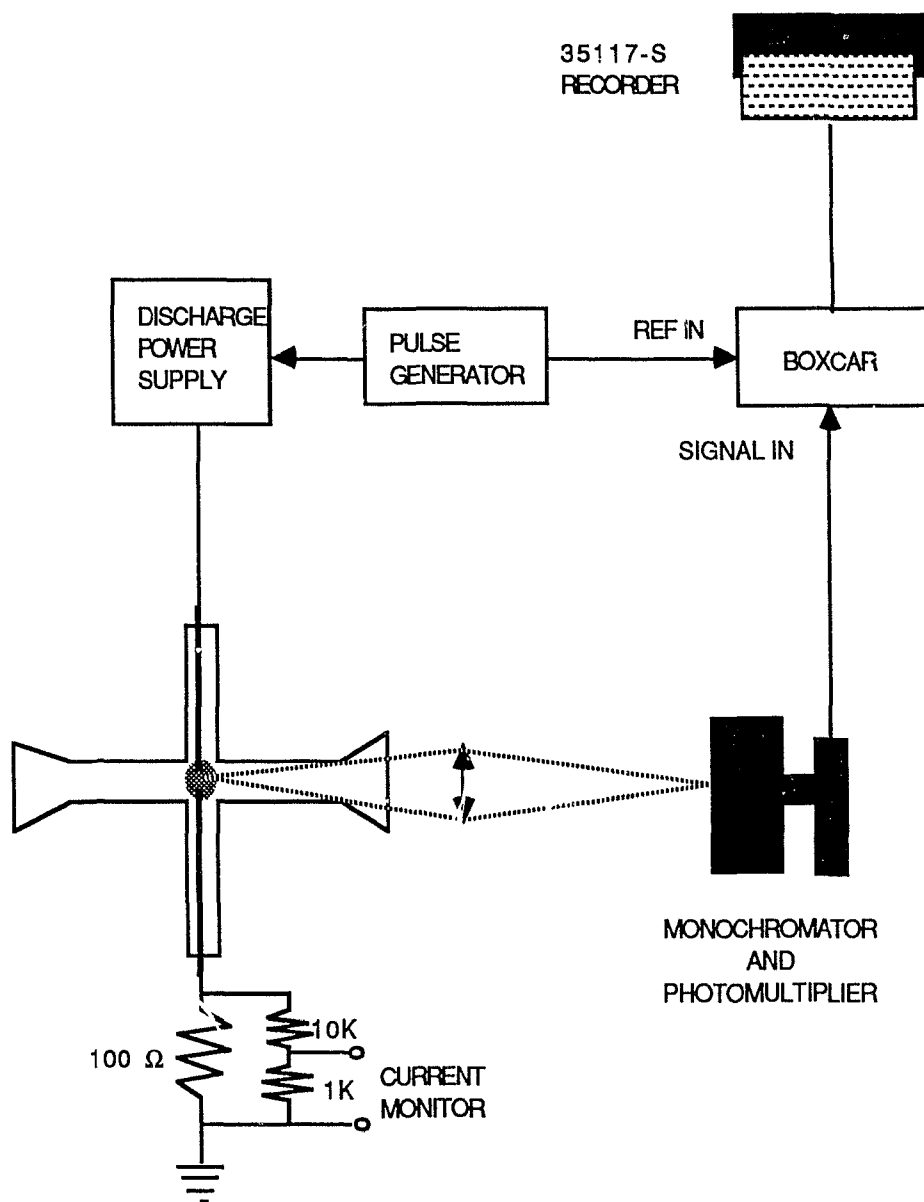
Before any dichroic measurement, tests for the emission of lithium at 670.8 nm were made. The signal processing used is described in Figure 4.7. Periodically switching the discharge off permitted delayed measurements of emission. The pulse generator provided the reference for both the discharge and the boxcar. The MP-1018A monochromator (McKee-Pedersen Instruments, Danville, CA) and an MP-1021 photomultiplier tube (McKee-Pedersen Instruments, Danville CA) were used as wavelength selector and detector respectively. Identification of the emission of Li involved observation of the colour of the discharge, wavelength scan close to the 670.8 nm Li line, and measurement of the intensity of emission versus discharge current.

## **4.3 RESULTS AND DISCUSSION.**

### **4.3.1 Faraday configuration.**

In order to show that the discharge cell at atmospheric pressure was able to produce an atom population, the emission, atomic absorption, background absorption, and Zeeman signal of the

FIGURE 4.7 Block diagram of the processing of the emission signal. Preliminary measurement to the detection of the dichroic signal.



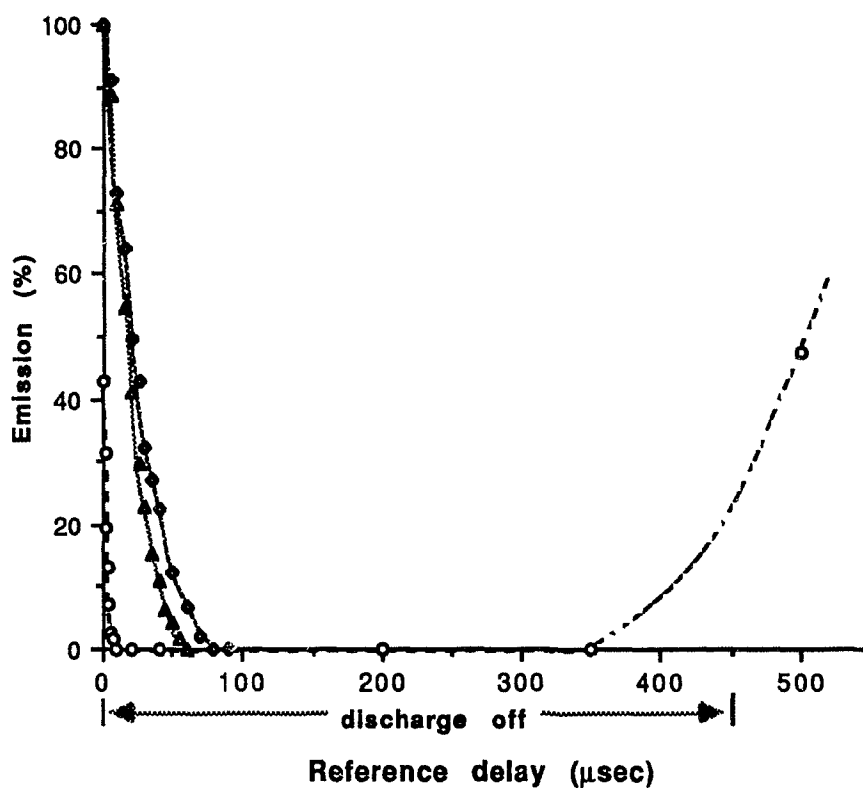
324.8 nm Cu line were measured.

In this particular arrangement, periodically switching the discharge off provided an effective way of to control background emission and to prevent overheating of the cell. Previous attempts to measure emission, absorption, and the Zeeman signal using a continuous discharge were accompanied by a poor signal-to-noise ratio and overheating.

The delayed measurement of emission after the discharge is switched off is shown in Figure 4.8. The measurements were done at the 324.8 nm Cu line and at two close wavelengths, 323.8 nm and 325.3 nm.; i.e. wavelengths where emission should be mainly attributable to the plasma. The emission at the above wavelengths decays to 10% of its peak value in about 40, 60, and 10  $\mu\text{sec}$  respectively. The emission at 324.8 nm (Cu line) and 323.8 nm can not be detected even 50  $\mu\text{sec}$  after the discharge is switched back on. On the other hand, the emission at 325.3 nm starts as soon the discharge is switched on. Since emission does not present the required decay pattern at the copper line, periodically switching the discharge off does not permit atomic emission measurements to be separated from background emission.

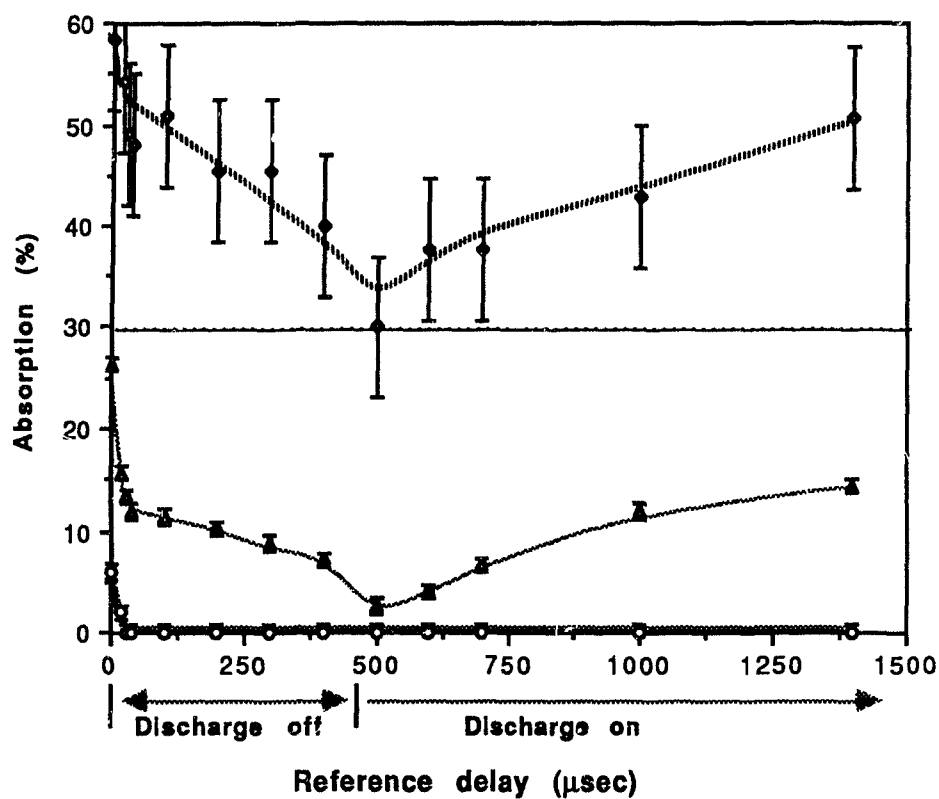
The delayed measurements of atomic absorption and background absorption can be seen in Figure 4.9. The atomic lines used were the 324.8 nm Cu line and the 341.5 nm Ni line, respectively. The background absorption at the moment the discharge is switched off

**FIGURE 4.8** Decay of the copper emission at the 324.8 nm Cu line.



The emission of copper at 324.8 nm, of background at 323.8 nm, and background at 325.3 nm are represented by  $\Delta$ ,  $\diamond$ , and  $\circ$  respectively. Discharge RF frequency 570 kHz; off cycle 450  $\mu\text{sec}$  every 10.0 msec. Reference pulse width 20  $\mu\text{sec}$ . The detail of the cell and the signal processing are shown in the Figures 4.1 and 4.3 respectively.

**FIGURE 4.9** Decay of the absorption and the Zeeman signals of the 324.8 nm Cu line.



The atomic absorption, Zeeman (X10; +30 offset) and background absorption signals are represented by  $\Delta$ ,  $\diamond$ , and  $\circ$  respectively; source for the background absorption measurement 341.5 nm Ni line; error bars are the standard deviation of three measurements. Peak magnetic field  $0.25 \pm 0.03$  Tesla. Source current 150-mA, 40- $\mu$ sec pulse. Discharge RF frequency 570 kHz; off cycle 450  $\mu$ sec every 10.0 msec. The detail of the cell and the signal processing are shown in the Figures 4.1 and 4.3 respectively.

is notably high. Scattering of the radiation by solid particles such as graphite particles still present when the discharge is switched off may account for the background absorption noted. The fast decay of the background absorption (it takes 25  $\mu\text{sec}$  to decay completely to zero absorption) compared to the slow decay of the atomic absorption (which does not decay completely to zero during the 450  $\mu\text{sec}$  the discharge is off) clearly indicates that a background-free absorption measurement can be obtained when the measurement is delayed 25  $\mu\text{sec}$ . The atomic absorption of copper begins to increase smoothly when the discharge is switched back on, while the background absorption is negligible even 1000  $\mu\text{sec}$  after the discharge is switched back on (Figure 4.9).

The Zeeman signal of the 324.8 nm Cu line is relatively small (the amplitude is exaggerated 10 times in Figure 4.9) compared to the associated absorption signal, and the signal-to-noise ratio is poor. Nevertheless, it is important to note that its decay after the discharge is switched off follows the general trend of the absorption signal. As expected, no Zeeman signal associated with the background absorption was detected.

It may be concluded that Zeeman background correction can be applied to a discharge cell at atmospheric pressure although a poor signal-to-noise ratio is obtained with this particular apparatus. In principle, the discharge cell could be run continuously to measure absorption when Zeeman background absorption is applied, provided another way was used to control overheating of the cell. Therefore,

in this particular case, the use of a periodically switched discharge to control background absorption may be redundant when Zeeman background correction is applied.

The absorption and Zeeman measurements versus the RF current of the 324.8 nm copper line are shown in Figure 4.10. The Zeeman signal shows a maximum and a further increase of the RF current beyond 25 mA pp does not improve its signal-to-noise ratio.

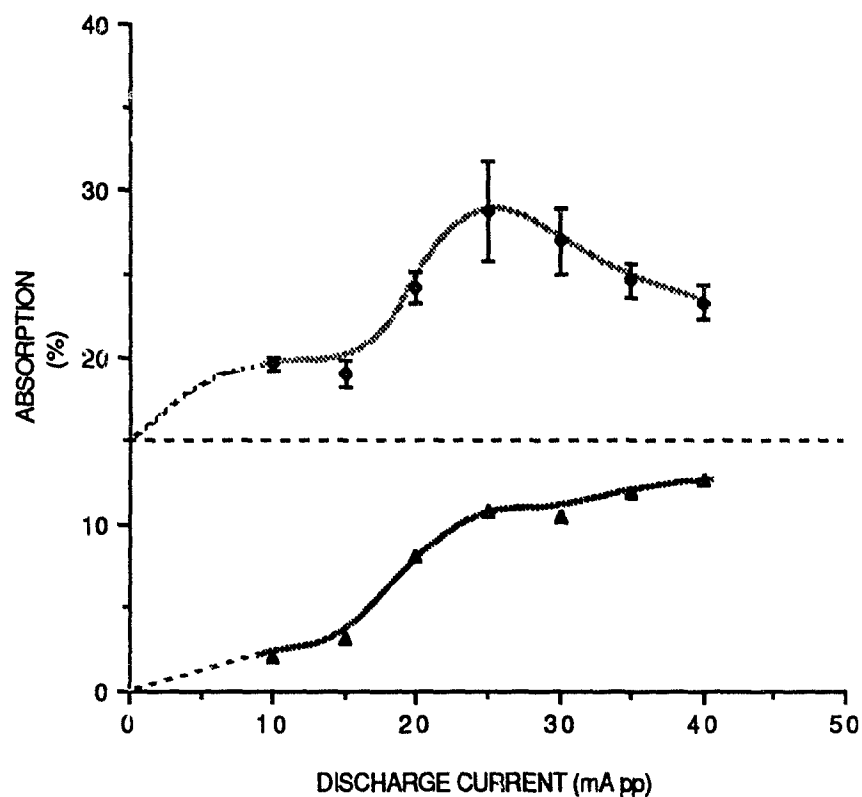
In conclusion, background absorption correction in a pulsed discharge cell filled with helium at atmospheric pressure was achieved by applying the Zeeman effect. However, the Zeeman signal showed a poor signal-to-noise ratio and low sensitivity. This problem was not alleviated by increasing the discharge current.

#### 4.3.2 Li emission measurements.

The emission of Li at 670.8 nm by the discharge cell was detected (Figure 4.11). Background emission was negligible since no signal could be detected when the pellet was made of graphite alone. This is attributed to the absence of plasma emission, because the discharge was off during the measurement. Since atomic emission and background emission show different decay patterns this cell can be used as an emission source. In addition, the atomic emission confirms the presence of lithium atoms in the cell.

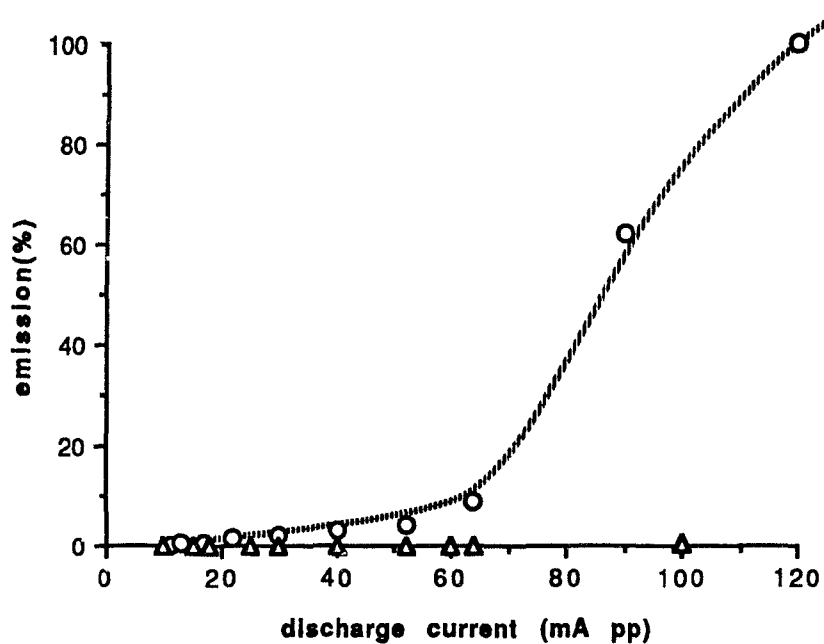
If the emission signal is proportional to the atom population of Li, the emission versus the discharge current curve (Figure 4.11)

**FIGURE 4.10 Absorption and Zeeman signals of the 324.8 nm Cu line versus discharge current.**



The absorption and Zeeman ( X10; +15 offset) signals , are represented by  $\Delta$ ,  $\diamond$  respectively; error bars are the standard deviation of three measurements. Peak magnetic field  $0.25 \pm 0.03$  Tesla. Source current 150-mA, 40- $\mu$ sec pulse. Discharge RF frequency 570 kHz; off cycle 450  $\mu$ sec every 10.0 msec. The detail of the cell and the signal processing are shown in the Figures 4.1 and 4.3 respectively.

**FIGURE 4.11 Emission at the 670.8 nm Li line versus discharge current in a pulsed discharge cell.**



Lithium (o) and background (Δ) emission are obtained by atomising 20% LiCl in graphite and 100% graphite respectively. Reference pulse 300 μsec. Discharge RF frequency 570 kHz; off cycle 450 μsec every 2.0 msec. The detail of the cell and the signal processing are shown in the Figures 4.5 A,C and 4.7 respectively.

also suggests that the process responsible for producing the atomic population is not singular. At RF currents below 60 mA, the emission signal increases linearly with the discharge current, but at currents above 60 mA, the slope of the curve increases sharply. It is proposed that in the first case, sputtering gives rise to the population of lithium atoms, while at high currents thermal vaporisation becomes important.

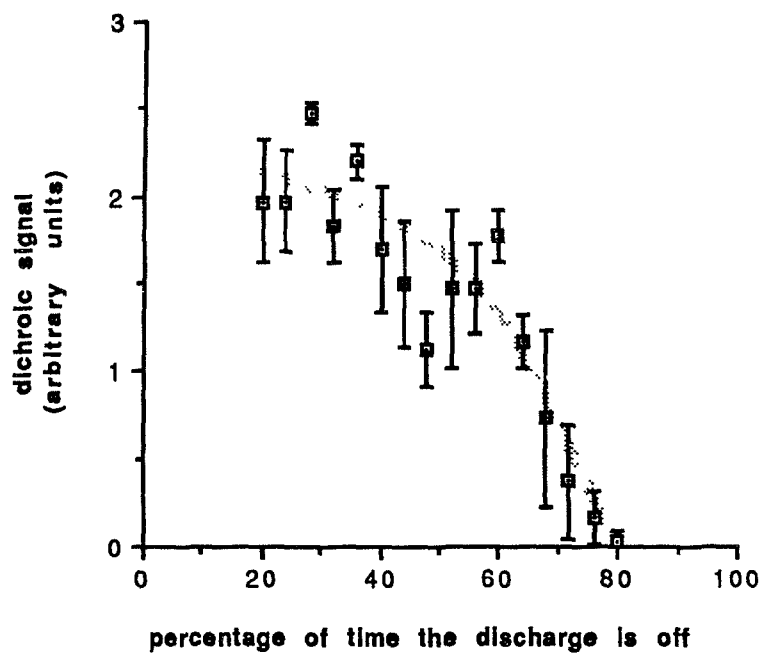
#### 4.3.3 Li dichroic measurements.

The dependence of the dichroic signal of the 670.8 nm Li line on the duty cycle of the discharge, the decay of the signal when the reference pulse is delayed, and the effect of field strength were investigated.

In order to check the authenticity of the signal, the absence of any dichroic signal was confirmed when a graphite pellet not containing any lithium chloride was used as a blank.

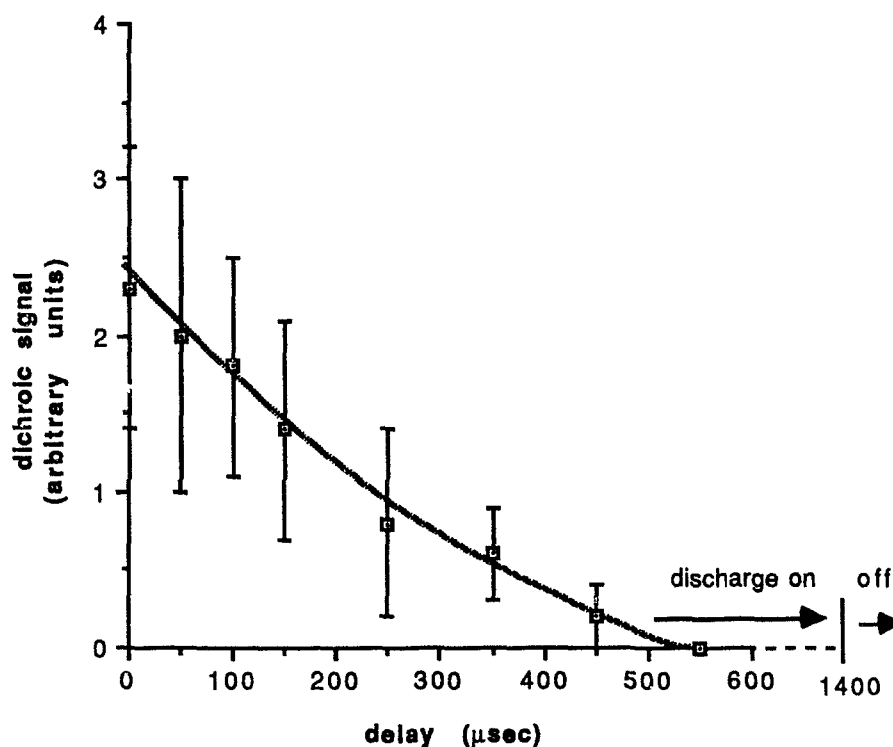
The dichroic signal of the 670.8 nm Li line was found to be strongly influenced by the length or the period during which the discharge was on (Figure 4.12). Every 2500  $\mu$ sec the discharge was switched off. As the on-time was decreased, the population of lithium atoms fell and the associated signal was correspondingly reduced. An attempt to use a discharge with on and off periods of equal length showed a rapid decay of the dichroic signal as the reference pulse was delayed (Figure 4.13). When the off-time of the discharge was reduced to about one quarter of the discharge cycle,

**FIGURE 4.12** Dependence of the dichroic signal of the 670.8 nm Li line on the duty cycle of the discharge cell.



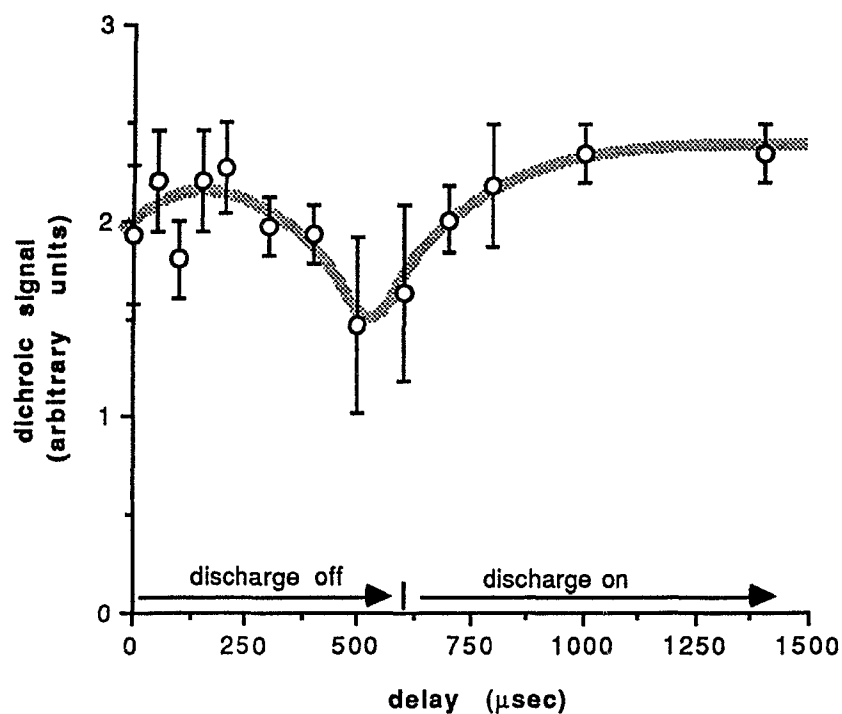
Discharge current 200 mA pp; RF frequency 570 kHz; repetition period 2.5 msec. Atomised material 20% LiCl in graphite. Reference pulse 250  $\mu$ sec. Source current 29 mA p. Field strength was 0.577 Tesla d.c. The detail of the cell and the signal processing are shown in the Figures 4.5 B,D and 4.6 respectively. Error bars are the standard deviation of three measurements.

**FIGURE 4.13** Dependence of the dichroic signal of the 670.8 nm Li line on the delay of the reference pulse. Discharge off 52% of the repetition period.



Discharge current 210 mA pp; RF frequency 625 kHz; repetition period 2.7 msec. Atomised material 20% LiCl in graphite. Reference pulse 80 μsec. Source current 150 mA p. Field strength was 0.577 Tesla d.c. The detail of the cell and the signal processing are shown in the Figures 4.5 B,D and 4.6 respectively. Error bars are the standard deviation of three measurements.

**FIGURE 4.14** Dependence of the dichroic signal of the 670.8 nm Li line on the delay of the reference pulse. Discharge off 24% of the repetition period.



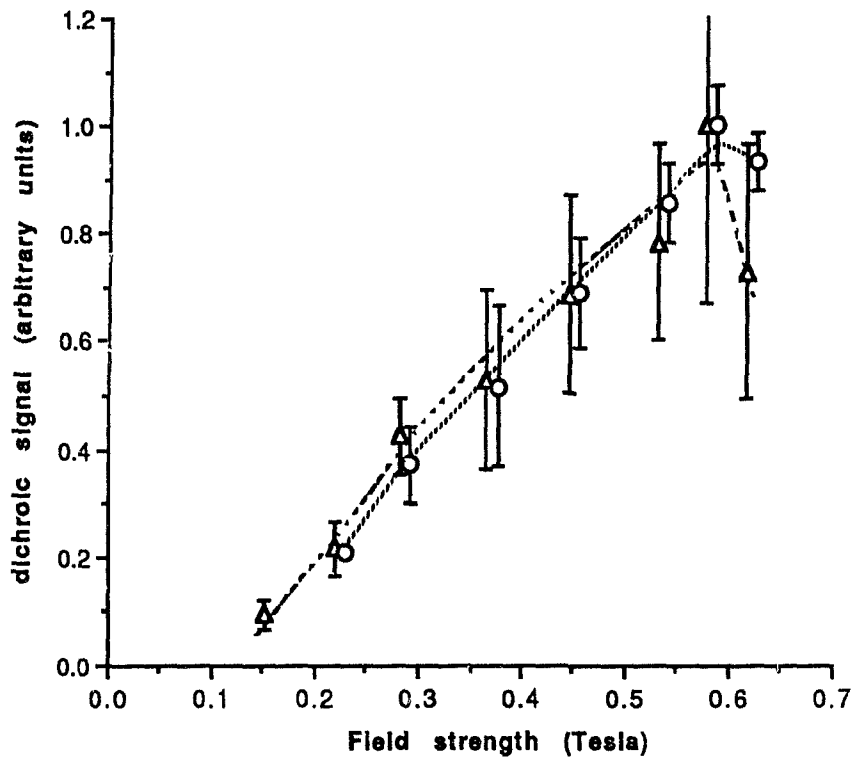
Discharge current 200 mA pp; RF frequency 625 kHz; repetition period 2.5 msec. Atomised material 20% LiCl in graphite. Reference pulse 80  $\mu\text{sec}$ . Source current 150 mA p. Field strength was 0.577 Tesla d.c. The detail of the cell and the signal processing are shown in the Figures 4.5 B,D and 4.6 respectively. Error bars are the standard deviation of three measurements.

the signal did not decay appreciably as the reference pulse was delayed (Figure 4.14). This last option was adopted in order to obtain a more or less continuous population of lithium atoms.

The measurement of the dichroic signal at the 670.8 nm Li line versus field strength is shown in Figure 4.15. The signal was determined using two sets of conditions for lamp currents and reference pulses. The duty cycle of the lamp current was closely monitored to avoid exceeding the maximum power dissipation of the hollow-cathode lamp. Interestingly, the response curves obtained using 48 and 84 mA p show the same form, with a maximum at about 0.55 Tesla. The results shown in Figure 4.15 appear to be the first time that the Paschen-Back effect has been seen to have a significant impact on the response of an instrument under the sort of conditions used to make an analytical measurement. This point is discussed in more detail in Appendix C.

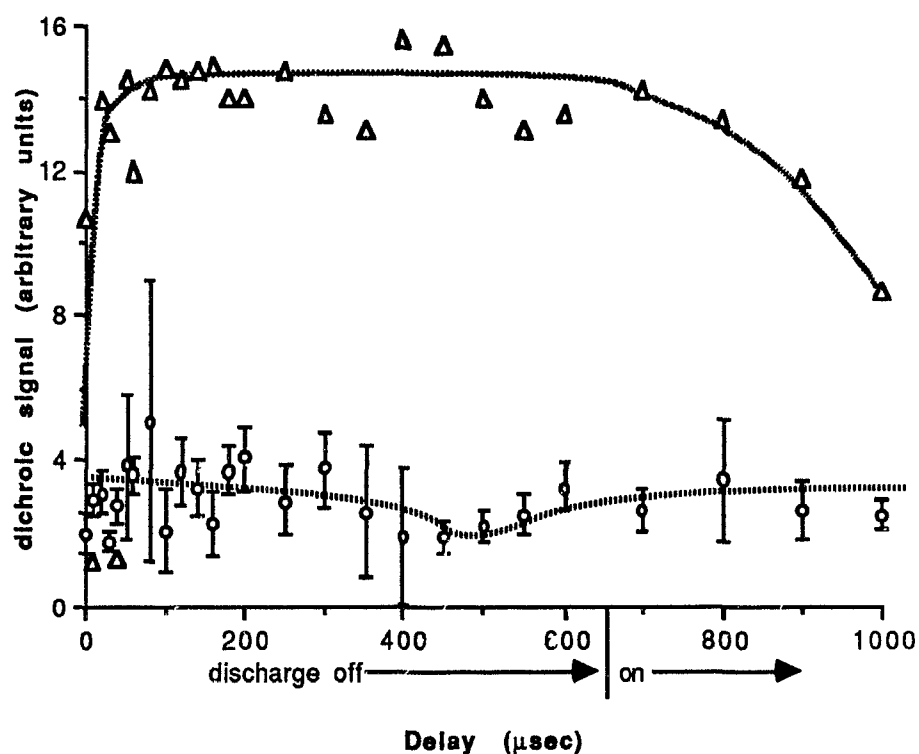
One of the major concerns in this work was to identify the main contribution to the signal noise. Alternate measurements of dichroism caused (i) by the population of lithium atoms in the presence of a magnetic field, and (ii) by a quartz plate (with the magnetic field kept off and the discharge in operation) were carried out. This quartz plate, at a fixed angle, was placed close to the window of the discharge cell intersecting the optical axis. The averages of the signals from the quartz plate and of the lithium response are shown in Figure 4.16. Since the noise of the signals produced by the quartz plate is relatively small, the main

**FIGURE 4.15** Dichroic signal of the 670.8 nm Li line versus field strength.



A 84-mA p 250- $\mu$ sec pulse (o) or a 48 mA p 500- $\mu$ sec pulse ( $\Delta$ ) was used for the hollow-cathode lamp. The signals are normalised; error bars are the standard deviation of three measurements. Discharge current 210 mA pp; RF frequency 625 kHz; time off 600  $\mu$ sec every 2.5 msec. Atomised material 20% LiCl in graphite. Reference pulse 80  $\mu$ sec. Source current 150 mA p. Field strength was 0.577 Tesla d.c. The detail of the cell and the signal processing are shown in the Figures 4.5 B,D and 4.6 respectively.

**FIGURE 4.16 Comparison of the dichroic signal produced by lithium vapour surrounded by a magnetic field and a quartz plate.**



Atomisation of 20% of LiCl in graphite in presence of 0.577 Tesla d.c. provided the lithium signal (o). A quartz plate, rotated 45° from the vertical axis, produced the dichroic signal (Δ). Discharge current 210 mA pp; RF frequency 625 kHz; discharge off 650 µsec; repetition period 2.2 msec. Reference pulse 80 µsec. Source 670.8 nm Li line; current 150 mA p. The detail of the cell and the signal processing are shown in the Figures 4.5 B,D and 4.6 respectively.

contribution to noise can be related to the population of lithium atoms in the plasma and not to photon noise or other sorts of optical interference from the discharge.

The importance of switching the discharge off during the measurement can also be noted in Figure 4.16. The quartz plate signal lost sensitivity when the reference delay was close to zero or when it overlapped the interval when the discharge was on. This can be attributed to a high background absorption level which was absent while the discharge was off. On the other hand, no loss of sensitivity of the signal of the lithium atoms while the discharge was on could be observed.

In conclusion, it can be said that the process of atomisation is the main source of noise in the dichroic measurement of the 670.8 nm Li line when the source of lithium is a mixture of 20% LiCl in graphite. A different approach to fabrication of the electrode is required. The advantages of the system for background correction could not be fully appreciated because of the lack of high background absorption level while the discharge is switched off. However, an indirect indication of the level of background absorption is given in Figure 4.16 by measurements done with the quartz plate while the discharge was on. Despite the complication in the electronics of the pulsed discharge, this approach makes it possible to avoid overheating the cell and eliminates background emission and absorption by delaying the measurement of the dichroic signal.

## **5. APPLICATION OF ZEEMAN BACKGROUND CORRECTION IN THE DETERMINATION OF Al, Cd, Co, Cr, Cu, Fe, Pb, Mg, Ni, Ag, and Zn ATOMISED IN A CONTINUOUS DISCHARGE CELL AT ATMOSPHERIC PRESSURE.**

### **5.1 PURPOSE.**

A discharge cell filled with helium at atmospheric pressure was successfully applied to atomise Cu and Li, as described in Chapter 4. Furthermore, the Zeeman background correction method was found to be feasible using the Faraday or the Voigt configuration. The purpose of the present study was to extend the use of the Zeeman background correction method described in the section 4.2.2 to Al, Cd, Co, Cr, Cu, Fe, Pb, Mg, Ni, Ag, and Zn . The Voigt configuration combined with a continuous discharge cell was chosen in this case.

It was also used to determine silver and lead electrodeposited on the electrode of the discharge cell prior to atomisation. The influence of the concentration of the silver solution, of the length of the deposition period, and the influence of stirring the solution during deposition were investigated.

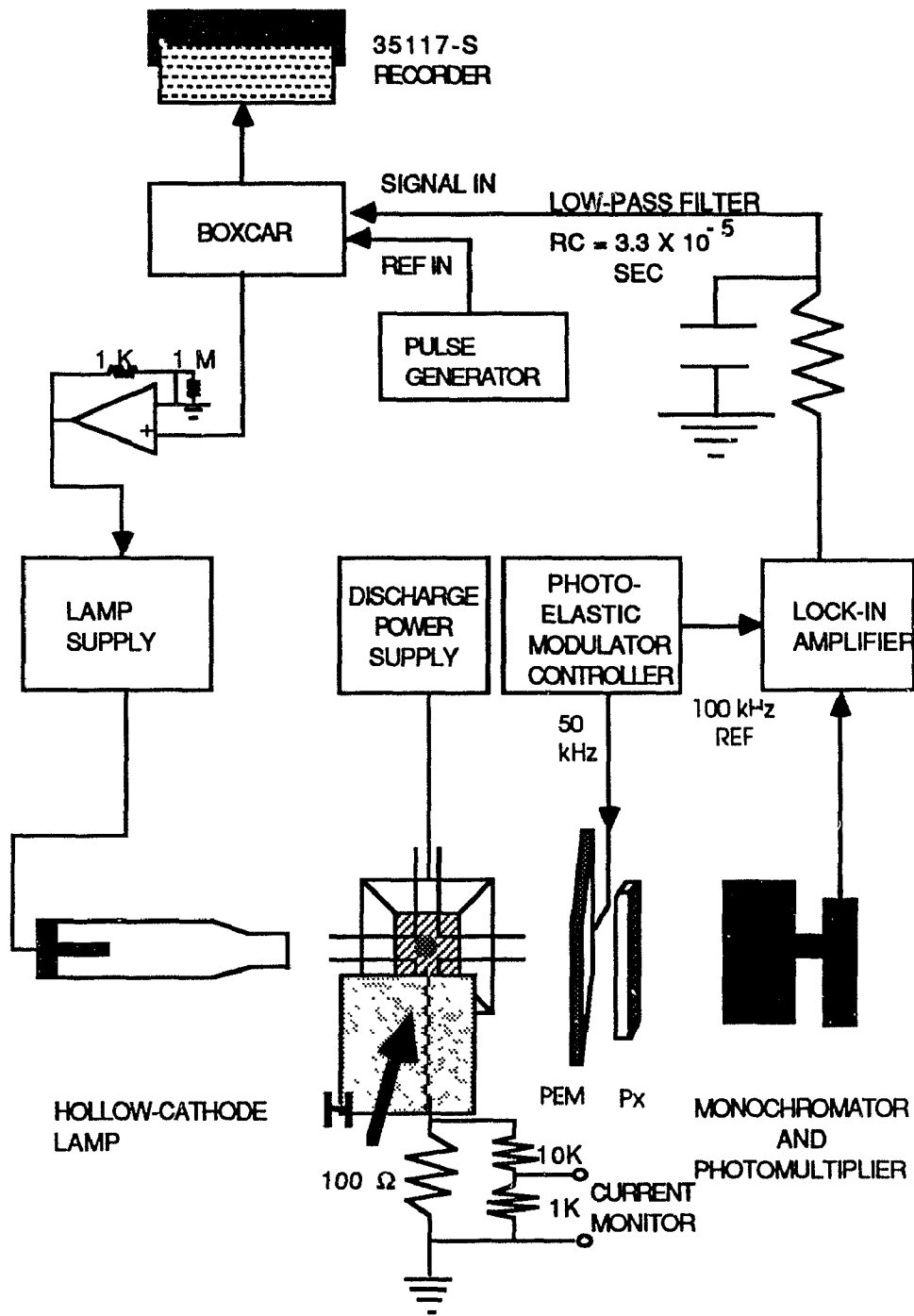
## 5.2 EXPERIMENTAL

### 5.2.1 Direct atomisation of Al, Cd, Co, Cr, Cu, Fe, Pb, Mg, Ni, Ag, and Zn.

The discharge cell was similar to the cell used in the system described in section 4.2.2 (Figure 4.5 B, D), except for the electrodes. A thin metallic sheet of the element to be investigated was used as the ground electrode. The electrode was cleaned with concentrated nitric acid and crimped onto a copper foil which provided electrical contact with the rest of the circuit and also served as a heat sink. The optical beam (about 3 mm cross section at the discharge point) was focused precisely on the electrode of interest. The tip of the electrode was located approximately at the centre of the optical beam.

The block diagram of the signal processing is shown in Figure 5.1. The arrangement is similar to that shown in Figure 4.7 except that a continuous discharge was used in the present case. Continuous operation of the discharge eliminated the need for an individual optimisation of the conditions to atomise each element required in pulsed discharge cell. The high-frequency lock-in amplifier processed the 100 kHz dichroic signal resulting from the 50 kHz modulation of the retarder. The boxcar, used to generate a pulsed reference for the hollow-cathode lamp, was set to produce a square wave reference, which was found to produce the best signal-to-noise ratio.

**FIGURE 5.1** Block diagram of the processing of the dichroic signal when the atomiser is a continuous discharge cell. Voigt configuration.



The preparation of the system prior to the measurement of the dichroic signal of each element was similar to that used to detect the dichroic signal of the 670.8 nm lithium line described in section 4.2.3. The comments included in that section about the duty cycle of the discharge and the delay of the reference do not apply in this case. The emission measurements described in that section were not carried out in this case. The hollow-cathode lamps used were Al, Be (also used for Cu measurements), Cr, Mg, Zn (Varian Techtron, Pty. Ltd., Australia), Ag, Cd, Fe, Ni (Corning Glass Works of Canada Ltd, Toronto), Co (Intensitron Lamp, Perkin Elmer, Norwalk, CN), and Pb (S & J Juniper & Co., Harlow, England).

The authenticity of the dichroic signal of each element was confirmed by using a close line of a different element as a source of radiation and keeping the same conditions in the discharge cell. The absence of "ghost" dichroic signals indicated the effectiveness of the Zeeman background correction method.

#### 5.2.2 Deposition of silver and lead

In this work, electrodeposition was combined with the Zeeman-corrected instrument using a discharge cell at atmospheric pressure as the atomisation device. This approach was used to show the feasibility and ease of combining the two methods, and to estimate the detection limits of the instrument for silver and lead.

Direct immersion of a metallic copper sheet in a solution of silver ions depleted in cupric ions produces an autogalvanic process which results in the deposition of metallic silver on the copper sheet and the release of cupric ions into solution (the standard reduction potentials of silver and copper are 0.799 V and 0.339 V respectively). In the present work,  $1.00 \times 10^{-2}$  -  $1.00 \times 10^{-8}$  M aqueous silver solutions ( $\text{AgNO}_3$ , Anachemia Chemical Ltd., Montreal) were used. The copper electrode was immersed in the test solution. The copper electrode was a thin sheet (3.0 mm long, 1.0 mm wide, 0.3 mm thick). It was cleaned by immersion in concentrated nitric acid followed by repetitive washes with distilled water. Then the electrode was immersed to a fixed depth in the silver solution to be measured. When the deposition period was over, the electrode was removed from the solution and carefully rinsed with distilled water. The electrode was then crimped to the supporting copper sheet, placed in the discharge cell, and analysed according to the procedure described in section 5.2.1. The d.c. field was switched on before the discharge was ignited in order to detect dichroic signals of rapid decay.

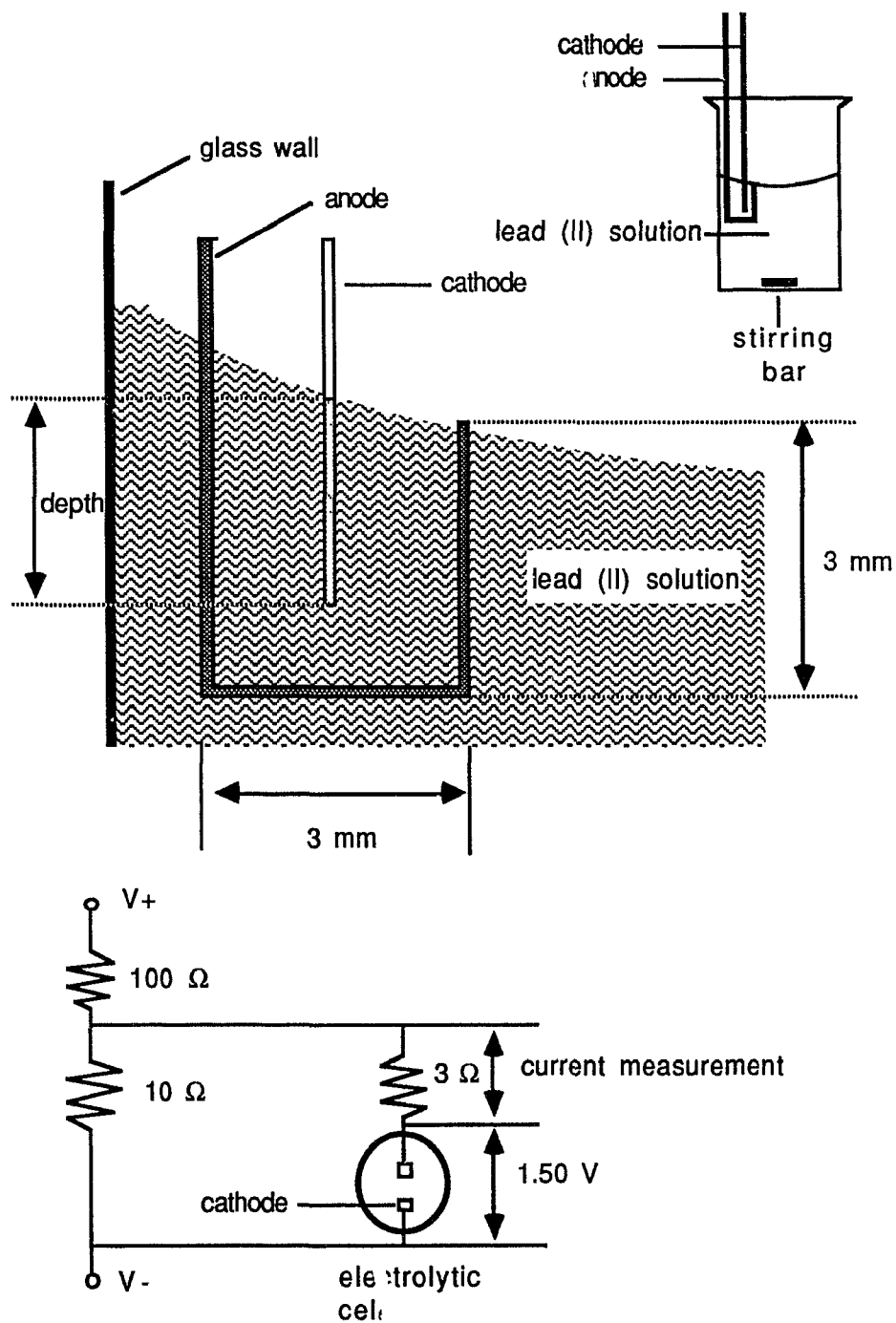
The influence of the concentration of the silver solution, of the length of the immersion period, and of stirring the silver solution during deposition on the dichroic signal of silver were investigated. The solution was stirred by means of a magnetic stirrer.

In order to estimate the detection limit for silver of this instrument, it was assumed that the number of copper ions released into solution was the result of the redox reaction between the metallic copper and the aqueous silver ions. The copper electrode was immersed in the solution of silver ions contained in a 10 ml volumetric flask. When deposition was over, the determination of the concentration of copper ions by conventional flame atomic absorption (AA Varian Techtron, Pty. Ltd, Australia) corresponding to different signal-to-noise ratio of the dichroic signals for Ag (328.1 nm) permitted the detection limit of the instrument to be estimated.

The deposition of lead on a sheet of metallic copper was carried out in an electrolytic cell (Figure 5.2). The anode and the cathode were made out of metallic copper and were not isolated from each other in different cell compartments. A constant voltage of 1.50 V was maintained across the cell. Lower voltages failed to deposit any material capable of producing a dichroic signal. Care was always taken to stir the solution of lead ions perpendicularly to the cross section shown in Figure 5.2. The cathode also served as the carrier of the metallic lead to be atomised in the discharge cell. Its preparation and handling prior to atomisation were the same as for the case of silver deposition.

The influence of deposition time and concentration of the lead ions in solution on the dichroic signal of Pb (283.3 nm) were studied. The range of concentrations investigated were from  $1.00 \times 10^{-3}$  to

**FIGURE 5.2** Detail of the cell and the electric circuit used in the electrodeposition of lead ions on the electrode.



$1.00 \times 10^{-5}$  M  $(\text{Pb}(\text{NO}_3)_2$ , Fisher Scientific Co., NJ). In order to estimate the detection limit of the instrument, the amount of lead deposited on the electrode corresponding to each of the signal-to-noise ratios of the dichroic signals was calculated. This calculation required the measurement of the current flowing through the cell during the deposition time and the use of Faraday's law.

### 5.3. RESULTS AND DISCUSSION

#### 5.3.1 Direct atomisation of Al, Cd, Co, Cr, Cu, Fe, Pb, Mg, Ni, Ag, and Zn.

The application of a background correction method is particularly important in sputtering cells at atmospheric pressure since background levels are normally high. In this work the atomic absorption of 11 elements (Al, Co, Cd, Cr, Cu, Fe, Pb, Mg, Ni, Ag, and Zn) was measured. In addition, the corresponding background absorption was determined to show its effect on the measurement of absorbance and the need of a method to correct for it. The measurement of the background absorption for a particular element was carried out by choosing an adjacent line of a second element while running the discharge cell under the same conditions used to measure the absorbance of the element of interest. The use of the adjacent line as the source of radiation required the use of a hollow-cathode lamp of the second element.

Table 5.1 shows the absorbance of each element and its corresponding background measurement. Under the conditions used,

**TABLE 5.1 Selected wavelengths for atomic absorption and background absorption measurements.**

Element (nm)	Measured absorbance†	Reported absorbance*	Background (nm)	Background absorbance†
Cd (324.8)	0.021±0.005	0.30	Zn (328.2)	0.000
Ni (341.5)	0.015±0.002	0.05	Fe (344.1)	0.000
Zn (213.4)	0.247±0.026	2.3	Cu (217.9)	0.000
Fe (248.3)	0.026±0.005	0.35	Be (249.4)	0.020±0.002
Mg (285.2)	0.070±0.004	0.70	Pb (283.2)	0.015±0.002
Ni (nichrome) (341.5)	0.025±0.002	0	Fe (344.1)	0.013±0.002
Al (396.1)	0.016±0.004	0	Pb (405.8)	0.025±0.003
Co (240.7)	0.011±0.002	0.35	Cu (244.2)	0.035±0.004
Cr (357.9)	0.013±0.002	0	Fe (358.1)	0.040±0.002
Pb (283.3)	0.007±0.002	0	Cu (282.4)	0.018±0.002

†The error is the standard deviation of three measurements.

\*Reported values refer to reference [32].

Cu (324.8 nm), Ni (341.5 nm), and Zn (213.9 nm) did not show background absorption when measured at the selected adjacent lines (Zn (328.2 nm), Fe (344.1 nm), and Cu (217.9 nm), respectively). A second set of elements, Fe (248.3 nm), Mg (285.2 nm), and Ni (nichrome) (341.5 nm), showed some background absorption when measured at the chosen adjacent lines (Be (249.4 nm), Pb (283.2 nm), and Fe (344.1 nm) respectively). A third set of elements showed stronger background absorption at the corresponding adjacent lines than at the line of the element. These elements were Al (396.1 nm), Co (240.7 nm), Cr (357.9 nm), and Pb (283.3 nm) whose background absorption was stronger at their adjacent lines (Pb (405.8 nm), Cu (244.2 nm), Fe (358.1 nm), and Cu (282.4 nm), respectively).

In order to explain the results described above (Table 5.1), it was necessary to investigate the nature of the background absorption. As described in section 1.3, background absorption may result from scattering of the radiation, absorption due to molecular bands, and spectral interference due to overlapping of atomic lines. Spectral interference due to overlapping of atomic lines is not considered here, since the atomic and background absorption are measured a few nanometres apart.

The background absorption due to scattering should remain essentially constant over a wavelength range of a few nanometres. Thus it cannot account for the high levels of background absorption measured at the adjacent line of the third set of elements. Moreover, the background absorption measurements of the first set

of elements indicated that scattering could not be detected under the present experimental conditions.

The experimental measurement of the total absorption in the vicinity of the lines of the elements of the third set by means of a continuous source and a narrow slitwidth revealed the presence of molecular bands. They can be assigned to  $N_2$ ,  $N_2^+$ ,  $O_2^+$  absorption bands [48]. The presence of absorption bands attributed to nitrogen and oxygen species suggested traces of air inside the discharge cell. As expected, increasing the flow of helium to the cell caused the absorption bands to become weaker. Thus one way to get rid of the absorption bands would be to increase the helium flow or tighten the seals of the cell. In each case, the absorption band was stronger at the adjacent line than at the line of the element of interest, which provides an explanation of the results from the third set of elements (Table 5.1).

The Zeeman-corrected instrument used to obtain the results shown below was considered to offer a better approach to the elimination of background absorption. The Zeeman background correction method was applied using the instrument described in section 5.2.1. The effect of the discharge current and of the magnetic field strength on the dichroic measurements of Cd (326.1 nm), Cu (324.8 nm), Ni (341.5 nm), Ni (nichrome, 341.5 nm), Ag (328.1 nm) are presented. A blank was made by applying the maximum attainable discharge current and field strength to the discharge cell and using an adjacent line as a source of radiation

(Table 5.2). Failure by the blank to produce a dichroic signal in each case proved the effectiveness of the background-correction method. The other elements studied failed to show a dichroic signal. The possible reasons will be discussed below.

The atom population in the discharge cell is sustained by sputtering or thermal vaporisation of the atoms of the electrode. The contribution of each of the processes to the production of atoms depends on the discharge cell operating conditions. Sputtering requires collisions of particles with enough kinetic energy to break individual atomic bonds. Thermal vaporisation requires the transfer of collisional energy to the electrode to raise the average lattice energy. The atoms with energy equal to or greater than the enthalpy of vaporisation  $\Delta H_{\text{vap}}$  will be vaporised. In this study (Figure 5.3), examples of atomisation due to both processes were identified.

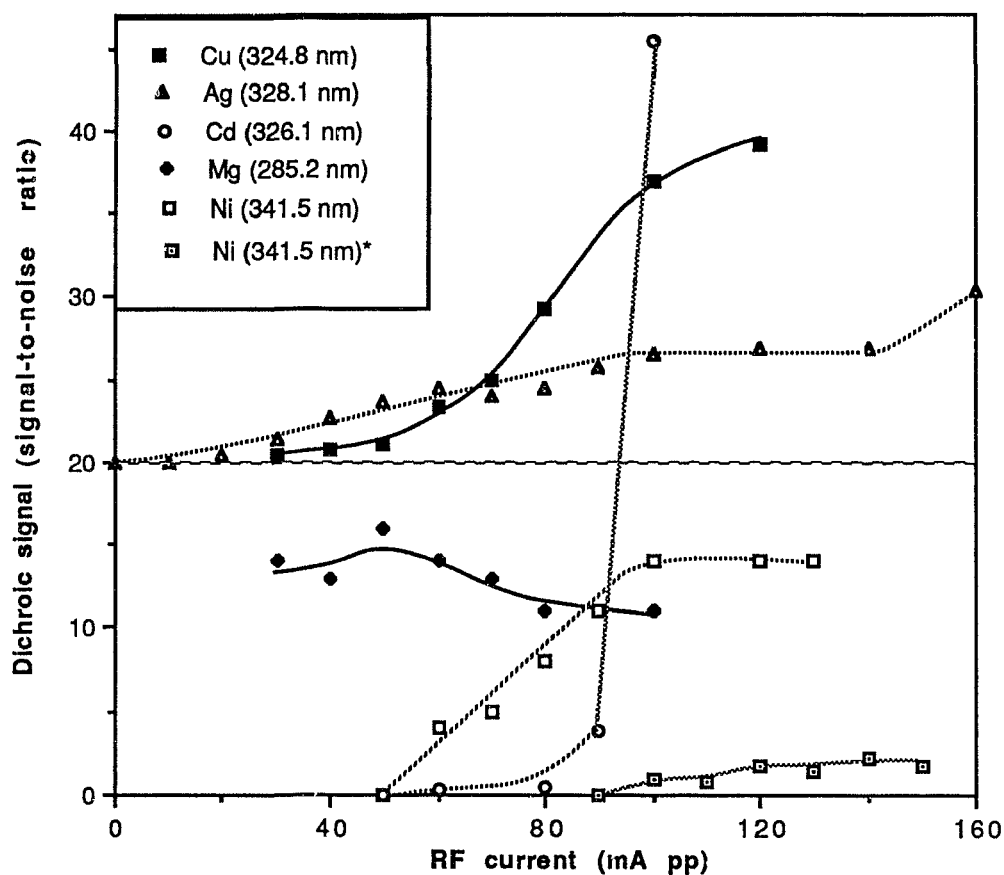
The results shown in Figure 5.3 indicate that sputtering is the dominant process at low discharge currents. A simple description would indicate that the number of sputtered atoms will be proportional to the number of collisions, which is in turn also proportional to the number of charge carriers (i.e. the electric current). Given low atomic absorption levels, the dichroic signal of the element is expected to increase linearly with the discharge current until thermal vaporisation becomes important in maintaining the atom population. In Figure 5.3 dichroic signals associated with sputtering can be identified for the following elements in the

**TABLE 5.2. Elements that showed a dichroic signal.**

Atomised material		Blank*	
Element line (nm)		Adjacent line (nm)	
Cd	326.1	Cu	324.8
Cu	324.8	Zn	328.2
Mg	285.2	Pb	283.2
Ni	341.5	Fe	344.1
Ni(nichrome)	341.5	Fe	344.1
Ag	328.1	Zn	328.2

\* The blank was made by choosing an adjacent line of a different element as the source of radiation while the discharge cell was operated under the same conditions.

**FIGURE 5.3** Dichroic signal of Cu, Ag, Cd, Mg, and Ni versus RF current.



Nichrome wire was the source of Ni in Ni (341.5 nm)\*. Cu and Ag have an offset of +20 arbitrary units; Cd curve is reduced 15 times. The field strength was 0.520 Tesla; the lamp frequency 1.0 kHz; the RF frequency 95 kHz.

indicated current ranges: Cd (50-80 mA pp), Cu (30-70 mA pp), Ni (50-100 mA pp), Ni (nichrome) (90-150 mA pp), and Ag (0-60 mA pp).

When thermal vaporisation is the dominant atomisation process, the slope of the curve of the dichroic signal versus discharge current increases, almost showing an exponential behaviour. The Cd curve (Figure 5.3) clearly shows that behaviour. Thermal vaporisation starts to contribute to the production of Cd atoms at discharge currents above 90 mA pp. The fact that Cd has the lowest enthalpy of vaporisation ( $\Delta H_{\text{vap}} = 23.9$  kCal/mole) of all the elements tested explains this difference in behaviour with respect to the other elements. Mg and Pb have the second and third lowest enthalpy of vaporisation ( $\Delta H_{\text{vap}} = 31.5$  kCal/mole and  $\Delta H_{\text{vap}} = 42.5$  kCal/mole respectively). However, no indication of thermal vaporisation was observed in the Mg curve (Figure 5.3), and Pb did not show any dichroic signal when metallic lead was used.

The Ni and Mg curves show a plateau in Figure 5.3. In the case of Ni, it occurs at high currents (100-130 mA pp), above of the sputtering region (50-100 mA pp). The Mg curve is basically constant in the 30-100 mA pp range. The plateau in the Ni and Mg curves was not the result of electronic or optical saturation of the instrument. This was confirmed by producing a dichroic signal with a quartz plate to check the performance of the response of the system in a much wider range. Thus, the plateau must be related to the performance of the discharge cell. At the point where the

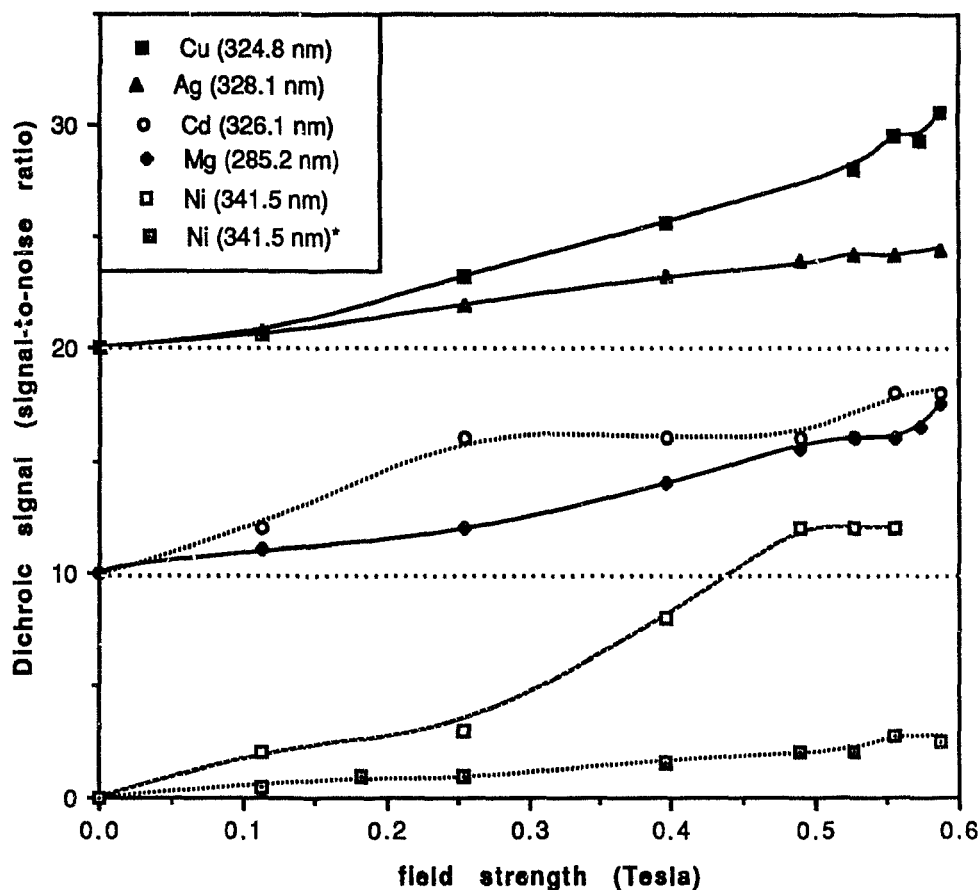
population of sputtered atoms does not increase any further as the discharge current is increased (30 mA pp or below for Mg and 100 mA pp for Ni), an alternative process must occur. Whatever mechanism causes the plateau, the point at which it appears will also depend on the material being atomised, as noted in the results with Ni metal and Nichrome.

The effect of field strength on the dichroic signal of the different elements can be seen in Figure 5.4. Since the dichroic signal depends on factors such as the Zeeman pattern of the transition, the characteristics of the source profile and the characteristics of the absorption profile, each curve described above shows a different behaviour.

In general, the long-term stability of the signal of each element was poor. The fast destruction of the electrode was found to be one of the reasons for instability in the Cr, Mg, and Pb measurements. It changed the size of the electrode, and consequently the throughput of radiation (since the beam of radiation was focused on the electrode) and the length of the column of the discharge.

Elements such as Al, Co, Cr, Fe, and Pb which did not show a dichroic signal clearly indicate that the discharge cell is not effective for producing an atom population of the element, or else that the density of the atomic species is below the detection limit of this instrument. A stable oxide layer formed on the surface of

**FIGURE 5.4 Dichroic signal of Cu, Ag, Cd, Mg, and Ni versus field strength.**



Nichrome wire was atomised in Ni (341.5 nm)\*. Cu, Ag, Cd, Mg, Ni, and Ni(nichrome) have an offset of +20, -20, +10, +10, 0, and 0 respectively. The discharge current used was 120, 30, 70, 100, 150, and 150 mA pp respectively. The lamp frequency was 1.0 kHz; RF frequency 95 kHz.

the material stops the sputtering of Al, Cr, and Pb atoms [32]. The low absorbance of Co and Fe (Table 5.1) suggests that the density of their atoms in the discharge is too low to detect their dichroic signal.

Zn also showed absorbance (Table 5.1) and did not show a dichroic signal. The 213.9 nm Zn resonance line is out of the transmission range of a calcite polariser prism (215 nm - 2.3  $\mu\text{m}$ ), dramatically reducing the sensitivity of the instrument at that wavelength. Use of Zn lines other than the main resonance line (such as the 307.2, 334.5, and 636.2 nm, which were also investigated) may not be appropriate because of the low oscillator strength of the corresponding electronic transition [12].

To conclude, the discharge cell described here has the following advantages: it is operated at atmospheric pressure; it can be used to obtain background-free signals of elements such as Cd, Cu, Mg, Ni, and Ag; solid samples are used directly; and, since the range in which sputtering is responsible for the atomisation can be chosen, there is no need to control and keep a high temperature in the cell to vaporise the element, as in the case of a furnace. The main disadvantages are a short pathlength, a low atom density, and the difficulty of sputtering elements such as Al, Pb, and Cr under the conditions described here. The technique requires further investigation before it becomes viable. Improvements could be made by use of better cooling systems to reduce the effect of thermal vaporisation, higher currents to obtain a better dynamic range,

pulsed discharges to eliminate background emission, and different fill gases.

### 5.3.2 Deposition of silver.

The objective in this part of the study was to combine electrodeposition with the instrument described in section 5.2.1 and to determine the detection limit of that instrument for silver using the 328.1 nm Ag line. The amount of silver deposited onto the electrode of the discharge cell was estimated on the basis of the concentration of cupric ions released into solution as the result of the redox reaction between metallic copper and silver ions. The influence of the length of the deposition time and the effect of stirring the solution on the detection limit were also investigated.

In order to improve the reproducibility of the signal and reduce the sources of error, the same electrode was used throughout each experiment, and the same position of the electrode in the discharge cell was maintained.

For small quantities of silver deposited on the electrode, (i.e. low original concentration and/or short time of deposition), the dichroic signal of silver decayed exponentially with atomisation time. The peak value was adopted to represent the dichroic signal. Although it is believed that the integration of the signal with respect to time would have represented better the total amount of material being atomised, this approach was not carried out because some signals took an excessive time to decay to zero.

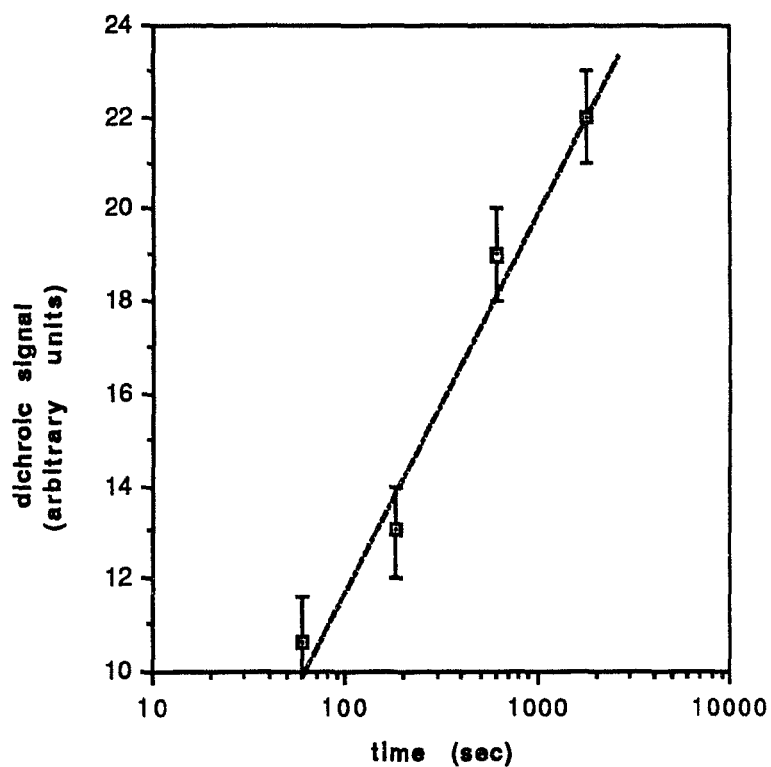
The dichroic signal for silver (Figure 5.5) increased as the time of deposition increased. The increment was not linear with respect to the time of immersion, but it seemed linear with respect to its logarithm. According to the model proposed by Sioda [49], an equilibrium is eventually reached and lengthening the immersion time does not increase the deposition of silver; as a consequence, the associated dichroic signal should reach a plateau. However, Figure 5.5 does not indicate that the signal has reached a plateau for the longest immersion time; thus the deposition process was still far from equilibrium and, as a consequence, lengthening the deposition time should improve the detection limit.

The dichroic signal of silver decreased as the concentration of silver ions in solution decreased (Figure 5.6). The estimated detection limit was  $1.00 \times 10^{-4}$  M (signal-to-noise ratio equal to 2) when the electrode was immersed 1 mm for 300 seconds.

In order to improve the detection limit of the instrument, the electrode was immersed in the silver solution to a depth of 3 mm instead of 1 mm, for 180 seconds. This had the effect of reducing the detection limit to  $1.00 \times 10^{-5}$  M. However further increases did not enhance the signal. Thus 3 mm was chosen as the depth for carrying out the tests described below.

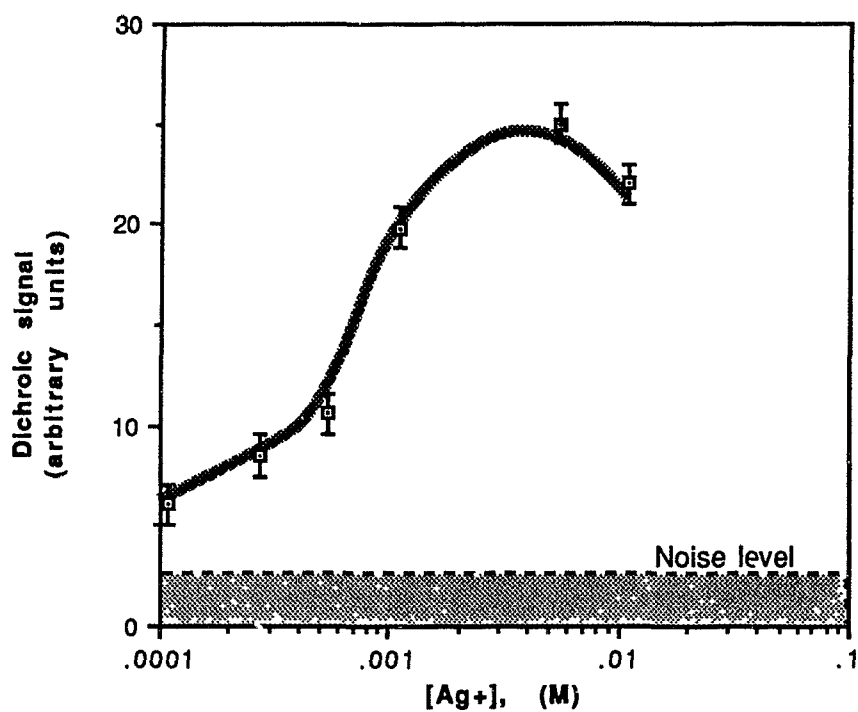
Stirring the solution during the deposition speeds up the deposition rate, and as a consequence, equilibrium is approached faster. For a given concentration and deposition time the dichroic

**FIGURE 5.5** Dependence of the dichroic signal of the 328.1 nm silver line on the time of deposition.



Silver was deposited on a copper electrode from a 0.0010 M silver ion solution. The RF current was 140 mA pp. The lamp frequency was 1.0 kHz; RF frequency 95 kHz; field strength 0.520 Tesla.

**FIGURE 5.6** Dependence of the dichroic signal of the 328.1 nm silver line on the concentration of the solution used to deposit the metallic silver.



The deposition was carried out for 300 seconds. The dichroic signal was obtained using the following conditions: RF current 140 mA pp; RF frequency 95 kHz; lamp frequency 1.0 kHz; field strength 0.520 Tesla.

signal is enhanced. When the solution was stirred and the rest of conditions were kept constant (electrode immersed to a depth of 3 mm for 180 seconds in a  $1.00 \times 10^{-5}$  M silver solution), the signal-to-noise ratio showed a five-fold improvement.

As mentioned above, the detection limit may be improved by lengthening the time of immersion. A signal-to-noise ratio of 7.5 was obtained when the electrode was immersed in a  $1.00 \times 10^{-8}$  M silver solution for 3600 seconds (1 hour). The solution was stirred at the same rate and the electrode was immersed to the same depth as above. If linearity is assumed at low concentrations, the detection limit (signal-to-noise ratio equal to 2) is  $2.7 \times 10^{-9}$  M (0.29 ppb).

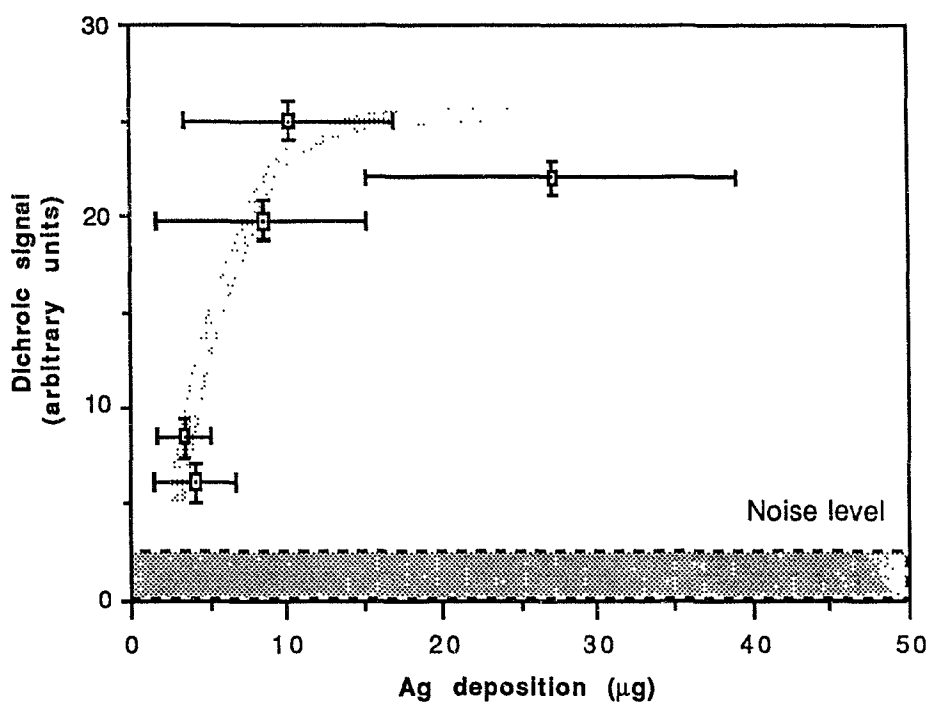
It can be concluded that stirring the solution and lengthening the immersion time lowers the detection limit. In this case, the detection limit of silver is  $2.7 \times 10^{-9}$  M (0.29 ppb) obtained when the electrode is immersed 3 mm for one hour in a stirred solution. Silver detection limits reported in the literature are as low as 0.0024 ppb when an electrolytic reduction was combined with a wire loop atomiser [40].

The detection limit may be improved further by increasing the sample volume and reducing the concentration of oxygen in solution (i.e. by bubbling nitrogen into the solution). The deposition time can be shortened by increasing the speed of stirring.

The amount of silver deposited on the electrode was indirectly determined by conventional atomic absorption analysis of the copper ions released into solution. The relation between the Ag (328.1 nm) dichroic signal and weight of silver deposited on the electrode is shown in Figure 5.7. The different amounts of silver deposited on the electrode were obtained by immersing the electrode in different concentrations of silver ions for a fixed time of 300 seconds.

The absolute detection limit is about 5  $\mu\text{g}$  of silver (signal-to-noise ratio equal to 2), based on the results shown in Figure 5.7. This calculation has the inherent problem that the uncertainty in the measurement of the deposited amount of silver is high. However, based on the minimum detectable concentration ( $2.7 \times 10^{-9}$  M) and the 10-ml volume used in this study, it is found that the maximum amount that could be present is only 3 ng. The reason for this difference may be attributed to traces of nitric acid which may have contributed to the dissolution of the copper electrode, causing overestimation of the amount of silver shown in Figure 5.7. Since the absolute detection limit is a function of the Zeeman-corrected instrument (as opposed to the detection limit of the ions in solution, which depends upon the conditions used in the deposition step and the Zeeman-corrected instrument), improvements can be achieved only by designing an instrument of higher sensitivity. A discharge cell which provides better atomic absorption levels by an increased pathlength or higher density of atoms is required.

**FIGURE 5.7** Dichroic signal of silver versus the amount of silver deposited on the electrode.



The amount of silver deposited on the electrode was calculated from the copper released into solution which was determined by conventional atomic absorption. Different amounts of silver were obtained by immersing the electrode in silver solutions of different concentrations for 300 seconds. The dichroic signal was obtained using the following conditions: RF current 140 mA pp; RF frequency 95 kHz; lamp frequency 1.0 kHz; field strength 0.520 Tesla. Error bars are the standard deviation of three repetitions.

### 5.3.3 Electrodeposition of lead.

The electrolysis of solutions of lead(II) ions produced a black deposit on the cathode. This material was susceptible to atomisation by the discharge, and the associated dichroic signal of lead could be detected. In an earlier part of this study (section 5.3.1), the oxide layer on the surface of a metallic lead electrode prevented it from producing a vapour of lead atoms, and as a consequence no dichroic signal could be detected.

In order to improve reproducibility and reduce error, the same cathode was used, the relative position of anode and cathode was checked prior to the electrodeposition, a constant voltage was applied across the cell, the electrodes were immersed to a fixed depth, the solution was stirred at a constant rate, and the cathode carrying the deposit was placed in the same position in the discharge cell.

Since this is the first time that the dichroic signal of the 283.3 nm Pb line has been detected using this instrument, a description of its dependence on the RF current and the field strength is presented. In order to deposit enough lead to carry out the measurements, electrolysis of a  $1 \times 10^{-3}$  M lead (II) ion solution was carried out for 180 seconds, applying a voltage of 1.50 V across the electrodes.

The signal increased almost linearly in the range

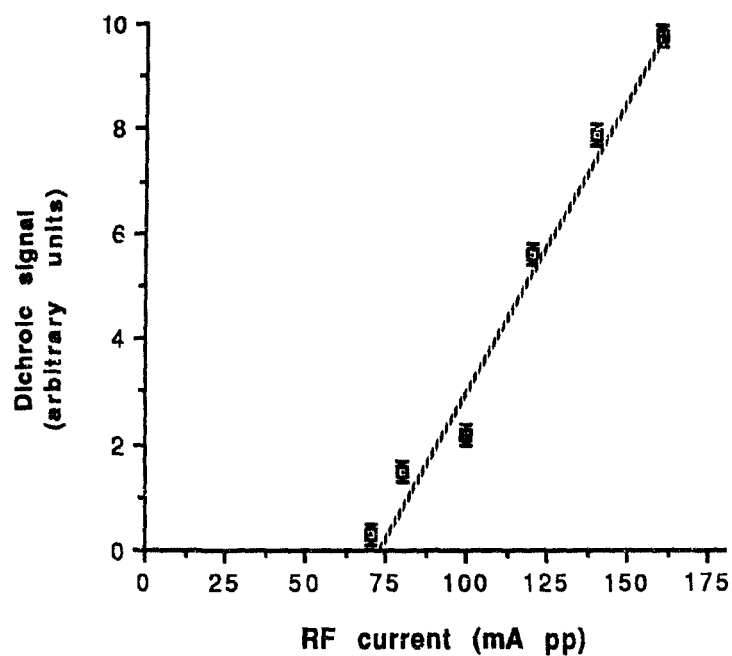
70 -160 mA pp as the RF current increased (Figure 5.8). A curve expressing the relation between the dichroic signal of the 283.3 nm Pb line and field strength is shown in Figure 5.9.

The dichroic signal of lead is plotted against deposition time in Figure 5.10. The dichroic signal increases almost linearly with respect to the logarithm of time from about 1900 seconds to 15000 seconds and gives no indication of having reached an equilibrium.

The amount of lead deposited on the copper sheet can be estimated from the measurement of the net current (difference of the currents measured using the lead (II) ion solution and a blank) through the electrolytic cell. A detection limit of 12  $\mu\text{g}$  of lead (signal-to-noise ratio equal to 2) was calculated from the total charge used in the electrodeposition (0.0108 Coulombs; 12  $\mu\text{A}$  flowing through the cell during 15 minutes). A voltage of 1.5 V was applied across the cell filled with a solution which original concentration of lead (II) was  $1.0 \times 10^{-5}$  M (2.1 ppm). Newton reported a detection limit of  $1 \times 10^{-4}$  ppm of lead (II) obtained by combining electrolytic reduction with a wire loop atomiser [40]. Study on lowering the minimum detectable concentration was not carried beyond this point.

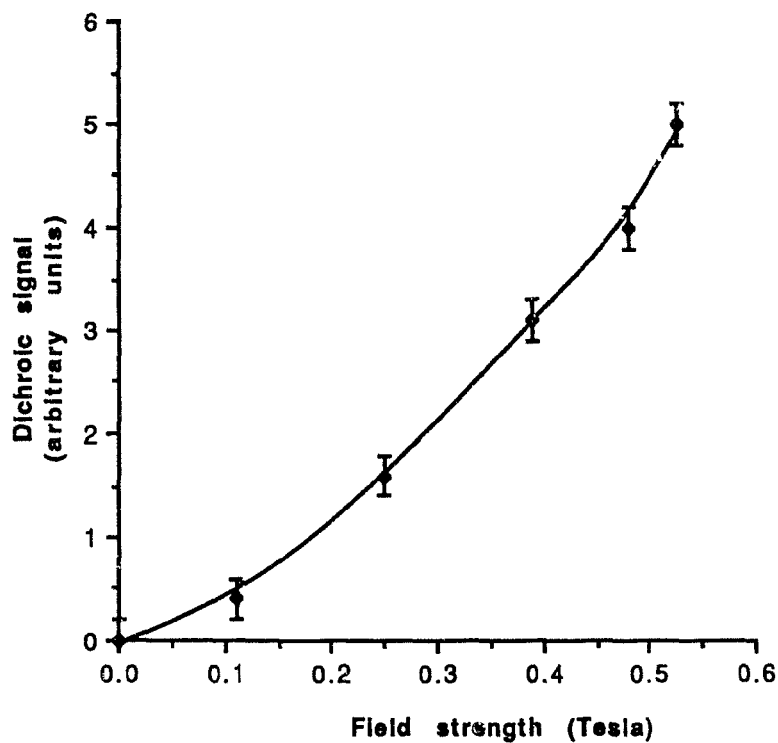
The electrolytic cell used in this work did not have separate compartments for the anode and the cathode. Therefore, the copper ions released on the anode could migrate and be redeposited onto the

**FIGURE 5.8** Dependence of the dichroic signal of the 283.3 nm lead line on the RF current.



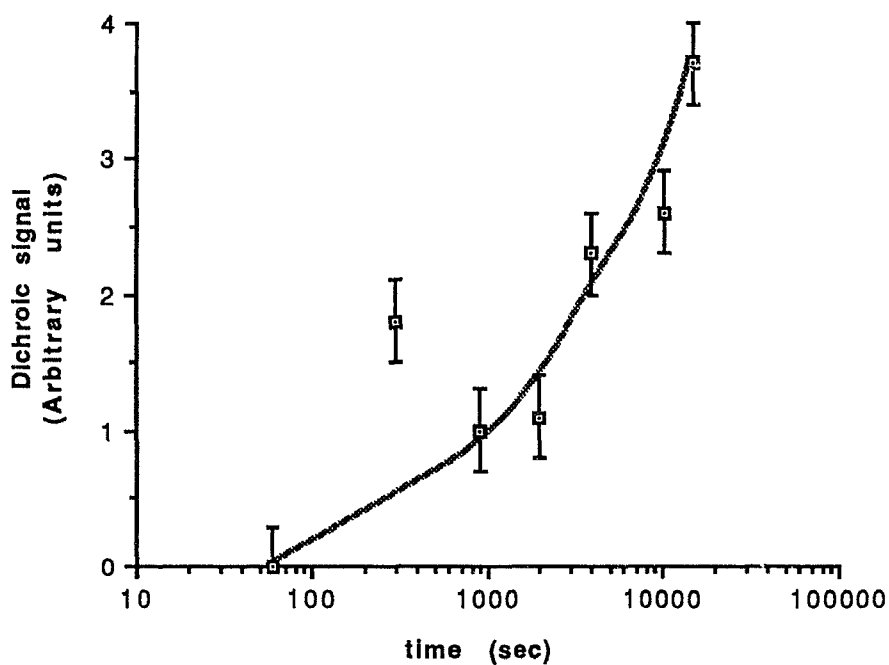
Lead was electrodeposited on a copper electrode from a 0.0010 M lead (II) solution for 180 seconds applying 1.50 V across the electrodes. The dichroic signal was obtained using the following conditions: RF frequency 95 kHz; lamp frequency 1.0 kHz; field strength 0.520 Tesla.

**FIGURE 5.9** Dependence of the dichroic signal of the 283.3 nm lead line on the field strength.



Lead was electrodeposited on a copper electrode from a 0.0010 M lead (II) solution for 180 seconds applying 1.50 V across the cell. The dichroic signal was obtained using the following conditions: RF current 150 mA pp; RF frequency 95 kHz; lamp frequency 1.0 kHz.

**FIGURE 5.10** Dependence of the dichroic signal of the 283.3 nm lead line on the length of electrodeposition.



Lead was electrodeposited on a copper electrode from a  $1.0 \times 10^{-5}$  M lead (II) solution applying 1.50 V across the cell. The dichroic signal was obtained using the following conditions: RF current 150 mA pp; RF frequency 95 kHz; lamp frequency 1.0 kHz; magnetic field 0.52 Tesla.

cathode. However, the measurement of the net current took that fact into account since the solution and blank had the same charge carriers, except for the lead ions. The use of this cell also suggested that different species can be deposited simultaneously, and subsequently determined by the Zeeman background-corrected instrument.

In conclusion, the Zeeman background-corrected discharge cell at atmospheric pressure can be combined with the electrodeposition technique as an alternative to analyse materials in solution such as silver and lead. Electrolytic and autogalvanic preconcentration appear to be very promising ways of lowering the detection limits of the instrument.

## 6. GENERAL CONCLUSIONS.

Harmonic analysis can be used to extract information about profiles experiencing an alternating magnetic field. Two configurations were explored in the course of this study: the Faraday configuration and the Voigt configuration.

### 6.1. Harmonic analysis using the Faraday configuration.

Using the Faraday configuration, the application of the field to a hollow-cathode lamp provided harmonics associated with the emission and self-absorption profiles. The results showed that the presence of self-absorption is a requirement for detection of the first harmonic. For instance, the first harmonic of the 377.7 nm Ne line was hardly detected. This transition has a low population in the lower state; thus the associated self absorption is also negligible.

When self-absorption is caused by atoms sputtered from the cathode, as in the case of Li (670.8 nm) and Mg (285.2 nm), the effects are poorly controlled, as reflected in the harmonic measurements.

### 6.2 Harmonic analysis using the Voigt configuration.

Using the Voigt configuration, the application of combined a.c. and d.c. fields provided selective harmonics associated with the absorption profiles of lines showing overlap. The three lowest harmonics  $b(0)$ ,  $a(1)$ , and  $b(2)$  contributed the most to the signal.

They provided an effective way to distinguish between the doublets of the lithium isotopes at 670.8 nm and the spectral overlap of Pt and Fe at 271.9 nm. This technique could be applied to flag a warning if the amplitude of the harmonics (or their ratios) are outside an expected range for a known analyte. A related application could involve the quantification of isotopic mixtures without the need for several isotopic-enriched sources.

6.3 Zeeman background correction applied to discharge cells filled with helium at atmospheric pressure.

A comparison of the application of the Voigt and Faraday configurations to perform Zeeman background correction in a pulsed discharge cell filled with helium at atmospheric pressure was made. In terms of instrumental design, the Voigt configuration was favoured. It did not require either a coil wound on the cell, and subject to overheating, or a pulsed magnetic field. The two configurations showed an equal capability to correct for background absorption: the Faraday configuration eliminated the background absorption associated with the 324.8 nm Cu line, and the Voigt configuration eliminated the background absorption associated with the 670.8 nm Li doublet. A pulsed discharge cell was used to control overheating of the cell, and the coil wound around it, and provided correction for background emission. It presented the inconvenience of requiring specific adjustment of the duty cycle for each element.

A continuous discharge cell filled with helium at atmospheric pressure was successfully used to atomise six elements (Cd, Cu, Mg, Ni, Pb, and Ag). The Voigt configuration provided an effective background correction for the atomic lines of these elements. The method was particularly effective in the cases of Mg (285.2 nm), Ni (341.5 nm), and Pb (283.2 nm), which showed strong background absorption at a selected adjacent line. The method was less successful in giving the Zeeman-corrected signals of Al, Co, Cr, Fe, Zn, and metallic Pb. A stable oxide layer impeded the atomisation of Al, Cr, and metallic Pb; the signals of Co and Fe could not be detected because of their low densities in the cell; Zn (213.4 nm) could only be explored at its resonant transition, which was outside the optical range of the system.

Improvements in instrument design to control background emission, to eliminate thermal vaporisation of the element, and to expand the range of the discharge currents are required before the technique becomes viable. The use of discharge cells at atmospheric pressure combined with Zeeman background correction has a great potential for direct atomisation of solid samples.

The combined use of electrodeposition of elements such as Pb and Ag onto the electrode of the discharge was also found to be feasible. In addition to providing an indirect indication of the detection limit of the system, it proved to be applicable to the analysis of solutions without the need for an elaborated sample preparation procedure.

## APPENDIX A. Jones calculus.

This mathematical treatment permits prediction of the components of the electric vector and hence the intensity of polarised light after interacting with an optical system.

Each optical component of the optical system is represented by a 2X2 matrix which describes a linear transformation on the electric vector of the incident light. In general, each of the elements of the matrix is a complex number. This appendix shows the basic application of the Jones calculus to the optical configurations used throughout this study. A more comprehensive description is presented by Kankare and Stephens [50] and the original publications by Jones [51-52].

### A.1 Theory.

A monochromatic plane wave can be described by its electric vector. In a right-handed co-ordinate system, where the direction of propagation is assumed to be the z axis, the electric vector  $\mathbf{E}$  oscillates perpendicularly to the z axis; it has components  $E_x$  and  $E_y$ . The electric vector is described as:

$$\mathbf{E} = \exp(-i\Psi_1) E_x + \exp(-i\Psi_2) E_y \quad (1A)$$

where

$$\Psi = \omega(t-nz/c); \quad (2A)$$

and  $\omega$  is the angular frequency,  $n$  is the index of refraction of the medium,  $c$  is the velocity of light and  $t$  is time.

In this study the relative (not the absolute) phase of the electric vectors is important. Putting  $\Psi_2 = \Psi_1 + \phi$  where  $\phi$  is the relative phase substitution in equation (1) yields:

$$\mathbf{E} = \exp(-i\Psi_1) [\mathbf{E}_x + \exp(-i\phi) \mathbf{E}_y] \quad (3A)$$

The relative phase of  $\mathbf{E}_y$  and  $\mathbf{E}_x$  indicates the polarisation of the radiation. When  $|\phi| = \frac{1}{2}\pi, \frac{3}{2}\pi, \dots$ , the plane wave is said to show circular polarisation; when  $|\phi| = 0, \pi, 2\pi, \dots$ , it is said to show linear polarisation; plane waves with other  $\phi$  values show elliptical polarisation.

The intensity of the radiation is proportional to the product of the electric vector  $\mathbf{E}$  and its conjugate  $\mathbf{E}^*$  [50]; thus the intensity  $I$  can be calculated as:

$$I = \mathbf{E} \cdot \mathbf{E}^* = \mathbf{E}_x \cdot \mathbf{E}_x^* + \mathbf{E}_y \cdot \mathbf{E}_y^* \quad (4A)$$

In general,  $I$ ,  $\mathbf{E}_x$  and  $\mathbf{E}_y$  are functions of the frequency and can be evaluated over the frequency bandwidth of the instrument (see section 1.1.4). In the rest of this appendix, the frequency dependence will be implicit.

Note that  $\exp(-i\Psi_1)$  and  $\exp(-i\phi)$  (equation (3A)) are cancelled when  $I$  is calculated in equation (4A); in order to simplify the matrix representation that follows, they will be omitted. Hence the electric vector is represented as

$$\mathbf{E} = \mathbf{E}_x + \mathbf{E}_y \quad (5A)$$

or, in matrix notation,

$$\mathbf{E} = \begin{bmatrix} E_x \\ E_y \end{bmatrix} \quad (6A)$$

The effect of an optical component on the electric vector of the plane wave is then described by a 2X2 matrix  $\mathbf{J}$  which connects the electric vector of the emerging radiation  $\mathbf{E}_{out}$  with that of the incident radiation  $\mathbf{E}_{in}$ ; thus

$$\mathbf{E}_{out} = \mathbf{J} \mathbf{E}_{in} \quad (7A)$$

where

$$\mathbf{E}_{out} = \begin{bmatrix} E_{x,out} \\ E_{y,out} \end{bmatrix}; \quad \mathbf{E}_{in} = \begin{bmatrix} E_{x,in} \\ E_{y,in} \end{bmatrix}; \quad \text{and } \mathbf{J} = \begin{bmatrix} J_{11} & J_{21} \\ J_{12} & J_{22} \end{bmatrix}$$

When radiation travels through  $q$  optical elements in sequence, each of them characterised by a Jones matrix  $\mathbf{J}_1, \mathbf{J}_2, \mathbf{J}_3, \dots, \mathbf{J}_q$ , then

$$\mathbf{E}_{out,1} = \mathbf{J}_1 \mathbf{E}_{in,1}$$

$$\mathbf{E}_{out,2} = \mathbf{J}_2 \mathbf{E}_{in,2} = \mathbf{J}_2 \mathbf{E}_{out,1} = \mathbf{J}_2 \mathbf{J}_1 \mathbf{E}_{in,1}$$

$$\mathbf{E}_{out,q} = \mathbf{J}_q \mathbf{J}_{q-1} \dots \mathbf{J}_2 \mathbf{J}_1 \mathbf{E}_{in,1} \quad (8A)$$

where  $\mathbf{J} = \mathbf{J}_q \mathbf{J}_{q-1} \dots \mathbf{J}_2 \mathbf{J}_1$  is the Jones matrix of the system.

A description of the matrices of optical components used in this work is presented below. It also includes transformation matrices which are needed to rotate coordinates in space or to exchange the basis set of the co-ordinate system. The deduction of such matrices is presented by Kankare and Stephens [50] and Gerrard and Burch [53].

## A.2 Matrix representation of common optical components.

Ideal polarisers are represented as  $\mathbf{P}_x$  and  $\mathbf{P}_y$  and only transmit the radiation with its electric vector aligned with the  $x$  and  $y$  axes respectively. Their Jones matrices are as follows:

$$\mathbf{P}_x = \begin{bmatrix} 1 & 0 \\ 0 & 0 \end{bmatrix} \quad (9A)$$

$$\mathbf{P}_y = \begin{bmatrix} 0 & 0 \\ 0 & 1 \end{bmatrix} \quad (10A)$$

Isotropic absorbers attenuate the magnitude of both components of the electric vector to the same extent. Their Jones matrix is:

$$\mathbf{K} = \begin{bmatrix} \exp(-K N \ell/2) & 0 \\ 0 & \exp(-K N \ell/2) \end{bmatrix} = \exp(-K N \ell/2) \mathbf{I} \quad (11A)$$

where  $K$  is the absorption coefficient,  $N$  the density of absorbing species,  $\ell$  is the pathlength, and  $\mathbf{I}$  is the unit matrix. The explicit dependence of  $K$  on the frequency is presented in section 1.1.4.

Dichroism is shown by anisotropic absorbers. They attenuate the magnitude of the components of the electric vector to a different extent. If a transverse magnetic field is used (Voigt configuration),  $\pi$  and  $\sigma$  components are present and assigned to the  $x$  and  $y$  axes respectively. Their Jones matrix is:

$$\mathbf{V}_{di} = \begin{bmatrix} \exp(-K_\pi N \ell/2) & 0 \\ 0 & \exp(-K_\sigma N \ell/2) \end{bmatrix} \quad (12A)$$

where the meaning of the variables is the same as for the isotropic absorbers, equation (11A).

Birefringence is shown by anisotropic retarders. They change the speeds of the components of an electric vector to different extents, for the index of refraction  $n$  is different on the  $x$  and  $y$  axes. In the presence of a transverse magnetic field (Voigt configuration)  $\pi$  and  $\sigma$  components are present. Their Jones matrix is:

$$\mathbf{V}_{bi} = \begin{bmatrix} \exp(i n_{\pi} l / 2) & 0 \\ 0 & \exp(i n_{\sigma} l / 2) \end{bmatrix} \quad (13A)$$

Dichroism and birefringence, described above, are related phenomena. An explicit relation, obtained by means of the Kramers-Kronig transform, is necessary to evaluate the dependence of the system on the line profile involved [54]. Both effects can be combined in a single matrix using a complex index of refraction  $\tilde{n} = n' + i n''$  where  $n'$  is related to the index of refraction of the medium and  $n'' = KN / 2$ . The corresponding Jones matrix is:

$$\mathbf{V} = \begin{bmatrix} \exp(i \tilde{n}_{\pi} l) & 0 \\ 0 & \exp(i \tilde{n}_{\sigma} l) \end{bmatrix} \quad (14A)$$

The results of equations (13A) and (14A) are also applicable to the Faraday configuration (directions of propagation of the wave

front and the magnetic field are the same). The subscripts of the complex index of refraction are changed to the  $\sigma_+$  and  $\sigma_-$  components, the vector basis of the circular polarisation. The corresponding Jones matrix is:

$$\mathbf{F} = \begin{bmatrix} \exp(i n_{\sigma_+} l) & 0 \\ 0 & \exp(i n_{\sigma_-} l) \end{bmatrix} \quad (15A)$$

Photoelastic modulators retard the electric vectors of the radiation to the same extent, but in opposite directions. These devices produce an oscillating retardance of the form  $\delta = \delta^0 \sin \omega_p t$  where  $\omega_p$  is the angular frequency of the photoelastic modulator. The associated Jones matrix is:

$$\mathbf{J}_{pem} = \begin{bmatrix} \exp(-i \delta) & 0 \\ 0 & \exp(i \delta) \end{bmatrix} \quad (16A)$$

Rotation matrices are used when the electric vectors have to be described in the frame of reference of a particular optical component whose x and y axes are rotated by an angle  $\Theta$ . After the interaction with the rotated optical component, the inverse rotation matrix transforms the electric vector to the original frame of reference. The rotation matrix and the inverse rotation matrix are represented by:

$$\mathbf{R}(\Theta) = \begin{bmatrix} \cos \Theta & \sin \Theta \\ -\sin \Theta & \cos \Theta \end{bmatrix} \quad (17A)$$

$$\mathbf{R}^{-1}(\Theta) = \begin{bmatrix} \cos \Theta & -\sin \Theta \\ \sin \Theta & \cos \Theta \end{bmatrix} \quad (18A)$$

respectively.

When a description of an electric vector in the basis set of circular co-ordinates is required, as when predicting the interaction in a Faraday cell, a transformation matrix  $\mathbf{U}$  is required. The matrix  $\mathbf{U}^{-1}$  transforms the circular co-ordinates back the original frame of reference:

$$\mathbf{U} = \frac{1+i}{2} \begin{bmatrix} 1 & -i \\ -i & 1 \end{bmatrix} \quad (19A)$$

$$\mathbf{U}^{-1} = \frac{1-i}{2} \begin{bmatrix} 1 & i \\ i & 1 \end{bmatrix} \quad (20A)$$

A.3 Prediction of the performance of the optical systems by means of Jones calculus.

A.3.1 System No 1: d.c. Zeeman scanning.

The optical configuration is shown in Figure 3.4. The Jones matrix of this system  $\mathbf{J}$  is the product of the matrices of a polariser  $\mathbf{P}_y$  and a Voigt cell  $\mathbf{V}$ , such as

$$\mathbf{J} = \mathbf{P}_y \mathbf{V} \quad (21A)$$

or, in the matrix form,

$$\mathbf{J} = \begin{bmatrix} 0 & 0 \\ 0 & 1 \end{bmatrix} \begin{bmatrix} \exp(i \tilde{n}_\pi l) & 0 \\ 0 & \exp(i \tilde{n}_\sigma l) \end{bmatrix} \quad (22A)$$

which leads to:

$$\mathbf{J} = \begin{bmatrix} 0 & 0 \\ 0 & \exp(i \tilde{n}_\sigma l) \end{bmatrix} \quad (23A)$$

According to equations (7A) and (8A), the electric vectors of the monochromatic radiation leaving the polariser should be:

$$\mathbf{E}_{y,\text{out}} = \mathbf{E}_{y,\text{in}} \exp(i \tilde{n}_\sigma l) \quad (24A)$$

and

$$\mathbf{E}_x = 0 \quad (25A)$$

From equation (4A), the intensity is

$$I = \mathbf{E} \cdot \mathbf{E}^* = E_y^2 = I_{y,in} \exp(i n_{\sigma}'' L) \quad (26A)$$

or

$$I = I_{y,in} \exp(-K_{\sigma} N L) \quad (27A)$$

where the variables have the same meaning as in equation (14A).

The difference in the signal of the absorbance in the presence ( $S_{H \neq 0}$ ) and absence ( $S_{H=0}$ ) of a d.c. magnetic field can be predicted, based on equation (27A), to be:

$$S_{H \neq 0} - S_{H=0} = 0.43 ((K_{\sigma} - K) N L) \quad (28A)$$

This equation represents the response of the system used to obtain the results in Figures 3.5 and 3.8.

### A.3.2 System No. 2: field-on-atomiser, Voigt configuration.

This optical configuration was used in Chapters 3,4 and 5 as shown in Figures 3.1, 4.6 and 5.1. The Jones matrix of this system is:

$$\mathbf{J} = \mathbf{P}_x \mathbf{R}^{-1}(\Theta) \mathbf{J}_{pem} \mathbf{R}(\Theta) \mathbf{V} \quad (29A)$$

or, in matrix form,

$$\mathbf{J} = \begin{bmatrix} 1 & 0 \\ 0 & 0 \end{bmatrix} \begin{bmatrix} \cos \Theta & -\sin \Theta \\ \sin \Theta & \cos \Theta \end{bmatrix} \begin{bmatrix} \exp(-i\delta) & 0 \\ 0 & \exp(i\delta) \end{bmatrix} \begin{bmatrix} \cos \Theta & \sin \Theta \\ -\sin \Theta & \cos \Theta \end{bmatrix} \\ \times \begin{bmatrix} \exp(i\tilde{n}_\pi \ell) & 0 \\ 0 & \exp(i\tilde{n}_\sigma \ell) \end{bmatrix} \quad (30A)$$

which leads to

$$\mathbf{J} = \begin{bmatrix} [c^2 \exp(-i\delta) + s^2 \exp(i\delta)] \cdot \exp(i\tilde{n}_\pi \ell) & cs[\exp(i\delta) - \exp(-i\delta)] \cdot \exp(i\tilde{n}_\sigma \ell) \\ 0 & 0 \end{bmatrix} \quad (31A)$$

where  $\sin \Theta$  and  $\cos \Theta$  are abbreviated  $s$  and  $c$  respectively.

According to equations (7A) and (8A), the electric vectors of the monochromatic radiation leaving the polariser should be:

$$\mathbf{E}_x = ([c^2 \exp(-i\delta) + s^2 \exp(i\delta)] \exp(i\tilde{n}_\pi \ell) \mathbf{E}_{x,in} + cs[\exp(i\delta) - \exp(-i\delta)] \exp(i\tilde{n}_\sigma \ell) \mathbf{E}_{y,in}) \quad (32A)$$

and

$$E_y = 0 \quad (33A)$$

Using equation (4A), the intensity is found to be:

$$I = \frac{I_0}{4} \{s^2 \cos 2\delta [\exp(-K_\pi N L) - \exp(-K_\sigma N L)] + (2-s^2) \exp(-K_\pi N L) + s^2 \exp(-K_\sigma N L)\} \quad (34A)$$

Substitution of  $\Theta = \pi/4$  rad in equation (34A) leads to

$$I = \frac{I_0}{4} \{\cos 2\delta [\exp(-K_\pi N L) - \exp(-K_\sigma N L)] + \exp(-K_\pi N L) + \exp(-K_\sigma N L)\} \quad (35A)$$

Since  $\delta = \delta^0 \sin \omega_p t$ , the term  $\cos 2\delta$  may be expressed using Bessel functions [55] as

$$\cos 2\delta = J_0(2\delta^0) + 2J_2(2\delta^0) \cos 2\omega_p t + 2J_4(2\delta^0) \cos 4\omega_p t + \dots \quad (36A)$$

In addition, the system uses a  $2\omega_p$  reference; thus only the second harmonic term  $2J_2(2\delta^0)$  contributes to the detected signal. Therefore the final intensity can be interpreted as

$$I = \frac{I_0}{4} \{2J_2(2\delta^0)[\exp(-K_\pi N L) - \exp(-K_\sigma N L)]\} \quad (37A)$$

whose corresponding electric signal will be

$$S(2\omega_p) = \text{constant} \times I_0 [\exp(-K_\pi N L) - \exp(-K_\sigma N L)] \quad (38A)$$

### A.3.3 System No. 3: absorption cell, Faraday configuration.

This optical configuration was used in Chapter 4 (Figure 4.3). The Jones matrix of this system is

$$\mathbf{J} = \mathbf{U}^{-1} \mathbf{F} \mathbf{U} \quad (39)$$

or, in the matrix form,

$$\mathbf{J} = \left( \frac{1-i}{2} \right) \left( \frac{1+i}{2} \right) \begin{bmatrix} 1 & i \\ i & 1 \end{bmatrix} \begin{bmatrix} \exp(i\tilde{n}_+ \ell) & 0 \\ 0 & \exp(i\tilde{n}_- \ell) \end{bmatrix} \begin{bmatrix} 1 & -i \\ -i & 1 \end{bmatrix} \quad (40A)$$

which leads to:

$$\mathbf{J} = \frac{1}{2} \begin{bmatrix} \exp(i\tilde{n}_+ \ell) + \exp(i\tilde{n}_- \ell) & \exp(i\tilde{n}_+ \ell + \pi/2) - \exp(i\tilde{n}_- \ell + \pi/2) \\ \exp(i\tilde{n}_- \ell + \pi/2) - \exp(i\tilde{n}_+ \ell + \pi/2) & \exp(i\tilde{n}_+ \ell) + \exp(i\tilde{n}_- \ell) \end{bmatrix} \quad (41A)$$

Following the procedure outlined above to calculate the intensity,  $I$ , at the detector, it is found that

$$I = I^0 [\exp(iK_+ N \ell) + \exp(iK_- N \ell)] \quad (42A)$$

For this system, the absorption coefficients are in general symmetrical with respect to the central frequency, except for the case when the absorption profile is shifted with respect to the emission profile.

## APPENDIX B. MEASUREMENT OF MAGNETIC FIELDS.

### B.1 Theory.

The experimental determination of magnetic field strength was based on Faraday's Law of induced electromotive forces. This law states that an electromotive force  $\varepsilon$  is induced in a fixed circuit when the magnetic flux  $\phi$  through the circuit is changing;  $\varepsilon$  is proportional to and opposes the time rate of change of the magnetic flux  $\phi$ , i.e.

$$\varepsilon = - d\phi/dt \quad (B1)$$

In a coil (the search coil) with  $N$  turns and surface area  $S$ , where each of the turns experiences the same rate of change, the total induced electromotive force will be equal to the sum of the induced  $\varepsilon$ 's of each turn:

$$\varepsilon_{TOT} = -N d\phi/dt \quad (B2)$$

The magnetic flux  $\phi$  is related to the magnetic flux density  $B$  (which is usually referred to as field strength  $H$ ), by the expression

$$\phi = \int_S \mathbf{B} \cdot d\mathbf{A} \quad (B3)$$

where  $d\mathbf{A}$  is the normal vector to an infinitesimal surface area of the coil. The integration is carried out over the whole surface  $S$ . Assuming that  $\mathbf{B}$  is homogeneous and parallel to each  $d\mathbf{A}$ , for each turn,

$$\phi = BA \quad (\text{B4})$$

where the area is assumed to be constant for each turn.

Substitution of (B4) in (B2) and integration of the resulting expression leads to

$$B = -\frac{1}{NA} \int \epsilon_{\text{TOT}} dt \quad (\text{B5})$$

Measurement of the voltage across a search coil induced by controlled changes in the magnetic field permits calculation of the field strength.

## B.2 Experimental.

Two different approaches were used to measure a.c. and d.c. fields. An a.c. field produces an a.c. induced voltage across the search coil, and the calculation is quite straightforward, as shown in equations (B6)-(B8) below.

$$\epsilon_{\text{TOT}} = \epsilon^{\circ} \sin 2\pi ft \quad (\text{B6})$$

$$B = (\epsilon^{\circ}/2\pi NAf) \cos 2\pi ft \quad (B7)$$

Therefore

$$B_{MAX} = (\epsilon^{\circ}/2\pi NAf) \quad (B8)$$

The parameters involved in the determination of the a.c. fields are shown in Table B.1.

In order to determine the d.c. field, the integral of equation (B5) was evaluated experimentally using an electronic integrator described in Figure B.1. The output of the integrator circuit was:

$$V_o = -\frac{1}{RC} \int_0^{t_1} V_{in} dt \quad (B9)$$

which measures the integral of the induced electromotive force across the search coil produced when the the power supply is switched on and off.

Substitution of (B9) in (B5) leads to

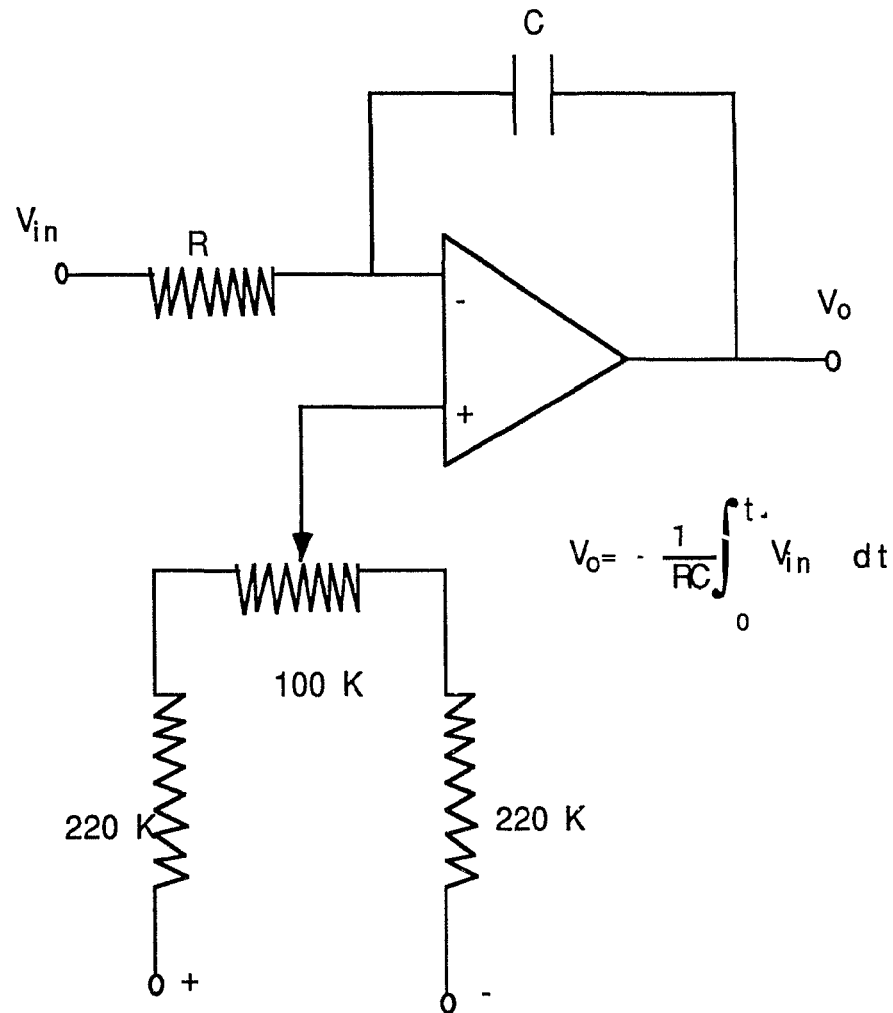
$$B = RCV_o/AN \quad (B10)$$

The parameters involved in the determination of d.c. fields are shown in Table B.1. The field strength versus variac setting of the

different arrangements used throughout this study was converted to a calibration curve (Figure B.2).

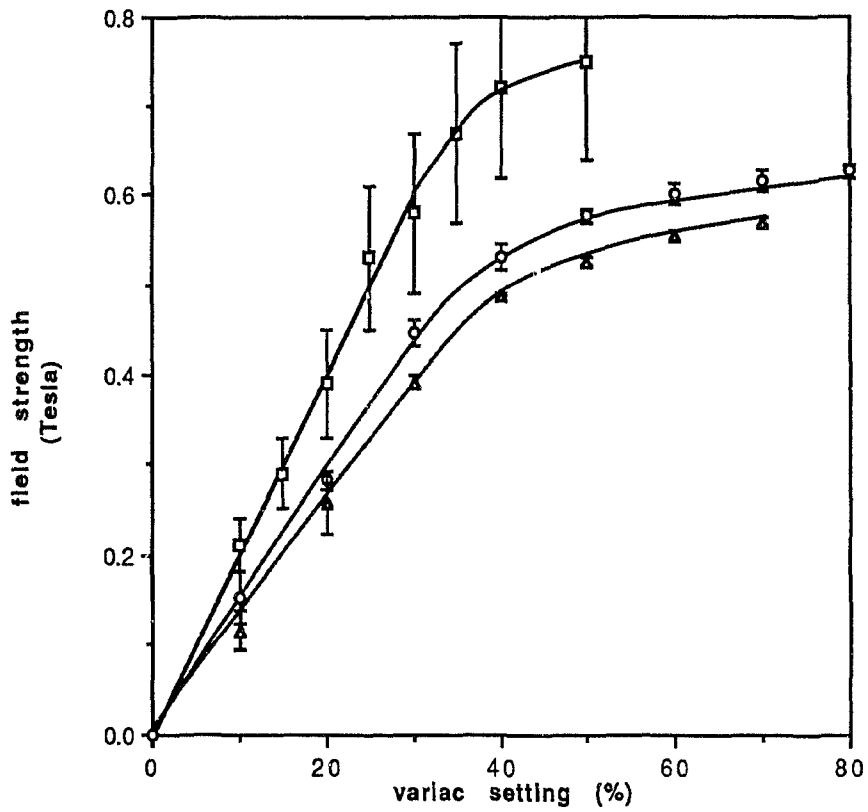
The calculation of the strength of pulsed fields were done using equation (B10). The output of the integrator was measured on an oscilloscope. The parameters involved in the determination of the pulsed fields are shown in Table B.1.

**FIGURE B.1** Electronic device used to measure the strength of d.c. fields.



$V_{in}$  is the voltage across the search coil. The magnetic fields used for the results in section 4.3.1 were determined by using  $C = 1\mu\text{F}$  and  $R = 1\text{K}\Omega$ ; for the results in Chapters 3, 5 and section 4.3.3 the fields were determined by using  $C = 0.185\mu\text{F}$  and  $R = 1\text{M}\Omega$ . The field is calculated as  $B = RC V_o / AN$ , where  $A$  and  $N$  are the area and the number of turns of the search coil.

**FIGURE B.2** Calibration curves for the d.c. magnetic field used in the Voigt configurations.



Chapter 3: separation between the poles 0.86 cm;  $\square$   
Sections 4.3.2. and 4.3.3: separation between the poles 1.5 cm;  $\circ$   
Chapter 5: separation between the poles 1.6 cm;  $\blacktriangle$   
Error bars are the standard deviation of three measurements.

TABLE B.1 Parameters used in field measurements.

Field Strength (Tesla)	Current (A) or voltage (V) across magnet	Search Coil, AN (m-turn)	Reference
0.042 ± 0.003 p (a.c.)	12 A rms	3.15 x 10 <sup>-3</sup>	Chapter 2, Faraday configuration
0.10 ± 0.01 p (a.c.)	330 V rms	4.20 x 10 <sup>-3</sup>	Chapter 3, Voigt configuration
0.25 ± 0.03 (pulse)	Pulse: 22 μsec wide; 12 A	2.73 x 10 <sup>-5</sup>	Sections 4.2.1, 4.31, Faraday configuration.
variable (d.c.; see graph B.2)	variable	1.32 x 10 <sup>-1</sup>	Chapters 3,5; sections 4.2.2, 4.3.2; Voigt configuration.

## APPENDIX C. MODEL FOR THE DICHROIC SIGNAL OF THE 670.8 nm Li DOUBLET VERSUS FIELD STRENGTH.

The 670.8 nm Li doublet corresponds to the  $^2S_{1/2} \text{ --- } ^2P_{1/2}$  and  $^2S_{1/2} \text{ --- } ^2P_{3/2}$  electronic transitions. In the presence of a magnetic field, the Zeeman components start to occupy a common frequency range even at a moderate field strength (less than 1 Tesla); the quantum vectors  $\mathbf{L}$  and  $\mathbf{S}$  of the upper states decouple, showing the Paschen-Back effect.

Experimental measurements of the dichroic signal of the 670.8 nm Li doublet versus field strength (Figures 4.15 and C.5) can be predicted only if the Paschen-Back effect is taken into account. The use of a model based on the Russell-Saunders scheme fails to describe the experimental observations.

Implementation of the model requires: (i) calculation of the frequency shift and intensities of the Zeeman components and (ii) prediction of the total intensity of the  $\sigma$  and  $\pi$  profiles at the detector.

### C.1 Calculation of the frequency shifts and intensities of the Zeeman components.

An outline of the calculations involved is presented below. A comprehensive description is presented by Condon and Shortley [13].

The frequency shift of a Zeeman component can be associated with a perturbation energy. In the Russell-Saunders scheme it is caused by the interaction between the electronic moment and the external field. This interaction is described as

$$\mu_B H (M_J + M_S) | \Psi \rangle = M_J g \mu_B H | \Psi \rangle \quad (C1)$$

The symbol  $| \Psi \rangle$  represents an electronic state (an eigenfunction) which can be described by its quantum numbers;  $\mu_B H (M_J + M_S)$  is a quantum operator;  $M_J g \mu_B H$  is an eigenvalue. The meanings of the other terms was described in section 1.3. As explained earlier, the state  $| \Psi \rangle$  splits into  $2M_J + 1$  components which are shifted by  $M_J g \mu_B H$ . Note that there is no combination of different electronic states.

When **L** and **S** decouples, the perturbation energy must include the spin-orbit interaction, in addition to the interaction with the external field. The operator of this interaction is **L**•**S** and it operates on the quantum vectors of the individual electrons; thus the quantum numbers  $s, l, m_s, m_l$  are good numbers [54]. If a state is represented by its quantum numbers as  $| s, l, m_s, m_l \rangle$ , the perturbation energy of the LS interaction can connect it with another state  $| s, l, m'_s, m'_l \rangle$ , that is

$$\langle s, \ell, m'_s, m'_\ell | \mathbf{L} \cdot \mathbf{S} | s, \ell, m_s, m_\ell \rangle \quad (\text{C2})$$

where  $m'_s = m_s$  or  $m_s \pm 1$  and  $m'_\ell + m'_s = m_s + m_\ell$ .

In order to obtain the eigenvectors of the expression (C2) the eigenfunctions are a linear combination of several electronic states as specified by their quantum numbers:

$$|\Psi\rangle = \sum_{m_s} \sum_{m_\ell} a_i |m_s, m_\ell\rangle \quad (\text{C3})$$

For instance, in the case of the upper states of the Li doublet  $2P_{3/2}$  and  $2P_{1/2}$ ,  $a_1$  corresponds to the state  $|m_s=1/2, m_\ell=1\rangle$ ;  $a_2$  to  $|m_s=-1/2, m_\ell=1\rangle$ ;  $a_3$  to  $|m_s=1/2, m_\ell=0\rangle$ ;  $a_4$  to  $|m_s=-1/2, m_\ell=0\rangle$ ;  $a_5$  to  $|m_s=1/2, m_\ell=-1\rangle$ ; and  $a_6$  to  $|m_s=-1/2, m_\ell=-1\rangle$ .

The perturbation energies associated with the different components of the multiplet are obtained by using the operator that describes the effect of the magnetic field and the LS splitting [13]. That is,

$$\langle \Psi' | \mathbf{L} \cdot \mathbf{S} + \mu_B \mathbf{H} (m_\ell + 2m_s) | \Psi \rangle \quad (\text{C4})$$

where  $|\psi\rangle$  is described in equation (C3). Each of the eigenvalues represents the energy shift from the zero field. The ground state  $2S_{1/2} \text{ sp}'$  to two levels, since  $l=0$ .

Based on the selection rules, the proper combination of the upper state with the lower state is used to calculate the frequency shift of each of the components of the Zeeman multiplet [54]. The frequency displacement is calculated as shown in the computer program below.

The relative intensity of each component is calculated as

$$|\langle \text{upper state} | \mathbf{P} | \text{lower state} \rangle|^2 \quad (\text{C5})$$

where  $\mathbf{P}$  is the dipole moment operator. A general solution to equation (C5) is given by Condon and Shortley [13]. These results are used to find the relative intensity of each Zeeman component in the program described below.

## C.2 Total intensity of the $\sigma$ and $\pi$ components.

The following calculations refer to a transverse magnetic field applied to the atomiser and a lithium doublet as the source.

The total intensity of the source  $I(\nu)$  is calculated as the sum of the two components of the doublet

$$I(v) = I_1(v) + I_2(v) \quad (C6)$$

$I_1(v)$  and  $I_2(v)$  are described by Gaussian functions as:

$$I_1(v) = \frac{2 I_0}{3} \exp \left[ -2 \sqrt{\ln 2} \frac{v - v_{s1}}{\Delta v_s} \right]^2 \quad (C7)$$

and

$$I_2(v) = \frac{I_0}{3} \exp \left[ -2 \sqrt{\ln 2} \frac{v - v_{s2}}{\Delta v_s} \right]^2 \quad (C8)$$

where  $v_{s1}$  and  $v_{s2}$ , the centre frequencies of each line, are displaced from the origin of the doublet  $v_0$ . They are:

$$v_{s1} = v_0 + \frac{\Delta LS}{3} \quad (C9)$$

and

$$v_{s2} = v_0 - \frac{2 \Delta LS}{3} \quad (C10)$$

where  $\Delta LS$  is the separation between the two lines. The remaining terms has the same meaning as elsewhere (sections 1.1, 2.1, and 3.1).

The total absorption coefficients  $K_{\pi}(\nu)$  and  $K_{\sigma}(\nu)$  are found by adding the contribution of each component of the multiplet:

$$K_{\pi}(\nu) = \sum_{i=1}^n K_{\pi;i}(\nu) \quad (\text{C11})$$

and

$$K_{\sigma}(\nu) = \sum_{j=1}^{n'} K_{\sigma;j}(\nu) \quad (\text{C12})$$

where each component is described as

$$K_{\pi;i}(\nu) = K_{0;i} \exp \left[ -2 \sqrt{\ln 2} \frac{\nu - \nu_{a;i}}{\Delta \nu_a} \right]^2 \quad (\text{C13})$$

and

$$K_{\sigma;j}(\nu) = K_{0;j} \exp \left[ -2 \sqrt{\ln 2} \frac{\nu - \nu_{a;j}}{\Delta \nu_a} \right]^2 \quad (\text{C14})$$

The coefficients  $K_{0;i}$  and  $K_{0;j}$  are the relative intensities obtained from (C5);  $\nu_{a;i}$  and  $\nu_{a;j}$  are the separation between the maximum frequency of each component, (including the collisional shift of the absorption profile), and the origin of the source  $\nu_s$ ; the rest other terms have the same meaning as elsewhere (sections 1.1, 2.1, and 3.1).

The intensities at the detector are then expressed as

$$I_{\pi} = \int_w I(\nu) \exp(-K_{\pi}(\nu)Nl) d\nu \quad (\text{C15})$$

and

$$I_{\sigma} = \int_w I(\nu) \exp(-K_{\sigma}(\nu)Nl) d\nu \quad (\text{C16})$$

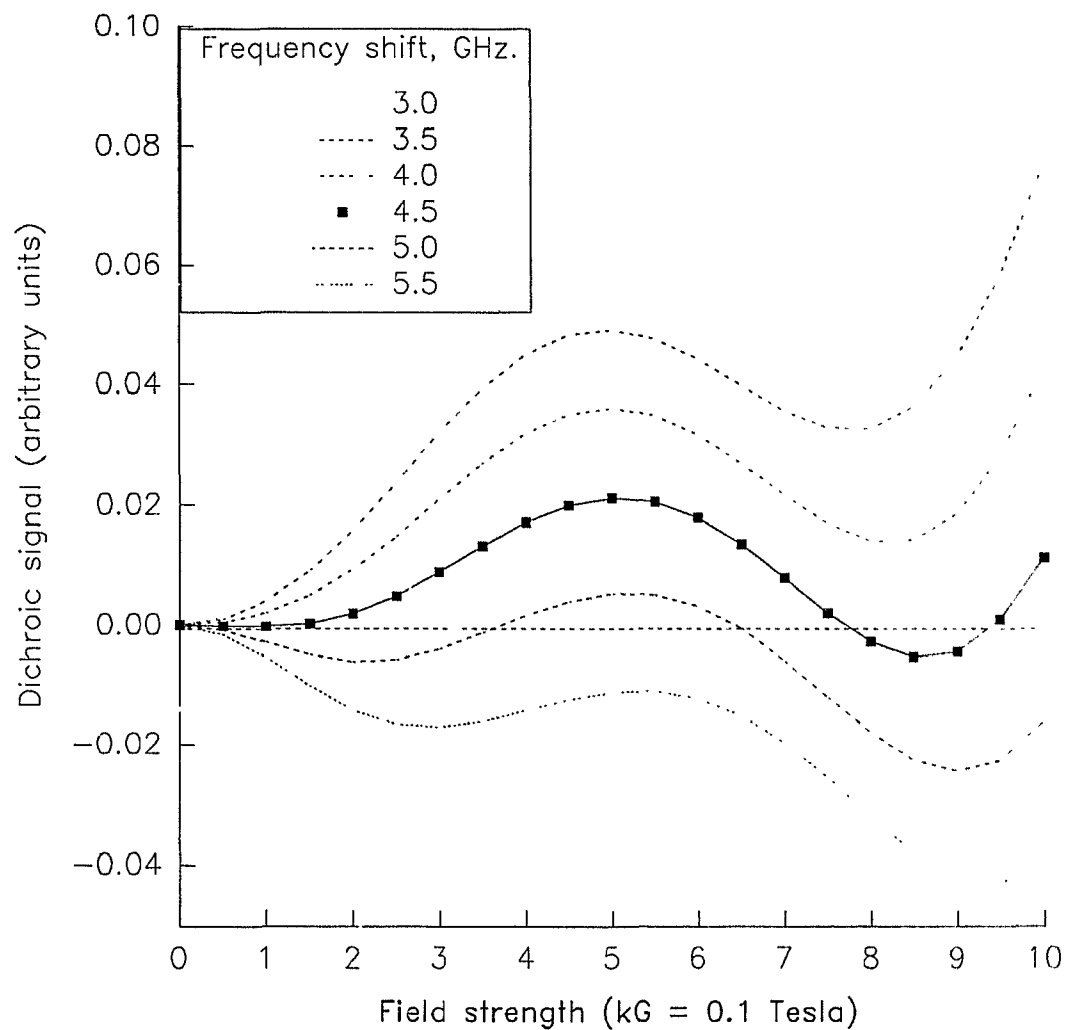
### C.3 Computer program.

The calculations outlined above are included in the program PB-ATS2.BAS (Table C.1). The dichroic signal is calculated as  $I_{\sigma} - I_{\pi}$ , which was the response of the instrument described in Chapter 3.

The selection of the parameters to simulate the results was made by investigating the influence of each of them on the dichroic response (Figure C.1- C.4).

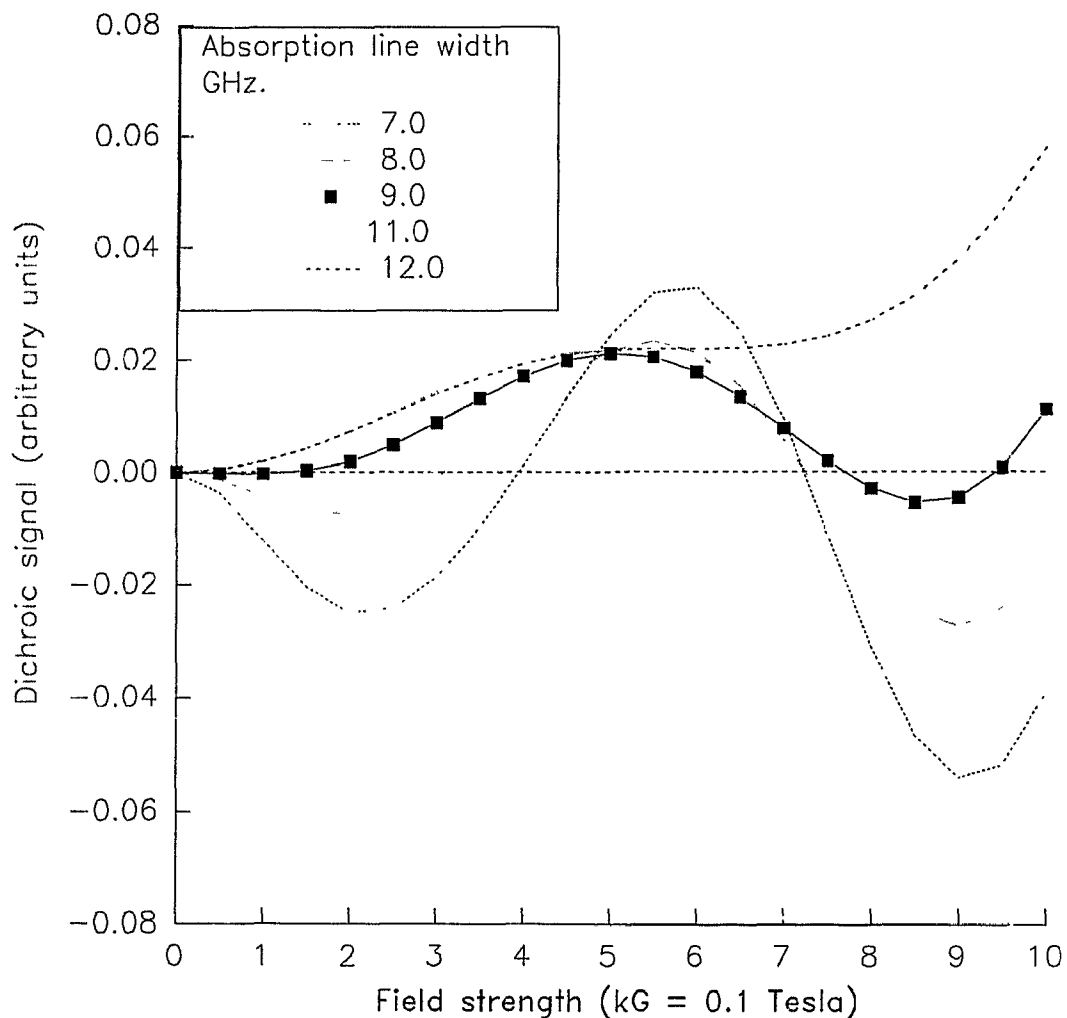
A comparison of the experimental results with this model (Figure C.5) shows that the model is able to predict the presence of the maximum observed experimentally. Use of the standard weak field (Russell-Saunders approximation), also shown in Figure C.5, resulted in serious departures from experimental observation. This is believed to be the first time that errors in the response of a Zeeman-corrected atomic absorption instrument caused by the Paschen-Back effect have been observed.

FIGURE C.1 Dependence of the dichroic signal on the frequency shift. Simulated data.



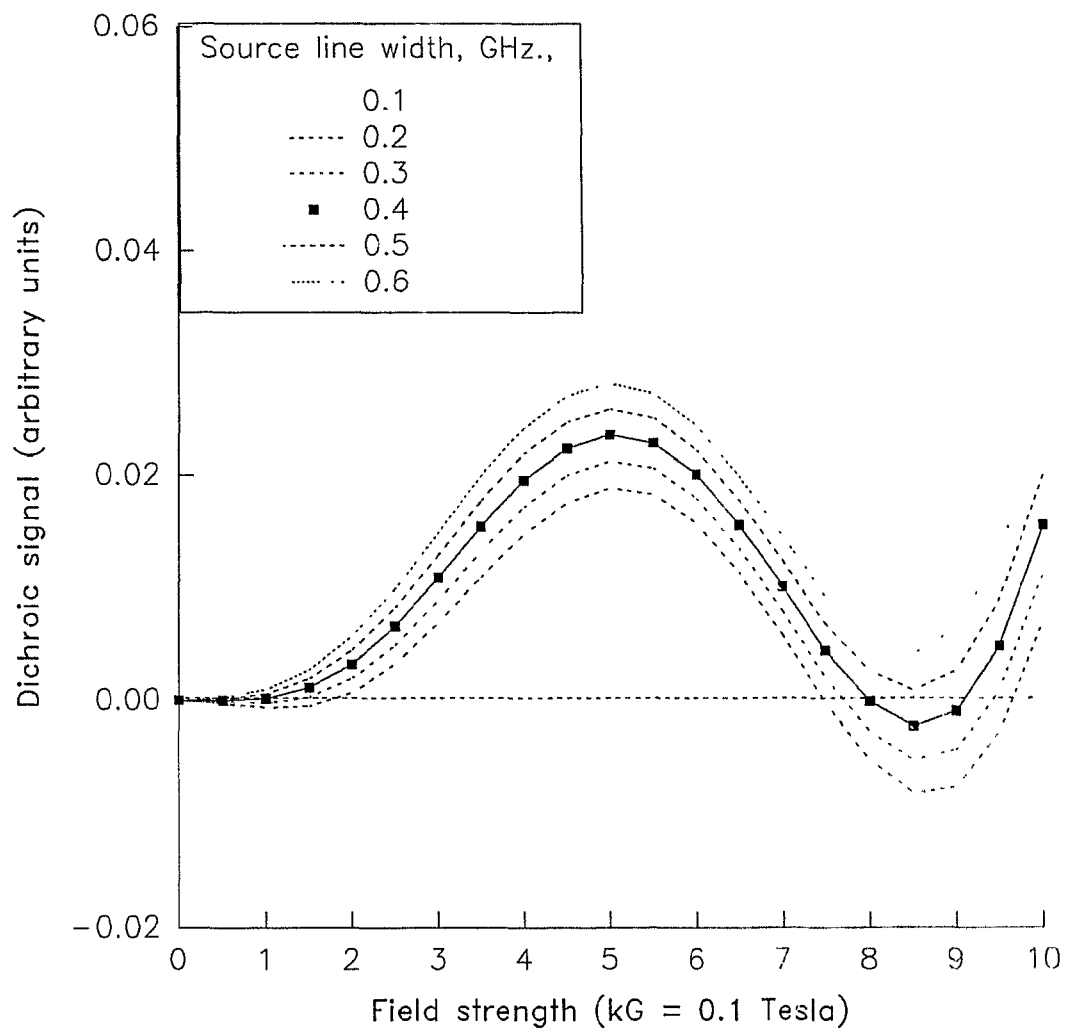
Source: 670.8 nm Li doublet. Absorption coefficient = 0.1; source line width = 0.4 GHz.; absorption line width = 9.0 GHz; Selected frequency shift to match experimental data = 4.5 GHz; Program PB-ATS2.BAS; Paschen-Back model.

FIGURE C.2 Dependence of the dichroic signal on the width of the absorption profile. Simulated data.



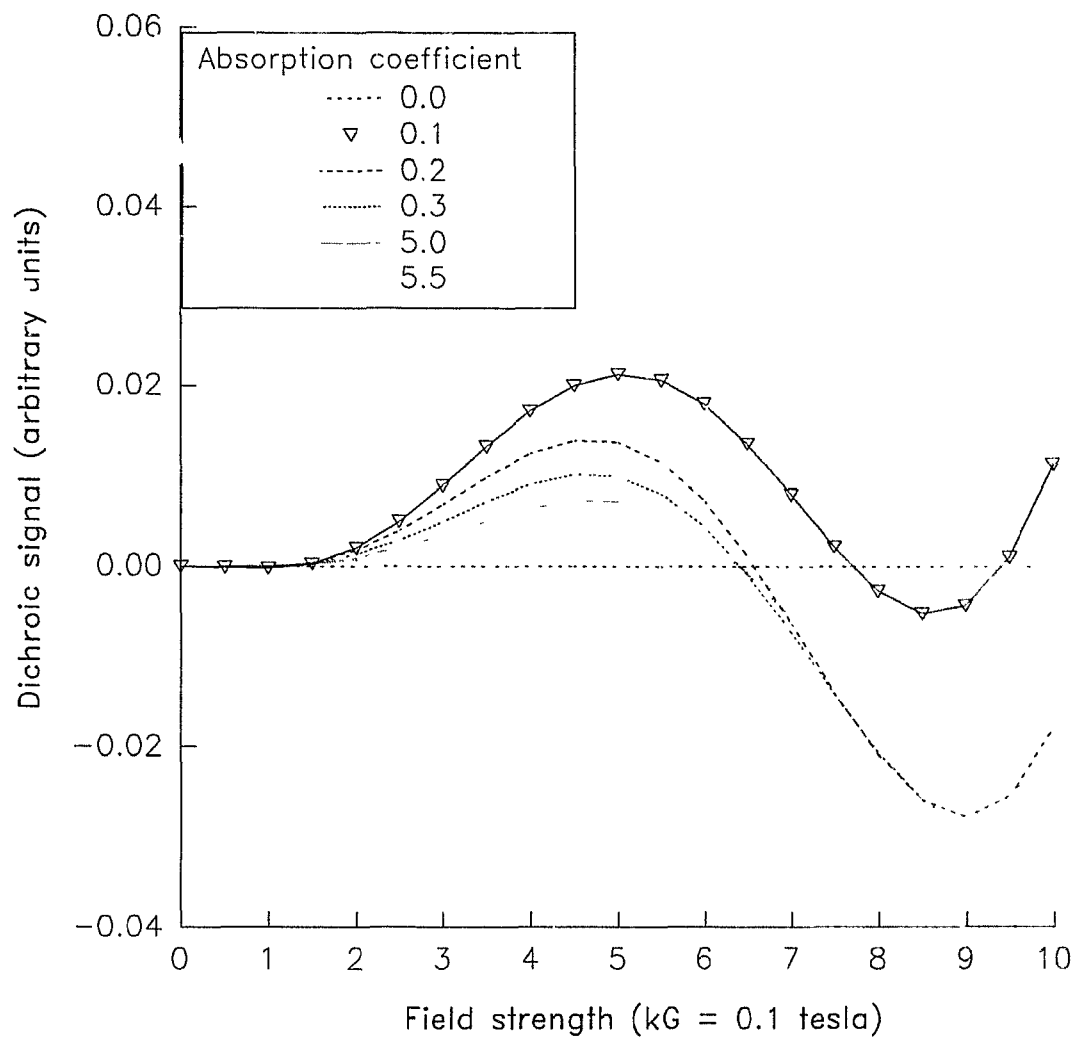
Source: 670.8 nm Li doublet; Absorption coefficient = 0.1; source line width = 0.4 GHz; frequency shift = 4.5 GHz. Program PB-ATS2.BAS; Paschen-Back model. Selected width of the absorption profile to match the experimental data 9.0 GHz.

FIGURE C.3 Dependence of the dichroic signal on the width of the source profile. Simulated data.



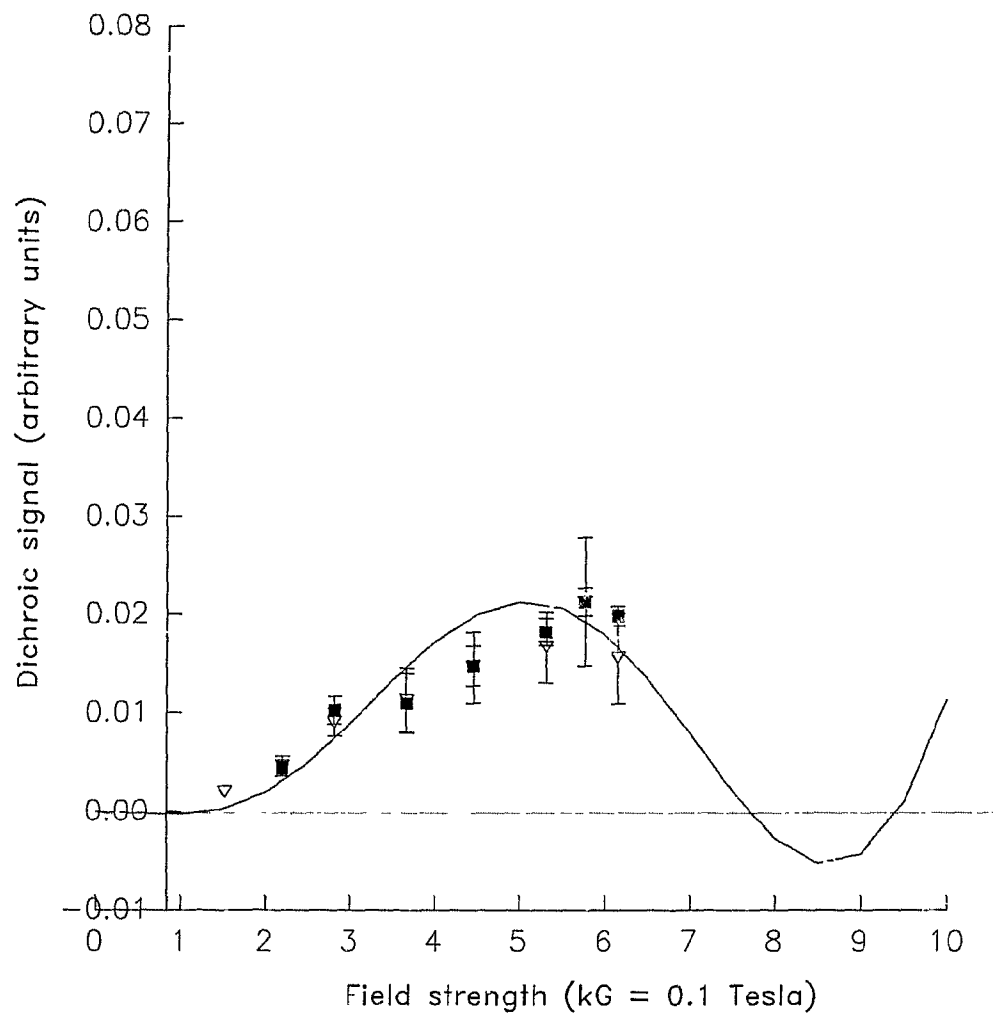
Source: 670.8 nm Li doublet; Absorption coefficient = 0.1; frequency shift = 4.5 GHz; absorption line width = 4.5 GHz. Program PB-ATS2.BAS; Paschen-Back model. Selected width of the source profile to match the experimental data 0.4 GHz.

FIGURE C.4 Dependence of the dichroic signal on the absorption coefficient. Simulated data.



Source: 670.8 nm Li doublet; Absorption line width = 9.0 GHz; source line width = 0.4 GHz; frequency shift = 4.5GHz. Program PB-ATS2.BAS; Faschen-Back model. Selected absorption coefficient to match the experimental data 0.1

FIGURE C.5 Simulated and experimental data of dichroism versus field strength at the 670.8 nm Li doublet.



Experimental data: Hollow-cathode lamp at 48 mA ( $\nabla$ ) and 84 mA ( $\blacksquare$ ); other conditions are the same as in Figure 4.15. Simulated data: Program PB-ATS2.BAS; Paschen-Back model (—) and Russell-Saunders model (—); absorption coefficient = 0.1; source line width = 0.4 GHz; absorption line width = 9.0 GHz; frequency shift = 4.5 GHz.

TABLE C.1 Program PB-ATS BAS

```

DECLARE SUB INTENSITY (DVS#, DV#, VLX#, DE#, KO#, F#(), J#(),
U$( ), PSUM#, SSUM#)
CLS
REM SOURCE: 670.8 NM Li DOUBLET.
REM DICHROIC SIGNAL VERSUS FIELD APPLIED AROUND THE ATOMISER.
REM WEAK FIELD (RS COUPLING) USES THE VARIABLES F(),J(),U$( ).
REM STRONG FIELD (PB EFFECT) USES THE VARIABLES E(),I(),T$( ).
REM SUBPROGRAM INTENSITY USES SIMPSON'S RULE (100 POINTS) TO
INTEGRATE THE -
REM SIGNAL OVER THE SOURCE PROFILE.
REM REFERENCE: Stephens, R.,PROGRESS IN ANALYTICAL
SPECTROSCOPY,12,277,1989.
DEFDBL A-Z
DEFINT N
NS = 100
DIM X(NS\), ITP(NS), ITS(NS), IT0(NS), SINT(20, 20), PINT(20,
20), DELINT(20, 20), REX(20), REX2(20), H(20)
PRINT "PB-ATS2 considers a field-on-atomiser configuration and
a doublet source"
PRINT "to calculate the difference of the intensity of the
polarised components"
PRINT "versus field strength."
PRINT " "
INPUT "Russell-Saunders coupling: RS;or Paschen-Back effect:
PB?"; PB$
INPUT "FILE NAME"; G$
INPUT " IDENTIFICATION NUMBER "; NAB
F$ = "B:" + PB$ + G$ + MID$(STR$(NAB), 2, 3)
INPUT "L-S SPLIT, GHz"; DE
E = DE * 2 / 3
IF E = 0 THEN E = 1E-09
REM INPUT " ABSORBANCE, KoNL"; KO
INPUT "FWHM of abs.line,GHz"; DVX
INPUT "FWHM OF SOURCE LINE, Ghz"; DVSX
INPUT "freq.shift of abs.line, GHz"; VLX
DV = 2 * SQR(LOG(2)) / DVX
DVS = 2 * SQR(LOG(2)) / DVSX
REM FOLLOWING LOOP VARIES ONE OF THE PARAMETERS ABOVE;MAKE
ADJUSTMENTS.
FOR NAB = 0 TO 5
  KO = NAB / 10
  PRINT "ABSORPTION COEFFICIENT "; KO
  MAX(NAB) = 0
  FOR NQ = 0 TO 20
    H = NQ / 2
  REM PB EFFECT CALCULATIONS BEGIN.
    E1 = 2.8 * H + E / 2
    T = SQR(2.25 * E ^ 2 + (1.4 * H) ^ 2 + 1.4 * H * E)
    E2 = .7 * H - E / 4 + T / 2

```

```

E3 = E2 - T
T = SQR(2.25 * E ^ 2 + (1.4 * H) ^ 2 - 1.4 * H * E)
E4 = -.7 * H - E / 4 + T / 2
E5 = E4 - T
E6 = -2.8 * H + E / 2
A1 = 1: A6 = 1
A2 = E ^ 2 / 2 / (E2 ^ 2 + E2 * E + .75 * E ^ 2)
A3 = 1 - A2
B2 = (E3 ^ 2 - 2.8 * H * E3 + (1.4 * H) ^ 2) / (E3
^ 2 - 2.8 * H * E3 + (1.4 * H) ^ 2 + E ^ 2 / 2)
B3 = 1 - B2
A4 = E ^ 2 / 2 / (E4 ^ 2 + 2.8 * H * E4 + (1.4 * H)
^ 2 + E ^ 2 / 2)
A5 = 1 - A4
B4 = (E5 ^ 2 + E5 * E + E ^ 2 / 4) / (E5 ^ 2 + E5 *
E + .75 * E ^ 2)
B5 = 1 - B4
E(1) = E1 - 1.4 * H: T$(1) = "S": I(1) = A1 / 2
E(2) = E2 - 1.4 * H: T$(2) = "P": I(2) = A3
E(3) = E2 + 1.4 * H: T$(3) = "S": I(3) = A2 / 2
E(4) = E3 - 1.4 * H: T$(4) = "P": I(4) = B3
E(5) = E3 + 1.4 * H: T$(5) = "S": I(5) = B2 / 2
E(6) = E4 - 1.4 * H: T$(6) = "S": I(6) = A5 / 2
E(7) = E4 + 1.4 * H: T$(7) = "P": I(7) = A4
E(8) = E5 - 1.4 * H: T$(8) = "S": I(8) = B5 / 2
E(9) = E5 + 1.4 * H: T$(9) = "P": I(9) = B4
E(0) = E6 + 1.4 * H: T$(0) = "S": I(0) = A6 / 2
REM INTENSITY OF EACH COMPONENT IS NORMALISED
II = 0
FOR N = 0 TO 9
  N(N) = N
  II = II + I(N)
NEXT N
FOR N = 0 TO 9
  I(N) = I(N) / II
NEXT N
REM COMPONENTS ARE ORDERED BY INCREASING FREQUENCY SHIFT.
FOR N1 = 0 TO 8
  N = N1
  470         IF E(N + 1) >= E(N) THEN 490
  T = E(N): E(N) = E(N + 1): E(N + 1) = T
  T = I(N): I(N) = I(N + 1): I(N + 1) = T
  T = N(N): N(N) = N(N + 1): N(N + 1) = T
  T$ = T$(N): T$(N) = T$(N + 1): T$(N + 1) = T$
  N = N - 1
  490         IF N >= 0 THEN 470
NEXT N1

REM END PB CALCN;energy shifts,intensities,polarisation states
in E(),I(),T$()
REM RS CALCULATIONS BEGIN.
J(1) = 1 / 8: J(2) = 1 / 6: J(3) = 1 / 24: J(4) =

```

```

J(3): J(5) = J(2): J(6) = J(1)
      F(1) = DE / 3 + 1.4 * H: F(2) = DE / 3 - 1.4 * H /
3: F(3) = DE / 3 + 5 * 1.4 * H / 3
      F(4) = DE / 3 - 5 * 1.4 * H / 3: F(5) = DE / 3 + 1.4
* H / 3: F(6) = DE / 3 - 1.4 * H
      U$(1) = "S": U$(2) = "P": U$(3) = "S": U$(4) = "S":
U$(5) = U$(2): U$(6) = "S"
      J(7) = 1 / 12: J(8) = 1 / 12: J(9) = J(8): J(0) =
J(7)
      F(7) = -2 / 3 * (DE + 1.4 * H): F(8) = -2 / 3 * DE
+ 4 * 1.4 / 3 * H: F(9) = -2 / 3 * (DE + 2 * 1.4 * H): F(0) =
-2 / 3 * DE + 1 / 3 * 1.4 * H
      U$(7) = "P": U$(8) = "S": U$(9) = "S": U$(0) = U$(7)
REM INTENSITY OF EACH COMPONENT IS NORMALISED.
      II = 0
      FOR N = 0 TO 9
        N(N) = N
        II = II + J(N)
      NEXT N
      FOR N = 0 TO 9
        J(N) = J(N) / II
      NEXT N
      REM COMPONENTS ARE ORDERED BY INCREASING FREQUENCY SHIFT.
      FOR N1 = 0 TO 8
        N = N1
510          IF F(N + 1) >= F(N) THEN 530
              T = F(N): F(N) = F(N + 1): F(N + 1) = T
              T = J(N): J(N) = J(N + 1): J(N + 1) = T
              T = N(N): N(N) = N(N + 1): N(N + 1) = T
              T$ = U$(N): U$(N) = U$(N + 1): U$(N + 1) = T$
              N = N - 1
              IF N >= 0 THEN 510
530          NEXT N1
      REM END RS CALCN;energy shifts,intensities,polarisation states
      in J(N),F(N),U$( )
      REM CALC.INTENSITY OVER THE SOURCE PROFILE WIDTH.
      IF PB$ = "RS" THEN CALL INTENSITY(DVS, DV, VLX, DE,
      KO, F(), J(), U$(), PSUM, SSUM)
      IF PB$ = "PB" THEN CALL INTENSITY(DVS, DV, VLX, DE,
      KO, E(), I(), T$(), PSUM, SSUM)
      SINT(NAB, NQ) = SSUM: PINT(NAB, NQ) = PSUM:
      DELINT(NAB, NQ) = SSUM - PSUM
      PRINT "H="; H; " Sint.="; SSUM; " Pint.="; PSUM;
      "Del ="; SSUM - PSUM
      REM SELECTION OF MAXIMUM POINT.
      IF NQ = 0 THEN 550
      IF MAX(NAB) < DELINT(NAB, NQ) AND DELINT(NAB, NQ -
      1) > DELINT(NAB, NQ) THEN MAX(NAB) = DELINT(NAB, NQ - 1)
      PRINT "MAXIMUM"; MAX(NAB)
550          NEXT NQ
      NEXT NAB
      REM NORMALISATION OF EXPERIMENTAL DATA.

```



```

      ITP(N) = 2 * ITP(N) + .5 * EXP(-TT ^ 2) *
EXP(-KO * P) / 3
      ITO(N) = 2 * ITO(N) + EXP(-TT ^ 2) / 3
      NEXT N
      NEXT ND
      IX = ITS(NS) - ITS(0): IP = ITP(NS) - ITP(0): IO =
ITO(NS) - ITO(0)
      FOR N = 0 TO 100 / 2 - 1
      IX = IX + 4 * ITS(2 * N + 1) + 2 * ITS(2 * N):
IP = IP + 4 * ITP(2 * N + 1) + 2 * ITP(2 * N)
      IO = IO + 4 * ITO(2 * N + 1) + 2 * ITO(2 * N)
      NEXT N
      IX = IX * (UL - LL): IP = IP * (UL - LL): IO = IO *
(UL - LL)
      PSUM = IP / IO: SSUM = IX / IO

END SUB

```

## BIBLIOGRAPHY.

- [1] Mitchell, A. and M. Zemansky, **Resonance radiation and excited atoms**, Cambridge University Press, N.Y., U.S.A., (1971).
- [2] Hieftje, G. M., **Journal of Analytical Atomic Spectrometry**, 4, 117-122, (1989).
- [3] Sharp, B., et al., **Journal of Analytical Atomic Spectrometry**, 2, 167R, (1987).
- [4] Kirkbright, G. F. and M. Sargent, **Atomic Absorption and Fluorescence Spectroscopy**, Academic Press, London, (1974).
- [5] Schrenk, W. G., **Applied Spectroscopy**, 40, xix-xxviii, (1986).
- [6] Marshall, J., et al., **Analytica Chimica Acta**, 180, 357-371, (1986).
- [7] Walsh, A., **Spectrochimica Acta**, 7, 108-117, (1955)
- [8] Alkemade, C. T. J. and J. M. W. Milatz, **Journal of the Optical Society of America**, 45, 583, (1955)
- [9] Marshall, J., Haswell, S. J., and S. Hill, **Journal of Analytical Atomic Spectrometry**, 4, 111R-136R, (1989).
- [10] Wagenaar, H. C. and L. de Galan, **Spectrochimica Acta**, 28B, 157-177, (1973).
- [11] Wagenaar, H. C. and L. de Galan, **Spectrochimica Acta**, 30B, 361-381, (1975).
- [12] Candler, C., **Atomic Spectra and the Vector Model**, Second Edition, Hilger & Watts Ltd., London, (1964).

- [13] Condon, E. U. and G. H. Shortley, **The Theory of Atomic Spectra**, Cambridge University Press, Cambridge, (1963)
- [14] de Loos-Vollebregt, M. T. C. and L. de Galan, **Progress in Analytical Atomic Spectroscopy**, 8, 47-81, (1985).
- [15] Norris, J. D. and T. S. West, **Analytical Chemistry**, 46, 1423-1426, (1974).
- [16] Smith, Jr., S. B. and G. M. Hieftje, **Applied Spectroscopy**, 37, 419-424, (1983).
- [17] de Loos-Vollebregt, M. T. C. and L. de Galan, **Spectrochimica Acta**, 33B, 495-511, (1978).
- [18] Massman, H., **Talanta**, 29, 1051-1055, (1982).
- [19] Carrick, G. R., Barnett, W., and W. Slavin, **Spectrochimica Acta**, 41B, 991-997, (1986).
- [20] Wennich, R., Frech, W., and E. Lundberg, **Spectrochimica Acta**, 44B, 239-246, (1989).
- [21] Wibetoe, G. and F. J. Langmyhr, **Analytica Chimica Acta**, 165, 87, (1984).
- [22] Wibetoe, G. and F. J. Langmyhr, **Analytica Chimica Acta**, 176, 33, (1985).
- [23] Wibetoe, G. and F. J. Langmyhr, **Analytica Chimica Acta**, 186, 55, (1986).
- [24] Wibetoe, G. and F. J. Langmyhr, **Analytica Chimica Acta**, 198, 81, (1987).
- [25] Murphy, G. F. and R. Stephens, **Talanta**, 25, 441-445, (1978).

- [26] Wheat, J. A., **Applied Spectroscopy**, 25, 328-330, (1975).
- [27] Chapman, J. F. and L. S. Dale, **Analytica Chimica Acta**, 87, 91-95, (1976).
- [28] Chapman, J. F., Dale L. S., and H. J. Fraser, **Analytica Chimica Acta**, 116, 427-431, (1980).
- [29] Kushita, K., **Analytica Chimica Acta**, 183, 225-230, (1986).
- [30] Sullivan, J. V. and A. Walsh, **Spectrochimica Acta**, 22, 1843-52, (1966).
- [31] Matsuta, H. and K. Hirokawa, **Spectrochimica Acta**, 43B, 159-65, (1988).
- [32] Stephens, R., **Journal of Analytical Atomic Spectrometry**, 3, 1137, (1988).
- [33] Ciszewski, A., et al., **Analytical Chemistry**, 61, 856-860, (1989).
- [34] Sioda, R., et al., **Talanta**, 33, 421-428, (1986).
- [35] Batley, G. E., **Analytica Chimica Acta**, 124, 121-129, (1981).
- [36] Batley, G. E. and J. P. Matovsek, **Analytical Chemistry**, 52, 1570-1574, (1980).
- [37] Frick, D. A. and D. E. Tallman, **Analytical Chemistry**, 54, 1217-1219, (1982).
- [38] Batley, G. E. and J. P. Matovsek, **Analytical Chemistry**, 49, 2031, (1977).

- [39] Czobik, E. J. and J. P. Matovsek, **Spectrochimica Acta**, 35B, 741-751, (1980).
- [40] Newton, M.P. and D.G. Davis, **Analytical Chemistry**, 47, 2003, (1975).
- [41] Fairless, C. and A. J. Bard, **Analytical Letters**, 5, 433-438, (1972).
- [42] Holen, B., Ragnar, B., and W. Lund, **Analytical Chimica Acta**, 130, 257-265, (1981).
- [43] Sioda, R.E., **Analytical Chemistry**, 60, 1177-1179, (1988).
- [44] Stephens, R., **Talanta**, 26, 57-59, (1979).
- [45] Tie-Zheng, G. and R. Stephens, **Journal of Analytical Atomic Spectrometry**, 1, 355-357, (1986).
- [46] Bashkin, S. and J.O. Stoner, **Atomic Energy Levels and Grotrian Diagrams**, Vol I, North-Holland Publishing Co., Amsterdam, (1975).
- [47] Arriaga, E. and R. Stephens, **Spectrochimica Acta**, 44B, 867-876, (1989).
- [48] Pearse, R.W. and A.G. Gaydon, **The identification of molecular spectra**, London, Chapman & Hall Ltd., (1941).
- [49] Jones, R. C., **Journal of the Optical Society of America**, 31, 488-503, (1941).
- [50] Kankare, J. K. and R. Stephens, **Spectrochimica Acta**, 35B, 849-864, (1980).

- [51] Jones, R. C., **Journal of the Optical Society of America**, **32**, 486-493, (1942).
- [52] Jones, R. C., **Journal of the Optical Society of America**, **37**, 110-112, (1947).
- [53] Gerrard, A. and J. M. Burch, **Introduction to Matrix Methods in Optics**, John Wiley & Sons, London, (1975).
- [54] Stephens, R., **Progress in Analytical Atomic Spectroscopy**, **12**, 277-347, (1989).
- [55] Spiegel, A., **Manual de formulas y tablas matematicas**, McGraw-Hill de Mexico S.A. de C.V., Mexico, (1970).